Università degli Studi di Salerno
Dipartimento di Fisica "E. R. Caianiello"
via Giovanni Paolo II, 132 - 84084 Fisciano (SA)

Dottorato di Ricerca in Matematica, fisica e applicazioni, XXXII ciclo

Tesi di Dottorato in Fisica

New features exhibited by transition metal pnictides

Candidate:
Giuseppe Cuono

Supervisor:
Prof. Canio Noce
Dr. Carmine Autieri

Ph.D. Coordinator:
Prof. Carmine Attanasio

Academic Year: 2018/19

A thesis submitted in fulfillment of the requirements for the degree of Doctor of Philosophy

A mia madre e mio padre

Contents

Chapter 1

Introduction

Since the time of the discovery of the superconductivity in heavy-fermion compounds [1], high transition temperature cuprates [2], strontium ruthenates [3] and iron pnictides [4], great attention has been given to the search for similar phenomena in other transition metal oxides or pnictides [5, 6]. In 2010, Wu et al. [7] studied some electron and magnetic features of CrAs, one of the intermetallic pnictides with crystal structure of orthorhombic MnP-type at ambient pressure and belonging to the Pnma space group, finding that above 270 K, a linear-temperature dependence of the magnetic susceptibility is observed up to 700 K, which resembles the T-dependent magnetic susceptibility of parents of iron-pnictides superconductors. In 2014, two groups, those of Wu et al. [8] and Kotegawa et al. [9], reported the discovery of superconductivity on the verge of antiferromagnetic order in CrAs via the application of external pressure. The bulk superconductivity with $T_C \sim 2$ K emerges at the critical pressure $P_C \sim 8$ kbar, where the first-order magnetic transition at $T_N \sim 275$ K is completely suppressed [8]. A common feature of CrAs and the other superconductors previously mentioned is that superconductivity emerges in the vicinity of a quantum critical point where a high-temperature ordered state involving spin, charge or lattice degrees of freedom is suppressed by applying external tuning parameter, such as doping charge carrier, chemical or physical pressure [10]. The vicinity of the superconductivity to a magnetic phase suggested a possible unconventional pairing mechanism where the critical spin fluctuations could act as the glue medium for Cooper pairing [8]. CrAs was the first example of superconductivity found in a Cr-based magnetic system [8].

The discovery of superconductivity in CrAs suggested a routine for exploring new superconductors, starting with a magnetic order and suppressing it by applying chemical or physical pressure [6]. A member of the same family of CrAs, namely belonging to the Pnma space group, and that exhibits a similar phase diagram, with the superconductivity appearing close to a magnetic phase and under the application of external pressure, is the MnP [11]. The MnP was identified as the first Mn-based superconductor and has the critical superconducting temperature $T_c \sim 1$ K at a pressure $P_C \sim 8$ GPa [11]. Very recently, Liu et al. [12] found an other superconductor of the same class of CrAs and MnP, namely the WP, with a bulk superconductivity appearing at 0.84 K, at ambient pressure.

In 2015 the superconductivity was discovered in new Cr-based materials, the $A_2Cr_3As_3$ compounds, with A being Na [13], K [14], Rb [15] or Cs [16]. Differently from the CrAs, these are superconductors at ambient pressure and at the temperatures of 8.6 K [13], 6.1 K [14], 4.8 K [15] and 2.2 K [16], respectively. They present a quasi-one dimensional (Q1D) and hexagonal crystal structure at room temperature that consists of double walled $[(Cr_3As_3)^{2-}]_\infty$ nanotubes separated by columns of A^+ ions, with chromium atoms forming the inner wall and arsenic atoms the outer one [13, 14, 15, 16]. These materials are very peculiar because of the fact that are Q1D and at the same time superconductors; the superconductivity is not so frequent in Q1D compounds due to the Peierls instability [17, 18]. The investigation of the superconductivity in Q1D materials can lead to greater understanding of the unconventional superconducting mechanism because of the inherent simplicity of one dimensionality. Since $3d$-transition elements generally bear strong electron correlations, additional interest is given by the possible realization of a Luttinger liquid in Q1D compounds with interacting electrons [19].

All these compounds belonging to the large family of the trasition metal pnictides are at the centre of today's debat because they are rich in novel and intriguing behaviours due to multiple quantum orders and competing phenomena. They still need a deep analysis to better understand the interplay between structural, electronic, magnetic and superconducting properties and their connections to the topological features. It is important, in support of experimental data, to analyze the electronic structure from a theoretical point of view, as well as the magnetism and the symmetries related to the crystal structure. In this thesis we will focus on the transition metal compounds belonging to the space group Pnma, namely CrAs, MnP and WP, and on the quasi-one-dimensional class of materials $A_2Cr_3As_3$, in particular we will study the compound with A=K. We present the analysis of their structural, electronic, magnetic, transport and symmetry properties by using model Hamiltonian approaches as well as *ab-initio* methods.

Regarding the CrAs, first we look at the electronic and magnetic properties by using density functional theory (DFT) methods [20]. Then we adopt a modified tight-binding approach that combines the tight-binding approximation and the Löwdin down-folding technique in order to obtain the low energy band structure [21]. We derive a tight-binding model based on the Wannier transformation of the *ab-initio* results and, subsequently, the 'folding' procedure allows us to replace the problem of the diagonalization of the complete full-range tight-binding Hamiltonian with that of an auxiliary matrix whose rank is definitely lower. Löwdin's technique has been successfully applied to, e.g. cuprate superconductors [22], as well as to strontium ruthenate superconductors [23], and it is particularly useful every time one is concerned only with a limited range of energy, e.g. few eV around the Fermi level. This method is

based on the partition of a basis of unperturbed eigenstates into two classes, which are related by a perturbative formula giving the influence of one class of states on the other. We would like to point out that such a procedure is completely consistent with the full *ab-initio* calculations, since its parameters are the *ab-initio* derived overlap integrals for orbitals and the matrix elements. On the other hand, it avoids the complication of the conventional *ab-initio* calculations in cases where the unit cell contains many atoms and allows us to set up an effective Hamiltonian projected on the Cr electronic degrees of freedom and to obtain the analytical expressions for the low energy bands which are ready to be used to evaluate relevant physical quantities.

With our tight-binding-Löwdin procedure we obtain the low energy band structure, the density of states (DOS) and the Fermi surface of CrAs and compare these results with those coming from the *ab-initio* procedure and with the available experimental data, finding a good qualitative agreement with both [21]. Then we analyze some transport properties and the magnetic moment as a function of the Coulomb interaction as well as of the volume of the primitive cell [21, 24]. We take also in consideration the effects of the spin-orbit coupling (SOC) interaction on the electronic properties of the compound [25].

The features of the CrAs, MnP and WP band structures, like the band degeneracies along high symmetry lines, reflect the symmetries of the Pnma space group and in particular the nonsymmorphic glide and screw symmetries. These involve not only point group operations but also non-primitive lattice translations; the glide consists in a reflection respect to a plane and then a translation along a line parallel to that plane, while the screw is the composition of a rotation about an axis and a translation along this axis. These nonsymmorphic systems may exhibit topologically protected Fermi surfaces of reduced dimensionality and have attracted a lot of interest since they can give rise to interesting features involving unconventional energy spectrum, novel topological response phenomena and unusual transport in external magnetic field. Moreover, nonsymmorphic symmetries can enforce the occurrence of unconventional topological phases. Niu et al. [26] substain that the quasilinear magnetoresistance in CrAs is due to an intricate interplay between nontrivial band crossing related to the presence in the crystal of nonsymmorphic symmetries and strong magnetic fluctuations. Daido et al. [27] studied another superconductor of the same family, namely UCoGe, and proposed that the paramagnetic superconducting phase under pressure is a promising candidate of $\mathbb{Z}_4$-nontrivial topological nonsymmorphic crystalline superconductivity enriched by glide symmetry. This very recent research could be extended to CrAs and other related materials to understand if they belong to the family of the $\mathbb{Z}_4$ topological nonsymmorphic crystalline superconductors.

Motivated by these discoveries, we study the symmetry properties of the CrAs, MnP and WP compounds employing DFT supported by the formulation of an effective

low-energy model Hamiltonian. We demonstrate that the eight-fold band degeneracy obtained along the SR path at $(k_x,k_y)=(\pi,\pi)$ is due to inversion-time reversal invariance and a pair of nonsymmorphic symmetries. The presence of multiple degenerate Fermi points along the SR direction constraints the topology of the Fermi surface, which manifests distinctive marks when considering its evolution upon band filling variation. The presence of 2D sheets at some fillings was observed. These 2D sheets could affect the transport and superconducting properties of this class of materials. When the role of the SOC is considered, we show that the interplay between the SOC interaction and the inter-orbital degrees of freedom allows a selective removal of the band degeneracy [28].

Concerning the other family of Cr-based superconductors, the $A_2Cr_3As_3$ compounds, we use tight-binding and DFT methods and we study in great detail the electronic structure of $K_2Cr_3As_3$ [29, 30]. Our results give clear indication that the physics of the system is significantly affected by in-plane dynamics, in spite of the presence in the lattice of well-defined quasi-1D nanotube structures. Then we present a systematic derivation of a minimal five-band tight-binding model, in which taking as a reference the DFT calculation, we use the outcome of a Löwdin procedure to refine a Wannier projection and fully exploit the predominant weight at the Fermi level of the states having the same symmetry of the crystal structure. This model captures very efficiently the energy spectrum of the system and, consequently, can be used to study transport properties, superconductivity and dynamical effects in this novel class of superconductors.

The structure of the thesis is as follows. Chapter 2 is devoted to the study of the electronic, magnetic and transport properties of the CrAs. The first section is about the state of the art. The second section is devoted to the DFT analysis of electronic and magnetic properties. In the third section we describe the analysis of the band structure, the DOS and the Fermi surface throught the application of a combined tight-binding-Löwdin procedure. Also transport and magnetic properties are analyzed. Then we investigate the effects of the SOC interaction on the electronic properties of the compound. Finally we do a discussion of the results obtained.

In Chapter 3 we focus on the symmetries of the systems belonging to the Pnma space group, with a particular enphasis on the nonsymmorphic symmetries that allow to have additional degeneracy in the band structures. In the first section we report the state of the art about the topological condensed matter particularly with regard to these compounds. The second section is devoted to the building up of a simple 2D model Hamiltonian describing these systems. Then, in the third section, we investigate the WP compound and we do a comparison between WP, CrAs and MnP, that are all unconventional superconductors belonging to the Pnma space group. In the

fourth section we generalize the 2D model previously described to a 3D model Hamiltonian that allows us to explain the eight-fold degeneracy of the bands along the SR line. The fifth section is devoted to the effects of nonsymmorphic symmetries on the Fermi surface for WP, CrAs and MnP. The sixth and the last section are dedicated to discussions and conclusions.

Chapter 4 is completely dedicated to the Q1D $K_2Cr_3As_3$ superconductor. Here we use both tight-binding method and DFT approximations in order to obtain a minimal model prefectly describing the low energy band structure. The first section is about the state of the art. The second section is devoted to DFT calculations, while in the third we analyze the electronic properties by using the tight-binding method and then we describe a Löwdin procedure that it is really useful for the construction of the minimal model of the fourth section. The last section is devoted to a discussion of the obtained results. In the last Chapter we draw our general conclusions.

Chapter 2

The pressure induced superconductor CrAs

In this chapter we analyze the electronic, magnetic and transport properties of the superconductor under pressure CrAs. First we describe the electronic and magnetic features via application of the DFT approximation. Then, in the second part we apply a method that combines the tight-binding approximation and the Löwdin down-folding procedure. In such a way we obtain the low energy band structure of the chromium arsenide, namely the effective d bands close to the Fermi level and that partecipate to the conduction. The Fermi surface and the DOS are also investigated. By taking advantage from the so builded low energy Hamiltonian, we study the resistivity and the magnetic moment as a function of the Coulomb interaction and the volume of the primitive cell. Afterward, we present the effects of SOC on the bands and Fermi surface. Finally, we comment on the connections between our results and recent experimental and theoretical proposals. The chapter is organized as follows: in the first section we report the state of the art for the CrAs, the second section is devoted to the DFT calculations and the third to the tight-binding analysis of the electronic, transport and magnetic properties. We also analyze the effects of the SOC interaction on the electronic properties, while in the last section we give our conclusions.

2.1 State of the art

Very recently, pressure-induced superconductivity was discovered in CrAs in the vicinity of the helimagnetic phase [8, 9]. This is the first example of superconductivity found in a Cr-based magnetic system.

CrAs belongs to the family of transition-metal pnictides with the general formula MX (M = transition metal, X = P, As, Sb). It exhibits either a hexagonal NiAs-type (B81) structure or an orthorhombic MnP-type (B31) structure. In particular, CrAs undergoes a phase transition at 800 K from the NiAs-type to the MnP-type configuration. In the latter phase, the unit-cell lattice parameters are a=5.649 Å, b=3.463 Å and c=6.2084 Å [8]. The primitive cell contains four Cr and four As atoms. The

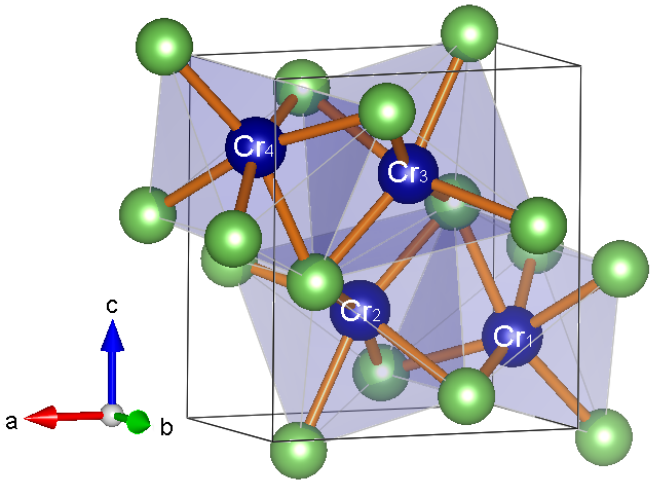

FIGURE 2.1: Crystal structure of the CrAs. Cr and As are shown as blue and green spheres, respectively.

Cr atoms are situated in the centre of $CrAs_6$ octahedra, surrounded by six nearest-neighbour arsenic atoms, as shown in figure 2.1; four of the six Cr–As bonds are inequivalent due to the high anisotropy exhibited by this class of compounds.

At ambient pressure chromium arsenide undergoes a first order phase transition to a non-collinear helimagnetic phase at $T_N \sim 265$ K, where the propagation vector is found to be parallel to the c axis and the magnetic moments lie in the ab plane, as shown by neutron diffraction measurements [31, 32]. The Cr magnetic moment at ambient pressure is 1.7 μ_B and the magnetic structure is formed by four spirals along the c axis, one for every Cr-atom in the primitive cell, with a well defined phase angle between the spirals [31]. Measurements of the magnetic properties versus the pressure indicate that the average ordered magnetic moment decreases from 1.7 μ_B at ambient pressure to 0.4 μ_B at the critical pressure $P_C \sim 0.7$ GPa, where the magnetic order is totally suppressed. Furthermore, Shen et al. [32] showed that CrAs exhibits a spin reorientation in addition to an abrupt drop of the magnetic propagation vector at the critical pressure. At this pressure the system moves from a configuration where the magnetic moments lie in the ab plane to one where they lie in the ac plane [32]. This magnetic phase transition, accompanied by a lattice anomaly, coincides with the emergence of bulk superconductivity. With further increasing pressure, CrAs approaches to the optimal superconductivity regime, where the magnetic moments tend to be aligned antiparallel between nearest neighbor ions [32]. It has been found that the helimagnetic order is also suppressed by phosphorus doping in $CrAs_{1-x}P_x$ at a critical $x_c \sim 0.05$ [33]. A recent analysis of the Al doped CrAs indicates that the pressure-induced superconductivity is almost independent of Al doping [34].

The bulk superconductivity with $T_C \sim 2$ K emerges at the critical pressure $P_C \sim 8$ kbar, where the first-order magnetic transition at T_N is completely suppressed [8]. The superconducting phase, that is realized in the paramagnetic state, has a maximum $T_C \sim 2.2$ K at 1.0 GPa, adopting a dome-like shaped phase diagram [8]. This peculiar diagram is very similar to that of many superconducting systems [35, 36, 37, 38, 39, 40, 41] and it has also been revealed by nuclear quadrupole resonance that the nuclear spin-lattice relaxation rate in CrAs shows substantial magnetic fluctuations, but does not display a coherence peak in the superconducting state [42]. These features suggested a possible unconventional pairing mechanism where the critical spin fluctuations could act as the glue medium for Cooper pairing [8]. Between the helimagnetic and paramagnetic phases, a phase separation is observed [43]. In the vicinity of the critical pressure P_c the internal field in the helimagnetic state maintains a large value and only decreases slowly with increasing pressure, indicating that the pressure-induced suppression of the magnetic order is of the first order [42]. Guo et al. [44] report the angular dependence of the upper critical field under pressure and this analysis suggests the presence of an unconventional odd-parity spin triplet state. In contrast to this vision that shows the CrAs as a possible unconventional superconductor, the phase separation scenario between magnetism and superconductivity, together with the observation that the superfluid density ρ_s scales with the critical temperature as $\sim T_c^{3.2}$, have been interpreted as indicative of a conventional mechanism of pairing [43].

Concerning the transport properties, it has been reported a T^2 temperature dependence of resistivity, i. e. a Fermi-liquid behavior, and found a Kadowaki-Woods ratio equal to $1 \times 10^{-5} \mu\Omega$ cm mol^2 K^2 mJ^{-2}, which fits well to the universal value of many heavy fermion compounds [45]. Moreover, it has been recently shown that CrAs is a bad metal, differently from Cr, a good metal with a room-temperature resistivity far below the Ioffe-Regel limit. The complex interplay between structural, magnetic and electronic properties at T_N is well established in many transition metal compounds and is also expected to be crucial in CrAs in making the external pressure a very effective tool in fine tuning its ground-state [46, 47, 48]. Other resistivity measurements of a CrAs single crystal in a wide temperature range suggest a non phonon mediated superconducting pairing, supporting a magnetic fluctuation mechanism as the likely glue for the superconducting coupling [49].

2.2 DFT analysis of the electronic and magnetic properties

2.2.1 DFT computational details

The DFT calculations have been performed by using the VASP package [50, 51, 52, 53]. In such an approach, the core and the valence electrons have been treated within the Projector Augmented Wave (PAW) method [54] and with a cutoff of 400 eV for the plane wave basis. All the calculations have been performed using a 12×16×10 k-point grid. For the treatment of exchange-correlation, the local density approximation (LDA) and the Perdew–Zunger parametrization [55] of the Ceperly-Alder [56] data have been considered. After obtaining the Bloch wave functions, the maximally localized Wannier functions [57, 58] are constructed using the WANNIER90 code [59]. To extract the Cr 3d and As 4p electronic bands, we have used the Slater–Koster interpolation scheme [59]. In particular, we have fitted the electronic bands, and in this way we have been able to get the hopping parameters and the spin-orbit constants. This approach has been applied to determine the real space Hamiltonian matrix elements in the maximally localised Wannier function basis.

2.2.2 Band structure and DOS

In Fig. 2.2 we report the band structure obtained via DFT approximation [20]. The high symmetry points along which we plot the band structure have been chosen according to the notation quoted in Ref. [60], and the path is represented in Fig. 2.3. First of all, we point out that we have found that this compound does not show any relevant charge transfer, and the oxidation state is basically zero both for Cr and As ions. The Cr atoms are in a d^6 configuration while the As atoms are in a p^3 configuration. Moreover, there are flat bands between –2.0 and +2.0 eV and wider bands out of this range. The presence of flat bands around the Fermi level gives rise to peaks in the DOS. Furthermore, we can also infer a strong anisotropy as observed from the band structure along the Γ-X, Γ-Y and Γ-Z paths. We have also calculated the spin-orbit coupling constant λ for the Cr and As atoms from the real space Hamiltonian. We have found that λ_{Cr}=33 meV for the 3d orbitals of the Cr atoms and λ_{As}= 164 meV for the 4p orbitals of the As atoms. We notice that the spin-orbit coupling of Cr is in good agrement with the value (34 meV) found in another anisotropic environment with monoclinic space group [61].

In Fig. 2.4 we report the DOS, that, from -6.5 eV to -3.5 eV, has a predominant As character, since in this energy range the bands are almost totally occupied by As states. On the other hand, from -3.5 eV to -2.0 eV we find a coexistence of Cr-d and As-p states, whereas from -2.0 eV to +2.0 eV we have essentially Cr bands that are more flat compared to the As bands. The coexistence of unoccupied Cr-d and As-p

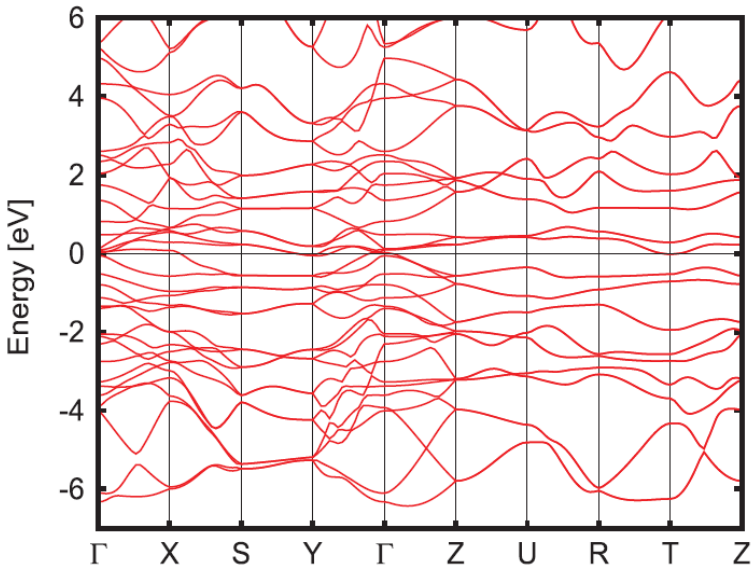

FIGURE 2.2: Band structure of the CrAs at ambient pressure plotted along high-symmetry paths of the orthorhombic Brillouin zone. The Fermi level is set at zero energy.

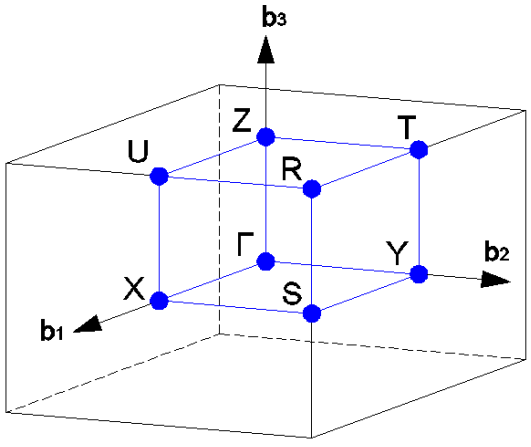

FIGURE 2.3: High-symmetry path in the orthorombic Brillouin zone chosen according to the notation quoted in Ref. [60]

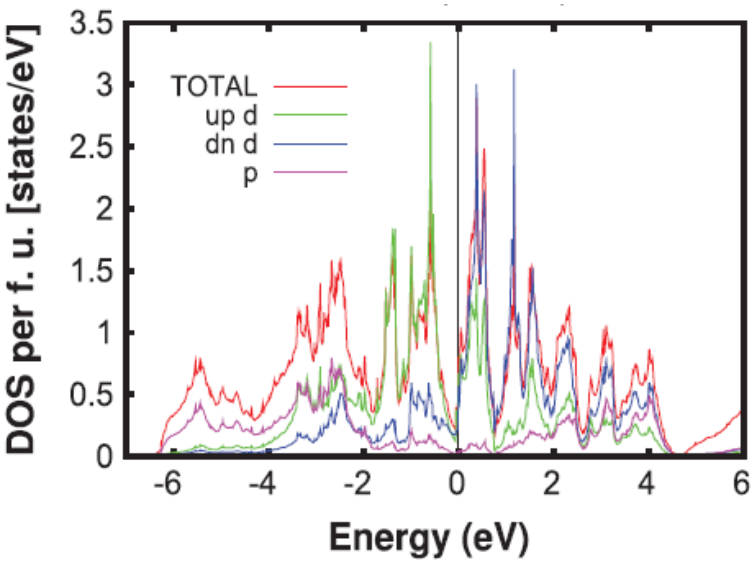

FIGURE 2.4: Total and local DOS of the CrAs at ambient pressure. The total DOS per formula unit is plotted as red. The majority Cr states, minority Cr states and As-p states are plotted as green, blue and pink lines, respectively.

states is found in the range [2.0, 4.5] eV, and finally the bands that originate from 4s electrons of the Cr atoms are located above 4.5 eV. Differently from transition metal oxides, for CrAs we cannot decouple the Cr bands from the As bands. In the Wannier analysis, we cannot disentangle the p-bands from the d-bands since they are not well separated in energy, and this property supports what we can infer from the DOS and the band structure.

2.2.3 Magnetic properties

To investigate the magnetic properties of CrAs, when the external pressure is varied, we have used the atomic positions and the volumes reported in Ref. [32], assuming the orthorhombic MnP-type structure since it is the phase adopted by the CrAs at low temperatures. To scrutinise the magnetisation at lower volumes we have performed a further uniform compression of the lattice constants. In this way we have performed the calculations for the volumes V1–V5, reported in Figure 2.5, where V1 = 123.4 Å^3, V2 = 116.5 Å^3, V3 = 116.2 Å^3 and V4 = V5 = 113.5 Å^3. We point out that the smallest volume of the unit cell for which the experimental data are available is 117.32 Å^3. The variation of the magnetic moment as a function of the volume is reported in Figure 2.5, where we plot the experimental available results [32] together with our theoretical predictions.

In particular, we have calculated the magnetic moment applying the LDA for both the antiferromagnetic case and the ferromagnetic one. Looking at this figure, we infer that the calculations suggest an antiferromagnetic ground state. Indeed, the trend of the magnetic moment, in the ferromagnetic configuration, does not follow

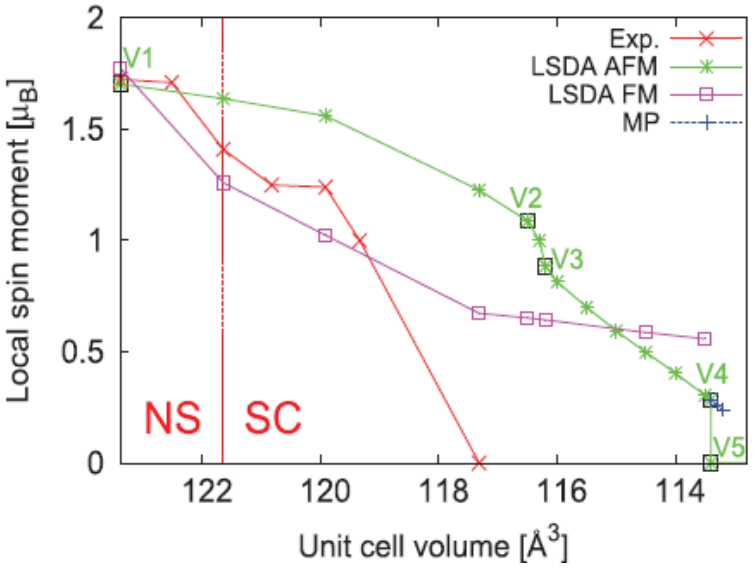

FIGURE 2.5: Evolution of the local magnetic moment of the Cr atoms as a function of the volume of the unit cell within the LDA for the AFM phase (green line), FM phase (pink line) and experimental results [32] (red line). A metastable phase (MP), represented as blue points, has been found at high pressure. We point out that at zero pressure the system is in the normal state (NS). The vertical dashed red line indicates the volume where the superconducting state (SC) comes in. The values of volumes V1–V5 are reported in the text.

the experimental results even though the numerical values of the magnetic moments are comparable to the experimental ones. Concerning the antiferromagnetic results, we can observe a discernible change of the magnetic moment for the volume V5. This variation corresponds to a first-order phase transition between two magnetic phases having different magnetic moment. A metastable phase is also found at the same pressure. When V is equal to V3 the magnetic moment exhibits another discernible change. Having performed an accurate calculation with a large number of k-points, we can state that this change is not a first-order phase transition but an abrupt variation of the magnetic moment. As a final consideration, we would like to point out that the reasonable values found for the magnetic moment without the inclusion of the Coulomb repulsion suggest that the CrAs may be considered as a moderately correlated metallic itinerant antiferromagnet, with a magnetic moment very sensitive to the chosen volume and to the magnetic configuration adopted. The magnetic ground state we find out is a G-type antiferromagnetic state whose behaviour is close to the ground state experimentally reported. Furthermore, we have evaluated the difference between the energy of the ferromagnetic phase E_{FM} and that of the G-type antiferromagnetic phase E_{AFM}, this latter quantity being related to the Néel critical temperature T_N. In the Figure 2.6 we show the evolution of this energy difference as a function of the volume.

We find that E_{FM}-E_{AFM} is +75.25 meV, per formula unit, at zero pressure while its minimum value is –2.46 meV. For volumes larger than 118 Å^3, the system is an antiferromagnet with large T_N, whereas in the experimental superconducting region

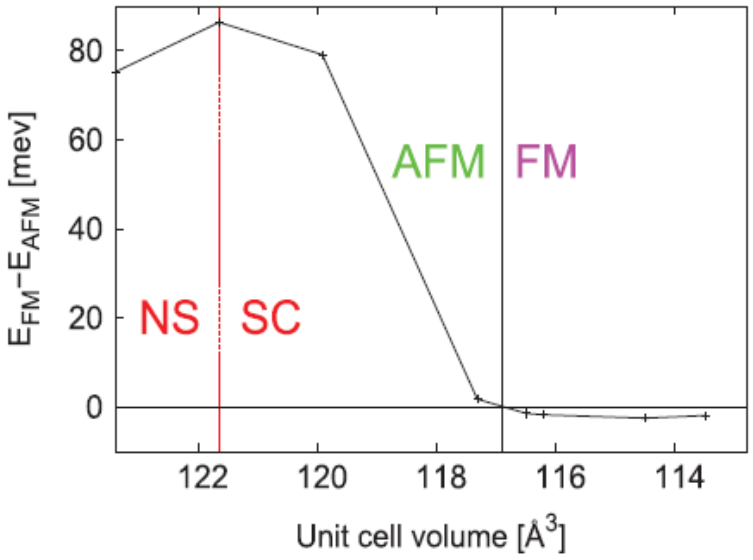

FIGURE 2.6: Energy difference E_{FM}-E_{AFM} per formula unit as function of the volume. In the superconductive region the energy difference gets reduced and the system becomes ferromagnetic.

below 118 Å^3 the magnetic exchange couplings are reduced by a factor 40 respect to the zero pressure case. Below 117 Å^3 the system becomes ferromagnetic with very small exchange coupling. As plotted in Figure 2.5, a non-vanishing magnetic moment is observed at very low volumes but the magnetic order is very week. We also point out that the ferromagnetic ground state configuration appears at volumes below the smallest available experimental volume. Interestingly, we do not have strong evidence of a ferromagnetic phase that could bring towards a triplet superconductivity in a region of the phase diagram.

2.3 Tight-binding analysis of the electronic, transport and magnetic properties

2.3.1 Model Hamiltonian and low energy bands

Here we use a tight-binding model Hamiltonian, in which the hopping parameters are the outcome of DFT calculations [20, 21, 24, 25]. The real space Hamiltonian is the following:

$$H_{sp} = \sum_{i,\alpha,\sigma} \epsilon_i^{\alpha} c_{i\alpha\sigma}^{+} c_{i\alpha\sigma} - \sum_{i,j,\alpha,\beta,\sigma} t_{ij}^{\alpha\beta} (c_{i\alpha\sigma}^{+} c_{j\beta\sigma} + h.c.). \tag{2.1}$$

In the non magnetic phase, the Hamiltonian is the sum of two contributions, the on-site energies ϵ_i at each Cr or As lattice site and the hopping terms of electrons with spin σ between the i and j sites where the Cr or As ions are located and between the

α and β orbitals. H_{sp} stands for single-particle Hamiltonian. The hopping amplitudes $t_{ij}^{\alpha\beta}$ are given by the following integrals:

$$t_{ij}^{\alpha\beta} = \langle \varphi_\alpha(\mathbf{r} - \mathbf{R}_i)|V(\mathbf{r})|\varphi_\beta(\mathbf{r} - \mathbf{R}_j)\rangle, \tag{2.2}$$

where $V(\mathbf{r})$ is the hopping potential, $\mathbf{R}_i$ is the lattice vector associated with the ion position, and $\varphi_\alpha(\mathbf{r} - \mathbf{R}_i)$ are the Wannier functions, forming, for all α and $\mathbf{R}_i$, a complete orthogonal set. The Hamiltonian that describes the system in the non magnetic phase is double degenerate in the spin degree of freedom, therefore we consider only one spin-channel.

As we have already said, the hopping terms comes from the DFT calculations reported in the previous section. The Hamiltonian in Eq. (2.1) is represented by a 32×32 matrix, due to the the fact that, as we have already anticipated, the primitive cell consists of four Cr and four As atoms, and for the chromium ions the orbitals that partecipate to the conduction are the $3d$, while for the arsenic atoms the electrons we are considering belong to the $4p$-orbitals. We can partition the matrix in this way:

$$H = \left[\begin{array}{c|c} H_{CrCr} & H_{CrAs} \\ \hline H_{AsCr} & H_{AsAs} \end{array}\right], \tag{2.3}$$

where H_{CrCr} is a 20×20 submatrix that describes the d-d hoppings among Cr ions, H_{AsAs} is a 12×12 one related to the As p orbitals, and the two sub-matrices H_{CrAs} and H_{AsCr} correspond to the d-p hoppings from Cr to As ions and vice-versa. In our analysis, we limit ourselves to consider atomic shells bringing substantial hopping parameters. As a consequence, we include in our calculations the nearest neighbour hoppings, the second nearest neighbour hoppings along the x-direction and the diagonal part of the second nearest neighbour hoppings along the y and z direction, with the hopping values ranging from 80 meV to 1 eV.

To obtain the full energy spectrum we need to solve the eigenvalue problem for the 32×32 matrix of Eq. (2.3). But we know from *ab-initio* [20] calculations that the As bands are located above and below 2 eV from the Fermi level and this allows us to project out the As $4p$ degrees of freedom using the Löwdin down-folding procedure [22, 62].

The Löwdin technique is based on the partition of a basis of unperturbed eigenstates into two classes $|i\rangle$ and $|j\rangle$, which are related by a perturbative formula giving the influence of one class of states on the other [22]. If we down-fold the H^{jj} block we have:

$$H_{ii'}(\varepsilon) = H_{ii'} - \sum_{j,j'} H_{ij}[(H^{jj} - \varepsilon)^{-1}]_{jj'} H_{j'i'} \,. \tag{2.4}$$

The identical zeros of $det[H - \varepsilon]$ and $det[H^{ii}(\varepsilon) - \varepsilon]$ are the eigenvalues of H. We can Taylor-expand the down-folded Hamiltonian of Eq. (2.4) about ε_F: $H^{ii}(\varepsilon) = H^{ii}(\varepsilon_F) + (\varepsilon - \varepsilon_F)\dot{H}^{ii}(\varepsilon_F) + ...$ The higher-order energy dependence of $H^{ii}(\varepsilon)$ and sometimes even the former energy dependencies can be neglected if the degrees of freedom to be integrated out have high energy, that is, if the energy range of interest lies far away from the eigenvalues of H^{jj}.

In our case, as we have already said, the degrees of freedom to be integrated out are the As-As hybridizations. We can map the 32×32 matrix in one effective $\widetilde{H}_{CrCr}$, whose rank is 20, and that is the following:

$$\widetilde{H}_{CrCr}(\varepsilon) = H_{CrCr} - H_{CrAs}\left(H_{AsAs} - \varepsilon\mathbb{I}\right)^{-1} H_{AsCr} \,. \tag{2.5}$$

In this way we obtain the low energy Hamiltonian, which describes the effective hybridizations Cr-Cr. This Hamiltonian projected into the Cr-subsector cannot be obtained using the Wannier function method. In fact, as we have already said, obtaining an effective Cr-band model for CrAs, and other similar Cr-based superconductors, is highly non trivial, and even though the DFT results for band structure, DOS and Fermi surface are available [20], they are not delivery in a form useful as the single-particle energy spectrum obtained from equation 2.5.

We plot the band structure along the high-symmetry points chosen according to the notation quoted in Ref. [60]. The so obtained low energy bands of CrAs are shown in Fig. 2.7. In the non magnetic phase the spin up and spin down channels are degenerate due to the inversion and time-reversal symmetries. Along some lines of the Brillouin zone (BZ), the bands present an additional degeneracy that we will analyze deeply in the next chapter. If we look at the figure, we observe that the bandwidth is large almost 3.5 eV; there are flat bands between -1.0 and 1.0 eV and wider bands out of this range due to the hybridization with the As bands. The presence of flat bands around the Fermi level gives rise to peaks in the DOS, reported in the next subsection. Furthermore, a strong anisotropy is observed if we look at the band structure along the Γ-X, Γ-Y and Γ-Z paths.

2.3.2 DOS and Fermi surface

The DOS is obtained by using the well-known definition:

$$\rho(\epsilon) = \frac{1}{N}\sum_{\boldsymbol{k}} \delta(\epsilon - \epsilon_{\boldsymbol{k}}), \tag{2.6}$$

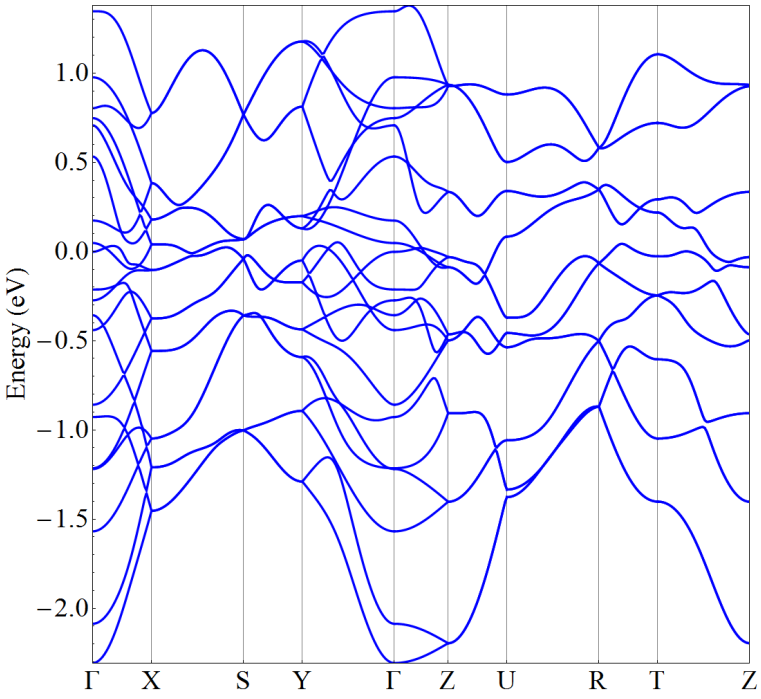

FIGURE 2.7: Low energy band structure of the CrAs plotted along high-symmetry paths of the orthorhombic Brillouin zone. The Fermi level is set at zero energy.

where ϵ is the energy, $\epsilon_{\boldsymbol{k}}$ is the energy dispersion of the Hamiltonian in Eq. (2.5) and the sum is carried out on the N values of $\boldsymbol{k}$ in the BZ. The delta functions in Eq. (2.6) have been approximated by the Gaussian functions:

$$\rho(\epsilon) \approx \frac{1}{N} \sum_{\boldsymbol{k}} \frac{1}{\sigma\sqrt{2\pi}} e^{-\frac{(\epsilon-\epsilon_{\boldsymbol{k}})^2}{2\sigma^2}}, \tag{2.7}$$

where the expected value of the Gaussians is represented by the eigenvalues of the matrix in Eq. (2.5) and the variance is assumed to be $\sigma = 0.012$ eV. The DOS is reported in Fig. 2.8.

From a comparison between our low energy DOS and total and local DOS reported by DTF calculations (Fig. 2.4), we infer that, at the Fermi level, the principal contribution is given by the Cr electrons, which carry more than 90% with a negligible As weight. We have already anticipated that the oxidation state is basically zero both for Cr and As ions and we confirm this result with our tight-binding analysis. The charge transfer from the Cr atoms to the As atoms is around 0.4 electrons per atom, again suggesting that the As spectral weight contribution to the low energy states is very small. The main contribution to the DOS is between -1 eV to +1 eV. The DOS shows its maximum close to the Fermi level, allowing for a magnetic instability even at small values of Coulomb repulsion. The peaks of the DOS at -1 eV and 1 eV are due to some flat Cr bands exhibited by the band structure.

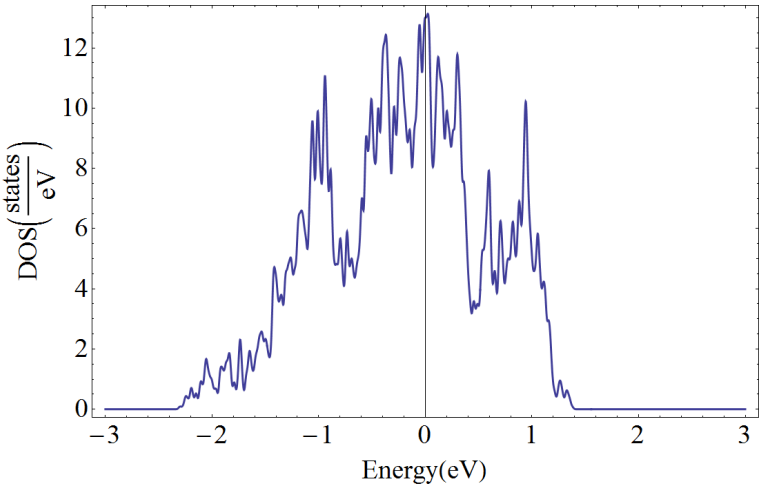

FIGURE 2.8: DOS of the low energy Cr-d bands of CrAs. The Fermi level is set at zero energy.

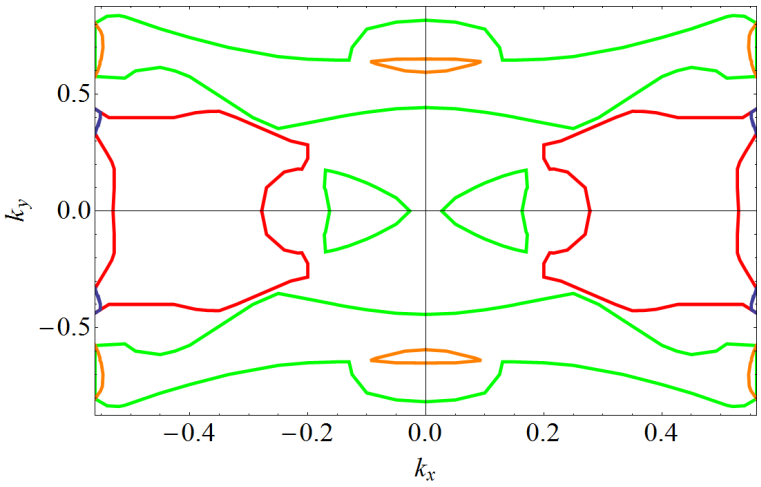

FIGURE 2.9: In-plane Fermi surface of CrAs.

In Fig. 2.9 we show the in-plane Fermi surface. The shape and the pockets are strongly dependent from the magnetic moment of the Cr atoms, in fact when we go from the non-magnetic to the magnetic phase the sheets of the Fermi surface from four become three.

2.3.3 Transport properties

The explicit knowledge of the energy bands allows us to study the transport properties; here we calculate the resistivity as a function of the temperature and we compare our result to the experimental data. In general, to analyze the transport, we need to calculate the current, that is defined as follows:

$$\boldsymbol{J} = e \int \boldsymbol{v} g(\boldsymbol{v}) d\boldsymbol{k}, \tag{2.8}$$

where e and $\boldsymbol{v}$ are the charge and the velocity of electron, respectively, and $g(\boldsymbol{v})$ is the local distribution of electrons. In presence of the external electric and magnetic

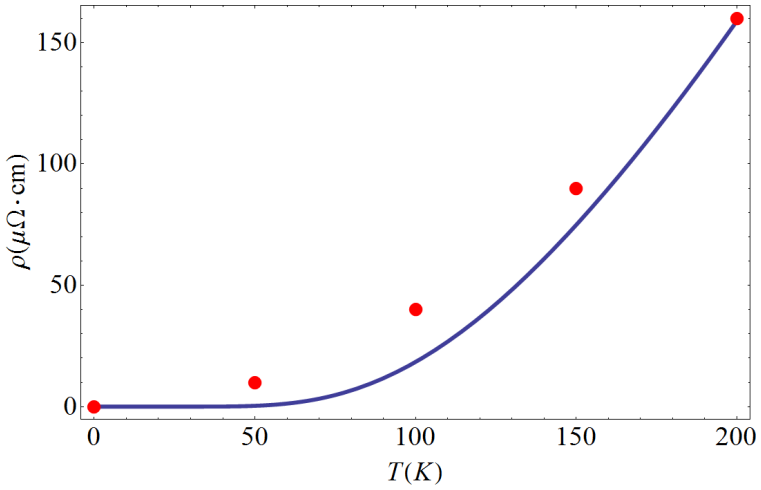

FIGURE 2.10: Temperature dependence of in-plane resistivity. The solid line indicates the outcome of the calculation performed within the Boltzmann theory, while the circles stand for the experimental data from Ref. [8]

fields $\boldsymbol{E}$ and $\boldsymbol{B}$ and expanding up to $\boldsymbol{B}^2$ [63], we obtain:

$$J_\alpha = \sigma^{(0)}_{\alpha\beta} E_\beta + \sigma^{(1)}_{\alpha\beta\gamma} E_\beta B_\gamma + \sigma^{(2)}_{\alpha\beta\gamma\delta} E_\beta B_\gamma B_\delta, \tag{2.9}$$

where the $\sigma^{(0)}_{\alpha\beta}$ tensor is the normal conductivity in absence of external magnetic field. Assuming a cubic environment, the conductivity tensor has the following form:

$$\sigma^{(0)} \equiv \sigma_0 = \frac{e^2}{2\pi^3} \int \tau v_x^2 \frac{\partial f}{\partial \varepsilon} d\boldsymbol{k}, \tag{2.10}$$

in which τ is the relaxation rate and f is the Fermi-Dirac distribution. To plot the temperature dependence of resistivity we need to know the relaxation rate as well as the energy band spectrum [64].

As far as the relaxation times are concerned, we will assume that they depend only on the scattering due to intra and inter-orbital particle-hole correlations, implying a T^2 power law. The result is presented in Fig. 2.10 where we suppose, for simplicity, the same relaxation time for all the bands, i. e. $(\tau)^{-1} = \alpha + \beta T^2$.

2.3.4 Magnetic properties

Now we investigate some magnetic properties of CrAs. In our analysis, we add a local Hubbard term to the tight-binding Hamiltonian as follows:

$$H = H_{sp} + U \sum_{i,\alpha} n_{i\alpha\uparrow} n_{i\alpha\downarrow}, \tag{2.11}$$

where the last term describes the Coulomb repulsion between electrons, with opposite spin on the same lattice site. Since, as mentioned above, the CrAs is a moderately correlated material, we will treat the previous Hamiltonian within the mean-field approximation:

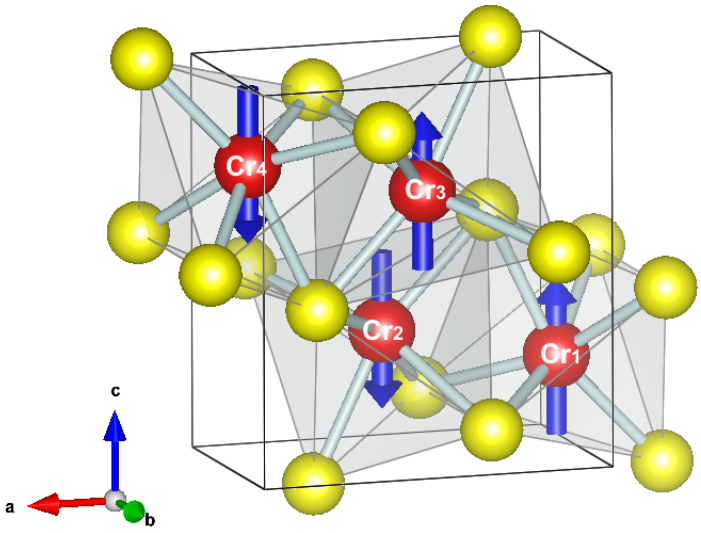

FIGURE 2.11: G-type antiferromagnetic state. Cr and As atoms are shown as red and yellow spheres, respectively, while the arrows represent the spins of the Cr atoms.

$$H = H_{sp} + U \sum_{i,\alpha} \left(n_{i\alpha\uparrow} \langle n_{i\alpha\downarrow} \rangle + n_{i\alpha\downarrow} \langle n_{i\alpha\uparrow} \rangle - \langle n_{i\alpha\uparrow} \rangle \langle n_{i\alpha\downarrow} \rangle \right), \tag{2.12}$$

where $\langle n_{i\alpha\uparrow} \rangle$ and $\langle n_{i\alpha\downarrow} \rangle$ are the average values of the number operator for spin up and down electrons at i lattice site and for the α orbital, respectively.

From DFT calculations, we know that the magnetic ground state in the collinear approximation is a G-type antiferromagnetic state, with antiparallel nearest neighbours spin, shown in Fig. 2.11. Beyond the collinear approximation, CrAs adopts the helical magnetic state.

To obtain the magnetic moment in the G-type configuration, we perform a self-consistent procedure according to the following scheme: we assign initial conditions for $n_{i\alpha\uparrow}$ and $n_{i\alpha\downarrow}$ of Eq. 2.12, and use them to evaluate improved expectation values, this procedure running until convergence with the requested accuracy is achieved.

2.3.5 Magnetic moment as a function of the Coulomb interaction

In Fig. 2.12 we analyze the magnetic moment as a function of the Coulomb interaction.

We assume U varying in the region between 0 and 1.5 eV because the system is metallic and the Fermi screening is expected to reduce the electrostatic repulsion respect to the Coulomb repulsion on the Cr atoms in the insulating systems, which is

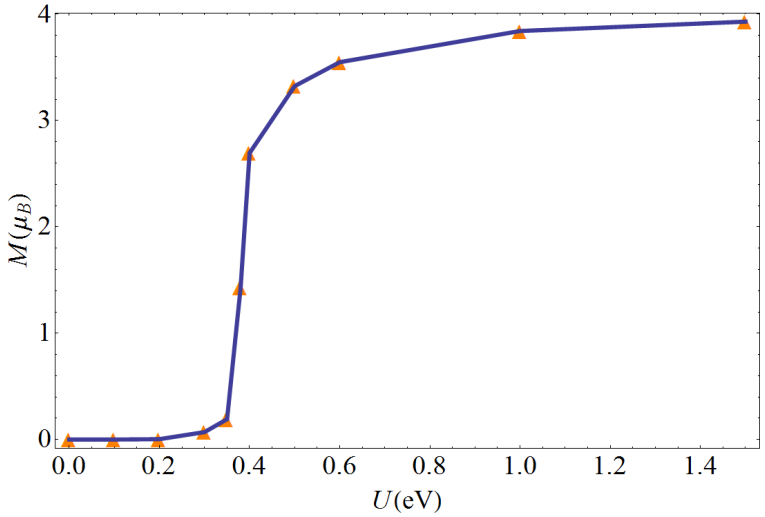

FIGURE 2.12: Magnetic moment evaluated for the mean field Hamiltonian in Eq. 2.12, as a function of the Coulomb interaction. U is measured in eV while the magnetization in Bohr magneton units. The jump in figure can be responsible of the metamagnetism [65, 66].

around 6 eV [61].

Three main regions can be identified, the first is the non-magnetic phase in which the system is up $U \approx 0.3$ eV. Above this value, one enters a crossover region characterized by unsaturated magnetic moment which grows as a function of U. Above ≈ 0.8 eV, the magnetic moment reachs its saturation value of 4 μ_B, because the Cr atoms are in a d^6 configuration.

We have to point out that the experimental data indicate that the CrAs, in its normal phase, is a metallic itinerant antiferromagnet with a very sensitive magnetic moment to the cell volume and to the magnetic configuration adopted [32]. Our results in Fig. 2.12 suggest that the magnetic moment strongly depends on the value of the Coulomb repulsion in the crossover region, as observed experimentally. We speculate that in that regime 0.3 eV $\lesssim U \lesssim$ 0.8 eV , our outcomes show both qualitative and quantitative agreement, the magnetic moment value being consistent with the experimental estimate of 1.73 μ_B [31, 32].

2.3.6 Magnetic moment under pressure

Now we analyze the evolution of the magnetic moment of CrAs under the action of an external pressure. As we have already seen in the previous chapter, Shen et al. [32] reported the experimental data relating to the magnetic moment of the CrAs as a function of the pressure as well as of the lattice constants. In Fig. 2.13 we plot, by using these data, the experimental pressure dependence of the volume of the primitive cell. We use these experimental results as input for our calculations. We simulate the effect of the external pressure acting on the system performing our calculations at different values of volume of the primitive cell.

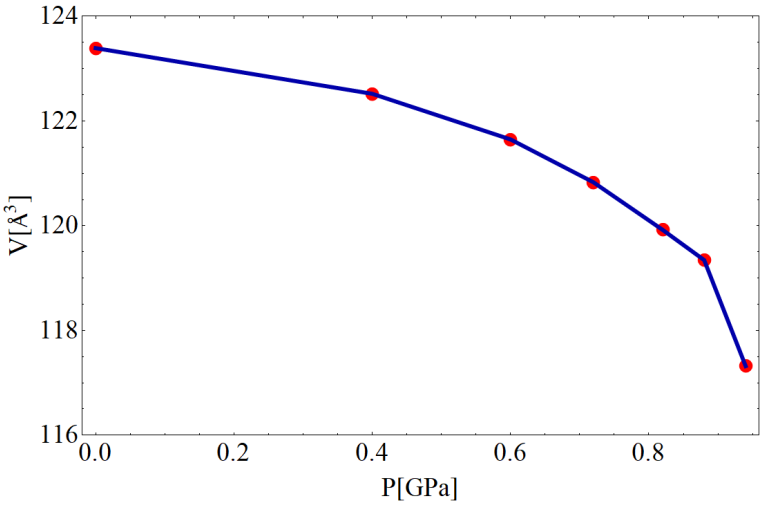

FIGURE 2.13: Volume of the primitive cell of the CrAs as a function of the external pressure acting on the system. The values are those reported in Ref. [32]

The self-consisted method previously descripted is so applied for each chosen value of the external pressure, that corresponds to a precise set of hopping parameters and lattice constants. The value of the Coulomb interaction is fixed at U=0.37 eV, where the experimental magnetization is obtained at ambient pressure. The results of our simulations are reported in Fig. 2.14, together with the available experimental data and the outcomes of the *ab-initio* calculation.

From this figure we notice that a general overall agreement with the experimental data is obtained as far as it concerns both the amplitude of the Cr magnetic moment and its reduction upon applied pressure. According to the results of the previous section, we infer that the magnetic moment reduction could be linked to the increase of the Cr-bandwidth. To clarify this point, we have plotted in Fig. 2.15 the Cr-bandwidth W as a function of the pressure for some values of the Coulomb repulsion, namely U=0.35, 0.37 and 0.39 eV. There are two trends that can be distinguished in Fig. 2.15. Below P=0.8 GPa the bandwidth smoothly decreases with increasing P, with a maximum percentage variation of 3% at 0.6 GPa. In correspondence, the evolution of the magnetization, as shown in Fig. 2.14, is almost constant. For external pressures that exceed P=0.8 GPa, the bandwidth displays a sudden increase corresponding to the dramatic reduction of the local magnetic moment, for all the values of U investigated. We also notice that the minimum of the Cr-bandwidth at P=0.6 GPa coincides with the maximum strength of the antiferromagnetic order. Nevertheless, we mention that other quantities may control the magnetic properties of CrAs, such as the bandwidth of the single bands crossing the Fermi level or the SOC. Furthermore, the magnetic moments of the Cr atoms with shorter distance are antiparallel, indicating a strong antiferromagnetic coupling between these Cr atoms, in agreement with the results here presented. We finally point out that the local magnetic moment, evaluated via the mean-field treatment of the Coulomb repulsion within tight-binding method, shows even a better agreement with the experiments,

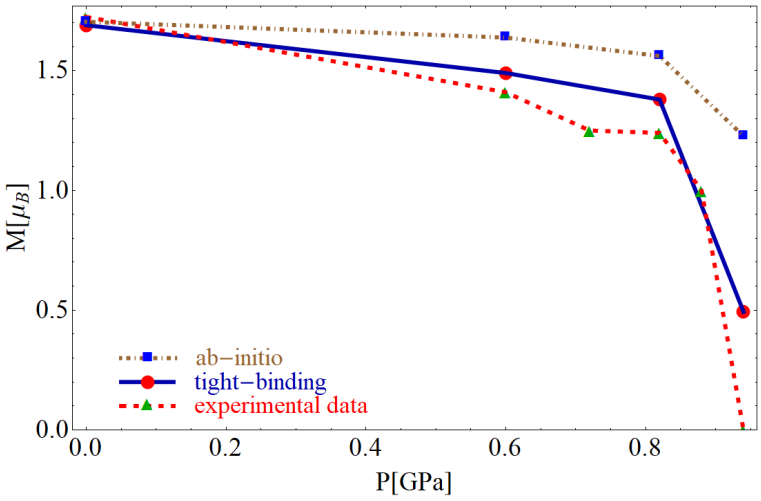

FIGURE 2.14: Magnetization of CrAs as a function of the external pressure. The blue line indicates the theoretical results, the brown dot-dashed line comes from the *ab-initio* simulation [20], while the red dashed line is obtained from the experimental data in Ref. [32]

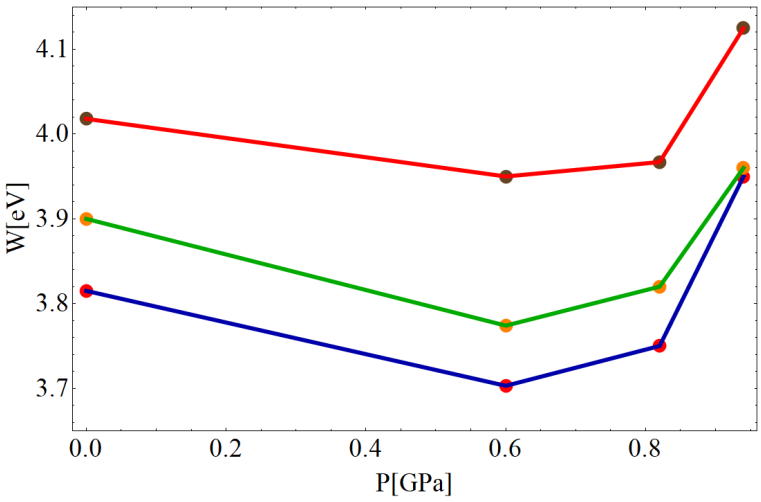

FIGURE 2.15: Bandwidth W of CrAs as function of the pressure for U=0.35 eV (blue line), 0.37 eV (green line) and 0.39 eV (red line).

compared with the LDA calculations reported in the subsection 2.2.3, as shown in Fig. 2.14.

2.3.7 Magnetic couplings

In this subsection we calculate the magnetic couplings and the specific heat of CrAs. For the calculation of the magnetic couplings we have employed *ab-initio* methods. The computational details are those described in the subsection 2.2.1. We have mapped the magnetic couplings on a Heisenberg model [67], that is good for the insulators and is not quite good for the metals. However in this case it is reasonable to use a Heisenberg model because of the high T_N of CrAs. Using the UppASD (Uppsala Atomistic Spin Dynamics) package [68], we have performed Monte Carlo simulations to obtain the specific heat. We took a 16×16×16 supercell based on a Heisenberg-like Hamiltonian:

$$H = \sum_{i,j} J_{ij} \boldsymbol{S}_i \cdot \boldsymbol{S}_j, \tag{2.13}$$

considering the first neighbours exchange couplings, which are denoted as J_a, J_b, J_{c1} and J_{c2} [33], the in-plane second neighbour J_{SNp}, and the second neighbours along c J_{SNc1} and J_{SNc2}, as shown in Fig. 2.16a). In this compound there are two different characteristic Cr–Cr distances along the c-axis, namely 3.090 and 4.042 Å, corresponding to Cr_2-Cr_3 and Cr_1-Cr_4 distances of Cr atoms in Fig. 2.11, and the magnetic coupling between the Cr atoms with shorter distance is strongly antiferromagnetic, while the coupling between Cr atoms with longer distance is weakly ferromagnetic, as shown in Fig. 2.16b). The presence of FM and AFM couplings leads to a frustration that is responsible for the spiral configuration since there is no collinear configuration that satisfies all the bonds of the quadrilateral. In order to reproduce the experimental propagating wave vector Q=(0, 0, 0.356), the stability conditions for the double helical magnetic ground state were already determined by Matsuda et al. [33] as: J_{c2}/J_a=7.1 and J_{c1}/J_a=−0.52, irrespective of the value and sign of J_b. These values have been used by Sen et al. [69] to calculate the linear spin wave spectra of CrAs and the magnon density of states.

However, the values of the exchange couplings have only been estimated from inelastic neutron scattering data on polycrystalline samples [33], there are no theoretical calculations. Therefore, we have performed LDA + U calculations fixing U=1 eV and we have obtained the exchange couplings until the second nearest neighbours. We have also tried the GGA approximation and other U values, but LDA + U with U=1 eV gives us the result closest to the experimental data. The value of U=1 eV is also justified by the fact that the material is supposed to be a moderately correlated compound [20]. The magnetic couplings obtained are reported in Table 2.1 together with the values of Ref. [33].

The experimental propagating wave vector in reciprocal lattice unit is Q=(0, 0, 0.356) [33], while the wave vector obtained with the LDA + U values of the exchange

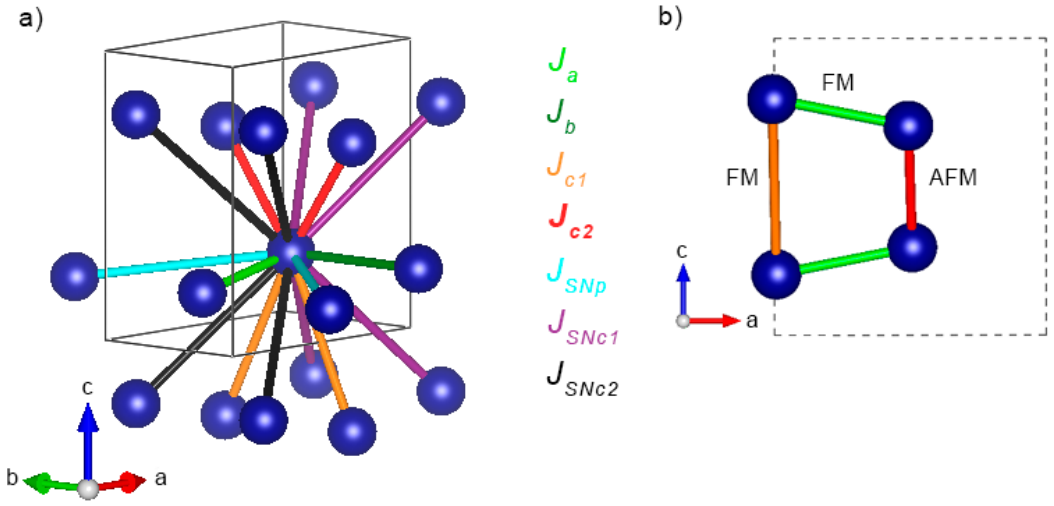

FIGURE 2.16: Magnetic couplings considered in our calculation. In panel a) we show the 3D vision, while in panel b) that in the ac plane where we show the characteristic Cr–Cr distances. With FM we indicate the ferromagnetic coupling, while with AFM the antiferromagnetic one.

	First neighbours				Second neighbours		
Distance	2.857	3.588	4.042	3.090	4.586	4.478	4.574
	J_a	J_b	J_{c1}	J_{c2}	J_{SNp}	J_{SNc1}	J_{SNc2}
LDA + U=1	-19.4	-25.6	-21.9	58.6	5.6	-8.2	-8.2
Ref. [33]	9.27		-4.82	65.0			

TABLE 2.1: In the first line we indicate the distances in Å, in the third and the fourth line we report the values of J obtained with our calculations in LDA approximation and the values of Ref. [33] respectively. J_a, J_b, J_{c1} and J_{c2} are referred to the first neighbours along a, b and c axes; J_{SNp} to the in-plane second neighbour; J_{SNc1} and J_{SNc2} to the second neighbours along c (that are assumed to be equal). The values of J are expressed in meV. The value of the Coulomb repulsion is in eV.

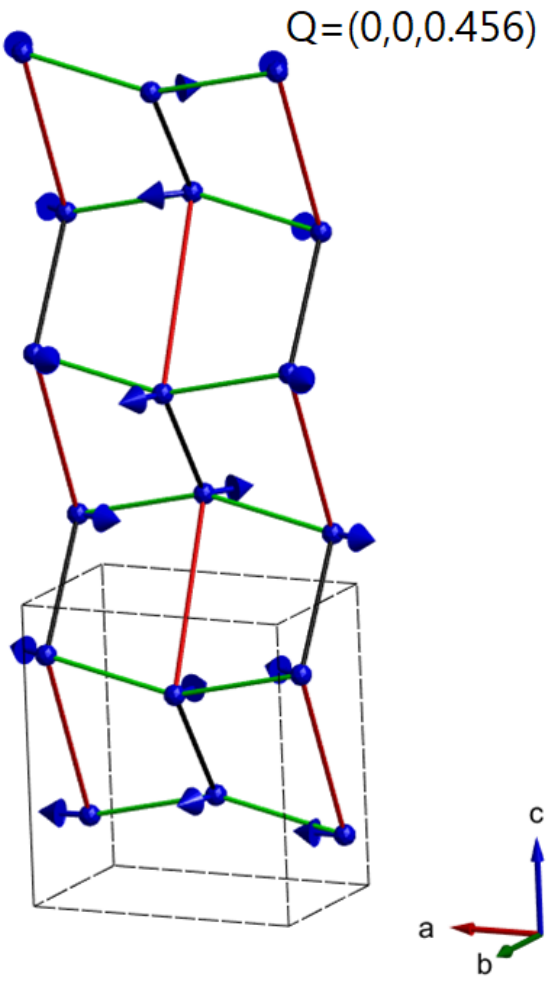

FIGURE 2.17: Double helical structure of CrAs obtained with our data for the exchange couplings.

couplings is Q=(0,0,0.456). This value of Q is close to that reported by Wang et al. [70] for $CrAs_xSb_{1-x}$. The double helical structure achieved is reported in Fig. 2.17; for this calculation the algorithm of Ref. [71] has been used. We also report in Fig. 2.18 the specific heat calculated with the LDA + U values of the exchange couplings, the obtained Neel temperature is T_N=185 K. This value is not so close to the experimental $T_N \sim 265$ K, this means that the compound is too metallic to be studied with a Heisenberg-like model. Although the T_N that we have calculated is not so close to the experimental one, it is similar to that found for $CrAs_{0.5}Sb_{0.5}$ [70]. We want to stress that in this case is very difficult to derive an expression of the exchange constants within perturbation theory in t/U, because U is very small for this system.

2.3.8 SOC interaction

Now we study the effect of the SOC interaction on the electronic properties of CrAs. In order to perform this analysis, we modify the diagonal terms of Hamiltonian of equation (2.5) including the Cr-single-particle on-site SOC term as follows [72]:

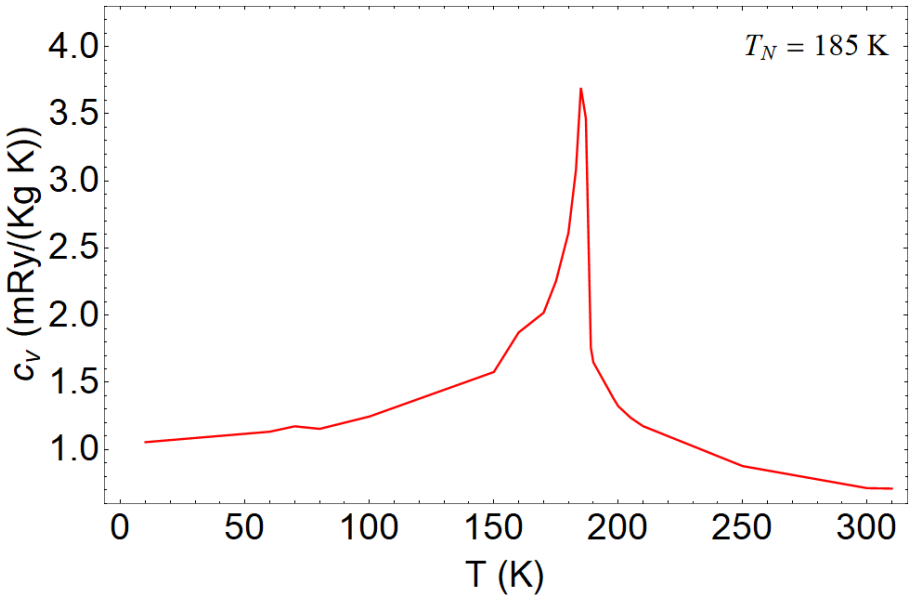

FIGURE 2.18: Specific heat of CrAs as a function of the temperature in LDA + U approximation for U=1 eV.

$$H_{AA}^{SOC} = H_{AA}\sigma_0 + \frac{\lambda}{2}\left(L_x\sigma_x + L_y\sigma_y + L_z\sigma_z\right), \tag{2.14}$$

where σ_0 is the unit matrix in the space of spins, σ_x, σ_y and σ_z are the Pauli matrices, λ is the SOC constant and A=As, Cr depending on the origin for the SOC we want to analyze.

The Hamiltonian can be written in this way:

$$H_{AA}^{SOC} = \begin{pmatrix} H_{AA} + \frac{\lambda}{2}L_z & \frac{\lambda}{2}L_- \\ \frac{\lambda}{2}L_+ & H_{AA} - \frac{\lambda}{2}L_z \end{pmatrix}. \tag{2.15}$$

In the case of the d orbitals, if we use the following basis:

$$\Phi^\dagger = (d^\dagger_{xy,\sigma}, d^\dagger_{yz,\sigma}, d^\dagger_{xz,\sigma}, d^\dagger_{x^2-y^2,\sigma}, d^\dagger_{z^2,\sigma}), \tag{2.16}$$

where $\sigma = \uparrow, \downarrow$, the SOC matrix is:

$$H^d_{SOC} = \begin{pmatrix} 0 & 0 & 0 & i\lambda & 0 & 0 & \frac{1}{2}\lambda & -\frac{i}{2}\lambda & 0 & 0 \\ 0 & 0 & \frac{i}{2}\lambda & 0 & 0 & -\frac{1}{2}\lambda & 0 & 0 & -\frac{i}{2}\lambda & -i\frac{\sqrt{3}}{2}\lambda \\ 0 & -\frac{i}{2}\lambda & 0 & 0 & 0 & \frac{i}{2}\lambda & 0 & 0 & -\frac{1}{2}\lambda & \frac{\sqrt{3}}{2}\lambda \\ -i\lambda & 0 & 0 & 0 & 0 & 0 & \frac{i}{2}\lambda & \frac{1}{2}\lambda & 0 & 0 \\ 0 & 0 & 0 & 0 & 0 & 0 & i\frac{\sqrt{3}}{2}\lambda & -\frac{\sqrt{3}}{2}\lambda & 0 & 0 \\ 0 & -\frac{1}{2}\lambda & -\frac{i}{2}\lambda & 0 & 0 & 0 & 0 & 0 & -i\lambda & 0 \\ \frac{1}{2}\lambda & 0 & 0 & -\frac{i}{2}\lambda & -i\frac{\sqrt{3}}{2}\lambda & 0 & 0 & -\frac{i}{2}\lambda & 0 & 0 \\ \frac{i}{2}\lambda & 0 & 0 & \frac{1}{2}\lambda & -\frac{\sqrt{3}}{2}\lambda & 0 & \frac{i}{2}\lambda & 0 & 0 & 0 \\ 0 & \frac{i}{2}\lambda & -\frac{1}{2}\lambda & 0 & 0 & i\lambda & 0 & 0 & 0 & 0 \\ 0 & i\frac{\sqrt{3}}{2}\lambda & \frac{\sqrt{3}}{2}\lambda & 0 & 0 & 0 & 0 & 0 & 0 & 0 \end{pmatrix}. \tag{2.17}$$

In the case of the p orbitals, if we use the following basis:

$$\Phi^\dagger = (p^\dagger_{x,\sigma}, p^\dagger_{y,\sigma}, p^\dagger_{z,\sigma}), \tag{2.18}$$

where $\sigma = \uparrow, \downarrow$, the SOC matrix is:

$$H^p_{SOC} = \begin{pmatrix} 0 & -\frac{i}{2}\lambda & 0 & 0 & 0 & \frac{1}{2}\lambda \\ \frac{i}{2}\lambda & 0 & 0 & 0 & 0 & -\frac{i}{2}\lambda \\ 0 & 0 & 0 & -\frac{1}{2}\lambda & \frac{i}{2}\lambda & 0 \\ 0 & 0 & -\frac{1}{2}\lambda & 0 & \frac{i}{2}\lambda & 0 \\ 0 & 0 & -\frac{i}{2}\lambda & -\frac{i}{2}\lambda & 0 & 0 \\ \frac{1}{2}\lambda & \frac{i}{2}\lambda & 0 & 0 & 0 & 0 \end{pmatrix}. \tag{2.19}$$

2.3.9 SOC effects on the band structure and Fermi surface

Here we will analyze the effect of the inclusion of the SOC on the electronic band structure and Fermi surface of CrAs. We assume the SOC terms on the Cr and As ions are relevant for describing the electronic structure, due to the significant degree of covalency between the $3d$ and $4p$ orbitals. We will consider first the effects on the bands of a SOC due to As and Cr atoms separately, and then simultaneously.

The tight-binding Hamiltonian describing the system in absence of SOC presents several symmetry properties. First of all, the system is symmetric under the action of the time-reversal operator $\hat{T}$, which generates the time-symmetry transformation. Moreover, it is also symmetric under the unitary inversion operator $\hat{P}$, that inverts the sign of the in-plane spatial coordinates. Therefore, the $\hat{P}\hat{T}$ combination allows to have an antiunitary symmetry that is local in momentum space and implies that the energy eigenstates realize bands which are twofold degenerate at any $\boldsymbol{k}$ vector in the BZ. This Kramers degeneracy sets to 20 the maximal number of bands, each with a 2-fold degeneracy. Other than inversion and time-reversal, the system presents additional nonsymmorphic symmetries, that involve not only point group operations

but also non-primitive lattice translations, and which we will discuss in more detail in the next chapter. These symmetries allows to have additional degeneracies of the bands along some lines of the BZ.

In order to analyze how the SOC may affect the features of the band structure, we first observe that SOC does not break the time-reversal symmetry, so that the Kramers degeneracy is preserved. Let us first consider the action of the SOC only on the As-p orbitals. From the DFT calculations reported in the previous section, we know that the As SOC coupling constant is λ_{As}=0.164 eV.

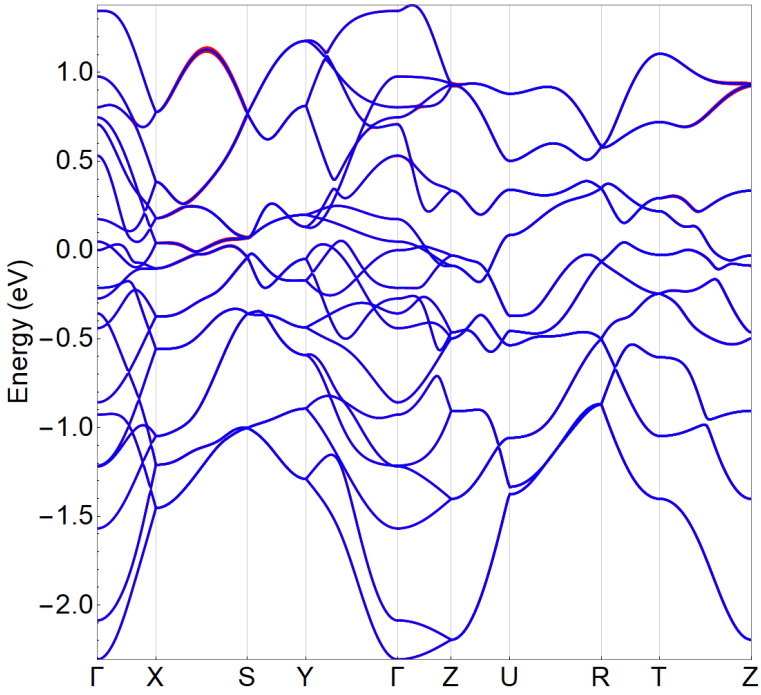

FIGURE 2.19: Comparison between the low-energy bands of CrAs without SOC (blue) and the modified bands with the action of the SOC on the 4p orbitals of the As atoms (red).The value of the SOC constant used is λ_{As}=0.164 eV. The Fermi level is set at zero energy.

In Fig. 2.19 we show the effects of the SOC related to the arsenic degrees of freedom if this value of the coupling constant is considered.

In blue are represented the bands without SOC and in red that under the action of SOC. However, since we have really small effects on the bands taking this value of the coupling constant, we choose to emphasize the value of λ_{As} by assuming λ_{As}=0.3 eV, in order to highlight the regions of the energy spectrum that are more affected by the As SOC term, and this case is reported in Fig. 2.20.

We notice that the arsenic SOC contribution to the low energy bands of CrAs is rather weak, and it mainly interests the bands far from the Fermi level, even when a larger value of λ_{As} is assumed. Furthermore, we observe that the four-fold degeneracy

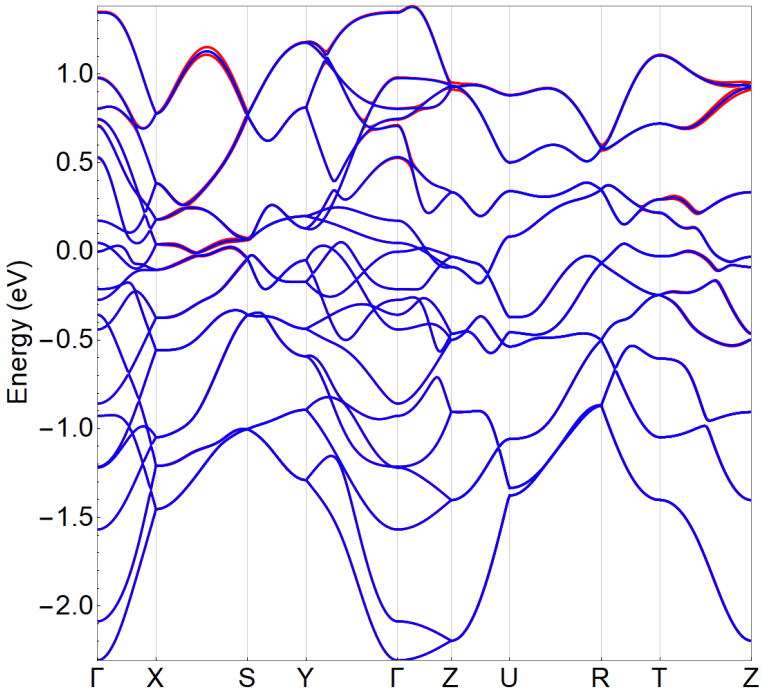

FIGURE 2.20: Comparison between the low-energy bands of CrAs without SOC (blue) and the modified bands with the action of the SOC on the $4p$ orbitals of the As atoms (red). The value of the SOC constant used is λ_{As}=0.3 eV. The Fermi level is set at zero energy.

is partially removed along the XS and TZ paths, in fact the SOC brings the degeneracy along these lines from four-fold to two-fold. The splitting of the bands along these directions is the order of 10^{-2} eV.

As next step, the effect of the SOC on the Cr degrees of freedom have been considered, by modifying the Cr-Cr part of the Hamiltonian of equation 2.5 and then performing the Löwdin procedure, to down-fold the H_{AsAs} matrix. The DFT calculations, as said in the previous section, give a value of λ_{Cr}=0.033 eV.

Also for the Cr degrees of freedom we show the modifications to the band structure obtained under the action of SOC in two cases, first if the DFT value of the coupling constant λ_{Cr}=0.033 eV is used, and this is reported in Fig. 2.21, and second by assuming λ_{Cr}=0.06 eV, in order to highlight the regions of the energy spectrum that are more affected by the Cr SOC term, and this is reported in Fig. 2.22.

From an inspection to thes figures, we infer that the Cr SOC affects the bands near the Fermi level, implying that this effect may be relevant on the transport properties of the CrAs. We point out that this change underlines the fact that the bands close to the Fermi level are mainly due to the chromium orbitals. Also in this case, the SOC causes a partial removal of the degeneracy, from a 4-fold to a 2-fold, along the XS and TZ high-symmetry lines of the orthorhombic BZ. The effect is more evident than when we consider the arsenic degrees of freedom even if the Cr-SOC constant is

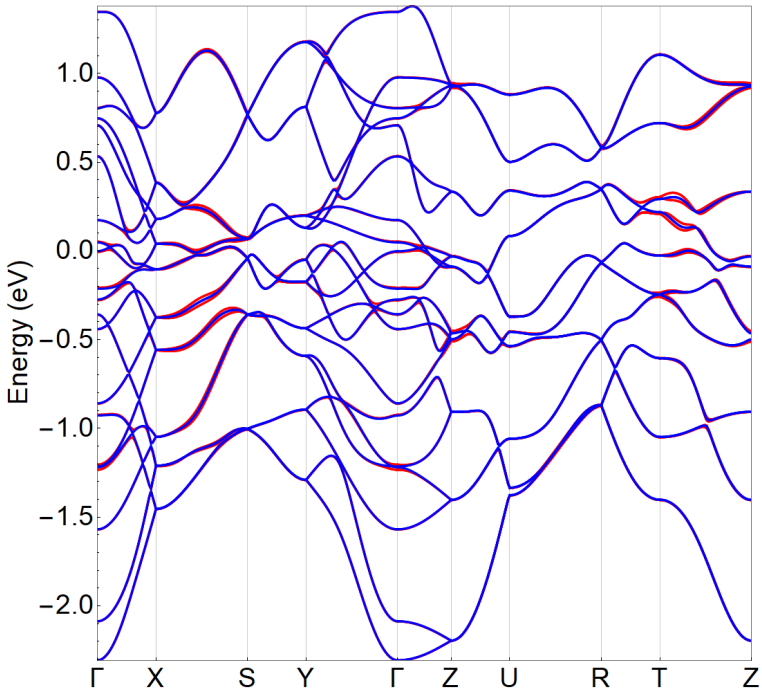

FIGURE 2.21: Comparison between the low-energy bands of CrAs without SOC (blue) and the modified bands after the action of the SOC on the $3d$ orbitals of the Cr atoms (red). The value of the SOC constant used is λ_{Cr}=0.033 eV. The Fermi level is set at zero energy.

smaller than that related to the As ions, this is once again due to the fact that the low energy bands have principally Cr origin.

The last step consists in considering both the Cr and As origin for the SOC. We choose as values of the coupling constants that given by the DFT analysis, namely λ_{Cr}=0.033 eV and λ_{As}=0.164 eV. The modifications of the bands when both Cr and As SOC are considered are shown in Fig. 2.23. The overall effect is a degeneracy removal that corresponds to an energy splitting of the order of 10^{-2} eV, taking place on the above mentioned high-symmetry lines of the BZ.

In Table 2.2, we summarize the modification in the bands degeneracy induced by the SOC, along each line of the orthorombic BZ. We can see that the inclusion of the SOC determines a partial removal of the degeneracy of the bands along two lines of the BZ, the XS (where $k_x = \pi/a$ and $k_z = 0$, while varying k_y) and TZ (where $k_x = 0$ and $k_z = \pi/c$, while varying k_y). Along these lines the degeneracy that comes from the nonsymmorphic crystal symmetries is removed, but not that related to the inversion-time reversal symmetry, in fact the band structure passes from a 4-fold to a 2-fold degeneracy. The non-trivial interplay between the SOC and the non-symmorphic crystal symmetries, which underlies this selective degeneracy removal can be found more in the detail in the next chapter.

Since the SOC is acting by splitting the 4-fold band degeneracy, it is plausible to expect that the Fermi surface topology will be strictly affected, by disconnecting

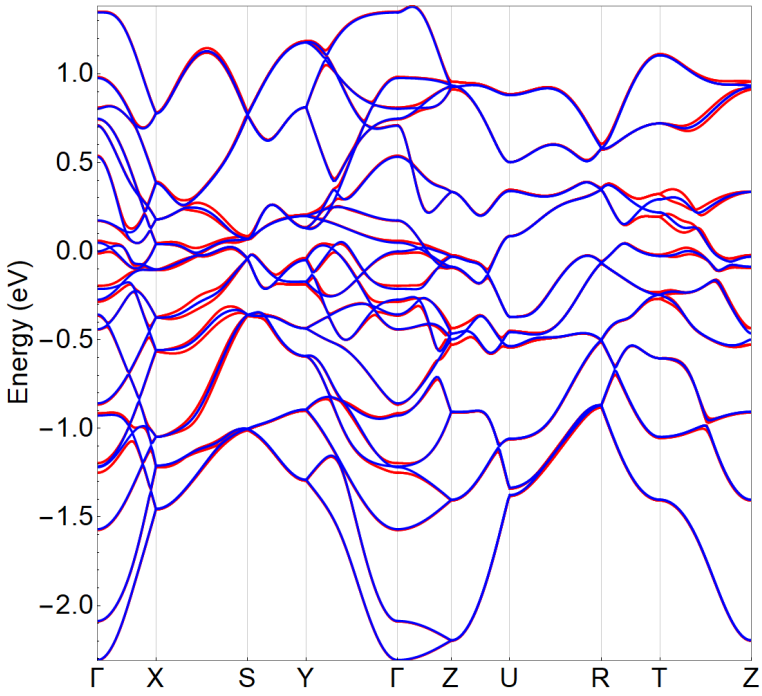

FIGURE 2.22: Comparison between the low-energy bands of CrAs without SOC (blue) and the modified bands after the action of the SOC on the $3d$ orbitals of the Cr atoms (red). The value of the SOC constant used is λ_{Cr}=0.06 eV. The Fermi level is set at zero energy.

the pockets that were constrained by the crystal symmetry to cross each other along those high-symmetry lines. In Fig.2.24, we show the representative case of the in-plane Fermi surface at $k_z = 0$, obtained when a SOC term acting both on the Cr and on the As atoms is considered (dashed lines), as compared to the one obtained without the inclusion of the SOC (solid lines). The *ab-initio* values for the constants, namely λ_{Cr}=0.033 eV and λ_{As}=0.164 eV, have been used.

In absence of SOC, the Fermi surface consists of four sheets, and is characterized by the presence of four pockets along XS, which are two at a time degenerate at four specific k_y values. The energy splitting induced by the SOC along this path has two main effects. First of all, by lowering one of the bands below the Fermi level, it causes the removal of the small electron pockets located at ($k_x = \pi/a, k_y \simeq 0.5$ Å^{-1}) (blue pockets). Moreover, the residual pockets are no longer constrained by the crystal symmetry to be connected, so they get separated and cut the XS path at eight different k_y values. We would also like to point out that the modification to the Fermi surface is essentially due to the Cr part of the SOC, once again supporting the conjecture that the bands near the Fermi level are mainly due to the Cr orbitals. In this analysis we studied the effect of the SOC interaction for the spin-unpolarised system. If the spin-orbit coupling were included when the system is spin-polarised, the situation would be more complicated, because we would have not only the spin-splitting due to the SOC but also a splitting due to the magnetism.

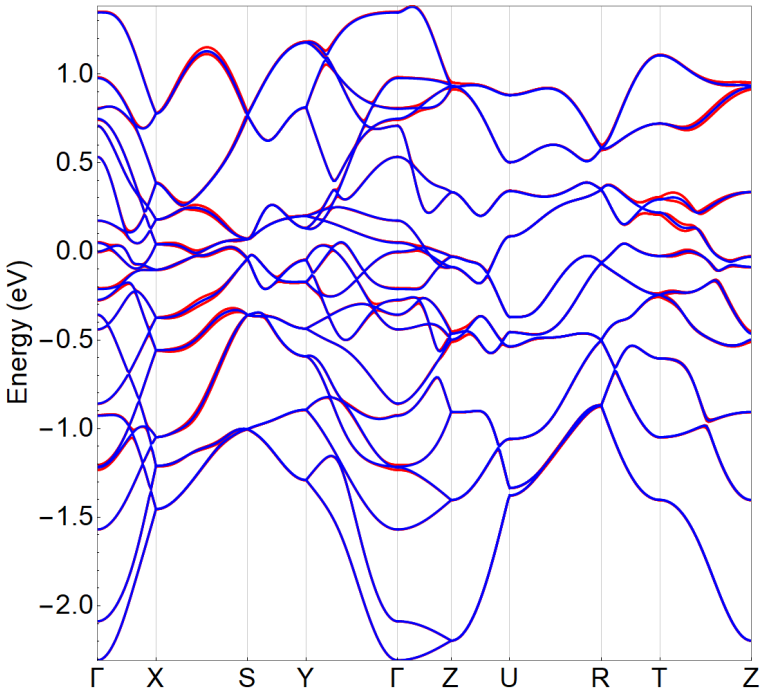

FIGURE 2.23: Comparison between the low-energy bands of CrAs without SOC (blue) and the modified bands after the action of the SOC both on the Cr and on the As part of the Hamiltonian (red). The values of the SOC constants used are λ_{Cr}=0.033 eV and λ_{As}=0.164 eV. The Fermi level is set at zero energy.

2.4 Conclusions

We have used a combined tight-binding-Löwdin down-folding approach to calculate the low energy bands, the DOS and the Fermi surface of CrAs [21]. The low energy Cr-bands turns out to be readily used in calculating physical quantities depending on the explicit form of the energy spectrum, as for instance the in-plane resistivity. We have also evaluated the Cr magnetic moment as a function of the Coulomb interaction [21] and its value under pressure [24]. We found a good qualitative agreement with the available experimental data. Furthermore, the effects of the SOC interaction on the bands and on the Fermi surface have been studied [25]. Here we have used the simplest possible tight-binding model including the hopping integrals between only nearest and next nearest neighbors and we have down-folded the Hamiltonian projection on the p As subspace by using the Löwdin procedure. This analytical formula for low energy bands can be used to analyze physical quantities where the topology of Fermi surface is important, could allow us to explore the superconducting instability within the standard broken-symmetry Hartree-Fock scheme and can be useful as the single-particle term in more sophisticated Hamiltonians containing for instance Coulomb correlations. As we have already said in the previous sections, even if *ab-initio* calculations are available, they are rather complicated and are not delivered in a form useful as the single-particle term of a model Hamiltonian of Eq. (2.5), that

High-symmetry line	k_x	k_y	k_z	Tight-binding	Löwdin	Löwdin with SOC
ΓX	k_x	0	0	2	2	2
XS	$\frac{\pi}{a}$	k_y	0	4	4	2
SY	k_x	$\frac{\pi}{b}$	0	4	4	4
YΓ	0	k_y	0	2	2	2
ΓZ	0	0	k_z	2	2	2
ZU	k_x	0	$\frac{\pi}{c}$	4	4	4
UR	$\frac{\pi}{a}$	k_y	$\frac{\pi}{c}$	4	4	4
RT	k_x	$\frac{\pi}{b}$	$\frac{\pi}{c}$	4	4	4
TZ	0	k_y	$\frac{\pi}{c}$	4	4	2

TABLE 2.2: Evolution of the bands degeneracy along high symmetry lines in the BZ, with the introduction of the SOC term. Along each line, one component of $\boldsymbol{k}$ varies and the other two are kept fixed. We indicate in the first column the high-symmetry lines of the BZ; in the second, third and fourth columns the values assumed by the components of $\boldsymbol{k}$; in the fifth column, we report as a comparison, the degeneracy value obtained in the pure tight-binding procedure; the sixth and the seventh columns show the band degeneracy without and with the inclusion of the SOC.

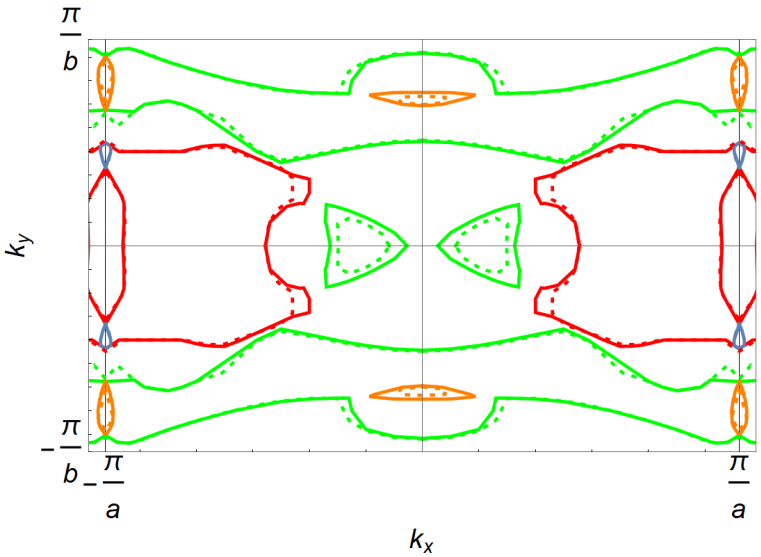

FIGURE 2.24: SOC effects on the in-plane Fermi surface at $k_z = 0$ of CrAs, obtained for λ_{Cr}=0.033 eV and λ_{As}=0.164 eV. The different colors indicate the different bands that cross the Fermi level while the dotted line represents the modified Fermi surface by the SOC.

describes the low-energy excitations. The good agreement of these results with the experiments both for the resistivity and for the magnetic moment suggest that CrAs is a moderately correlated compound that can be well described in a tight-binding approach.

Concerning the SOC interaction, both the Cr and the As degrees of freedom have been considered. The main effect of the inclusion of the SOC term in our model Hamiltonian is the removal of the band degeneracy along the XS and TZ lines of the orthorhombic BZ. The splitting of the bands along these directions is the order of 10^{-2} eV. We demonstrated that the SOC term determines a modification in the topology of the Fermi surface. In particular, the energy splitting of the bands under the action of the SOC affects the small electron pockets located along XS and TZ paths, which get suppressed once the constraint of the band 4-fold degeneracy is released. We are able to ascribe to the $3d$ orbitals of the chromium this effect, further supporting the conjecture that the spectral weight of the d band near the Fermi level is larger than the p-band corresponding one. In the next chapter we will investigate more deeply the topic of the band crossings protected by nonsymmorphic symmetries, that have attracted a lot of interest since they can give rise to unconventional dispersions, novel topological response phenomena and unusual transport in external magnetic field.

Chapter 3

Multiple band crossings and Fermi surface topology in MnP-type crystal structures

In this chapter we analyze the symmetry properties of the compounds belonging to the Pnma space group, in particular those with the MnP-type crystal structure. MnP is a subgroup of the Pnma space group in case there are two different atoms. These compounds present not only inversion and time-reversal symmetries, but also nonsymmorphic symmetries associated with the glide planes and screw axes. First, we build up a model Hamiltonian aimed at the analysis of the different kinds of symmetries in these compounds in the simpler 2D case. Then, by using relativistic *ab-initio* methods combined with a model Hamiltonian approach, we focus on the normal-phase electronic and structural properties of the recently discovered WP superconductor. The outcomes of such study can be employed to set fundamental connections among WP and the CrAs and MnP superconductors belonging to the same space group. In particular, we demonstrate that the eight-fold band degeneracy obtained along the SR path at $(k_x,k_y)=(\pi,\pi)$ is due to inversion-time reversal invariance and a pair of nonsymmorphic symmetries. This demonstration is done with a 3D model Hamiltonian which it is built starting from the 2D Hamiltonian previoulsy described. The presence of multiple degenerate Fermi points along the SR direction constraints the topology of the Fermi surface, which manifests distinctive marks when considering its evolution upon band filling variation. Finally, we comment on the connections between our results and recent experimental and theoretical proposals about the triplet superconductivity in this class of compounds. The chapter is organized as follows: the first section is devoted to the state of the art in topological condensed matter and also about the compounds of the Pnma space group with MnP-type crystal structure, in the second section we present our 2D model Hamiltonian, in the third section we study of the structural and electronic properties of the WP and the comparison with those of CrAs and MnP. In the fourth section we present a 3D model Hamiltonian that is the generalization of the 2D previously reported and that allows us to explain the eight-fold degeneracy along the SR line, in the fifth one we investigate the effects of the nonsymmorphic symmetries on the Fermi surface in these compounds, the sixth

and the last sections are devoted to discussions and conclusions.

3.1 State of the art

Recent years have testified an increasing interest in the study of nodal metals with protected band degeneracies near the Fermi level, especially due to the rapid development of the field of topological condensed matter [73, 74, 75, 76, 77, 78, 79, 80, 81, 82, 83, 84, 85, 86, 87, 88, 89, 90, 91, 92, 93]. Topological gapless phases are marked by topologically protected Fermi surface which occur as a consequence of band crossings associated with a topological number that in turn is tied to the symmetries enforcing the band degeneracy. The significant advancements in the classification schemes based on topology and in materials predictions led to the discovery of a wide number of topological semimetals (SMs) that include both Dirac [94] and Weyl SMs [95, 96, 97], nodal line [98, 99, 100], type-I and type-II SMs [101], multifold SMs [102].

It is well known that crystals degeneracies can also come from non point-group types of symmetries. For instance, nonsymmorphic crystalline symmetries, namely symmetries that involve not only point group operations but also non-primitive lattice translations, typically force bands to cross and can enforce the occurrence of unconventional topological phases [95, 103, 104, 105, 106, 107, 108, 109, 110, 111, 112, 113].

Nonsymmorphic symmetries when combined with inversion, time or particle-hole symmetry transformations [114], can allow band degeneracies at the origin or at the boundary of the BZ [103]. Moreover, such nonsymmorphic nodal systems can also exhibit topologically protected Fermi surfaces of reduced dimensionality, as well as topological response phenomena with non-standard magnetotransport properties [27, 103, 115].

Among the materials exhibiting nonsymmorphic crystal symmetries, a remarkable case is represented by CrAs, especially in view of the promising possibility to combine nonstandard nodal electronic states with magnetic and superconducting orderings [116, 117, 118]. A member of the same family is the MnP that shares with CrAs a superconducting phase driven by external pressure and akin to the magnetism, suggesting a new form of superconductivity with nonconventional order parameter [7, 8, 9, 11]. In both compounds the critical temperature-external pressure phase diagram has a typical dome-shaped behavior [9, 31, 35, 38, 42, 43] with the superconductivity appearing at the critical pressure P equal to 0.7 GPa for CrAs and 8 GPa for MnP, where the helimagnetic transition is suppressed [8, 11]. Another common and salient feature of the phase diagram of these compounds is the presence of tunable magnetic phases that can coexist with superconductivity [43], exhibit different types of ordered patterns (e.g., helimagnetism in CrAs [8, 119] and metamagnetism [65, 66],

ferromagnetism, and helimagnetism in MnP [120, 121, 122, 123, 124]), exhibit non-standard magnetic anisotropy [31, 32], or undergo a variety of phase transitions upon cooling [124], doping [33], and application of external pressure [42]. Very recently, Liu et al. [12] found a new superconductor, namely, WP, belonging to this class of transition-metal pnictides, with a bulk superconductivity appearing at 0.84 K, at ambient pressure [12]. Remarkably, WP is the first $5d$ transition-metal phosphide with a nonmagnetic ground state. The extended $5d$ shells lead to a strong coupling between the W d orbitals and the neighboring p orbitals, giving rise to a crystal structure more distorted than that of CrAs and MnP. Moreover, the W-$5d$ electrons exhibit spin-orbit coupling interaction stronger than the $3d$ electrons of CrAs and MnP.

3.2 Nonsymmorphic symmetries in the MnP-type crystal structures: a 2D model Hamiltonian

We present in this section a 2D model Hamiltonian that will then be generalized to the 3D case. This model will allow us to study properties of the bands and Fermi surfaces that we will find in the next sections concerning materials of the Pnma space group with MnP-type crystal structure like WP, CrAs and MnP.

Let us consider the 2D crystal structure and the hopping parameters reported in Fig 3.1. We will study the electronic and symmetry properties of this system in different cases, given by the conditions imposed on the hoppings. For simplicity the nearest hoppings between the same atoms A-A, B-B, C-C, D-D along the y direction, that we have considered in the calculations (namely $t_{AA} = t_{BB} = t_{CC} = t_{DD}$), are not shown in the picture.

The Hamiltonian describing the system is a spin-degenerate 4×4 matrix:

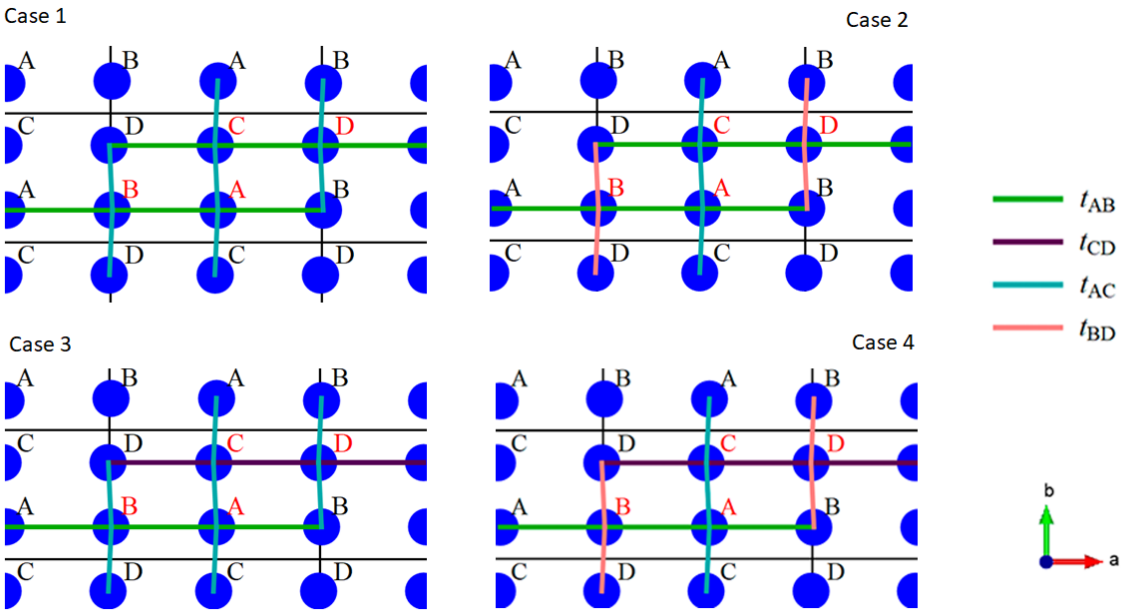

FIGURE 3.1: Crystal structure and hopping parameters considered. The red letters indicate the atoms of the primitive cell (0,0).

$$
\begin{aligned}
H(k_x,k_y) = &\begin{pmatrix} \varepsilon & t_{AB} & t_{AC} & 0 \\ t_{AB} & \varepsilon & 0 & 0 \\ t_{AC} & 0 & \varepsilon & t_{CD} \\ 0 & 0 & t_{CD} & \varepsilon \end{pmatrix} + e^{ik_x} \begin{pmatrix} 0 & t_{AB} & 0 & 0 \\ 0 & 0 & 0 & 0 \\ 0 & 0 & 0 & 0 \\ 0 & t_{BD} & t_{CD} & 0 \end{pmatrix} + \\
&+ e^{-ik_x} \begin{pmatrix} 0 & 0 & 0 & 0 \\ t_{AB} & 0 & 0 & t_{BD} \\ 0 & 0 & 0 & t_{CD} \\ 0 & 0 & 0 & 0 \end{pmatrix} + e^{ik_y} \begin{pmatrix} t_{AA} & 0 & 0 & 0 \\ 0 & t_{AA} & 0 & 0 \\ t_{AC} & 0 & t_{AA} & 0 \\ 0 & 0 & 0 & t_{AA} \end{pmatrix} + \\
&+ e^{-ik_y} \begin{pmatrix} t_{AA} & 0 & t_{AC} & 0 \\ 0 & t_{AA} & 0 & 0 \\ 0 & 0 & t_{AA} & 0 \\ 0 & 0 & 0 & t_{AA} \end{pmatrix} + e^{i(k_x+k_y)} \begin{pmatrix} 0 & 0 & 0 & 0 \\ 0 & 0 & 0 & 0 \\ 0 & 0 & 0 & 0 \\ 0 & t_{BD} & 0 & 0 \end{pmatrix} + \\
&+ e^{-i(k_x+k_y)} \begin{pmatrix} 0 & 0 & 0 & 0 \\ 0 & 0 & 0 & t_{BD} \\ 0 & 0 & 0 & 0 \\ 0 & 0 & 0 & 0 \end{pmatrix},
\end{aligned}
\tag{3.1}
$$

where ε is the on-site energy and t_{ij} is the hopping between the i and j lattice sites. We analyze four cases:

1) $t_{AB} = t_{CD} \neq t_{AC} = t_{BD}$,

2) $t_{AB} = t_{CD} \neq t_{AC} \neq t_{BD}$,

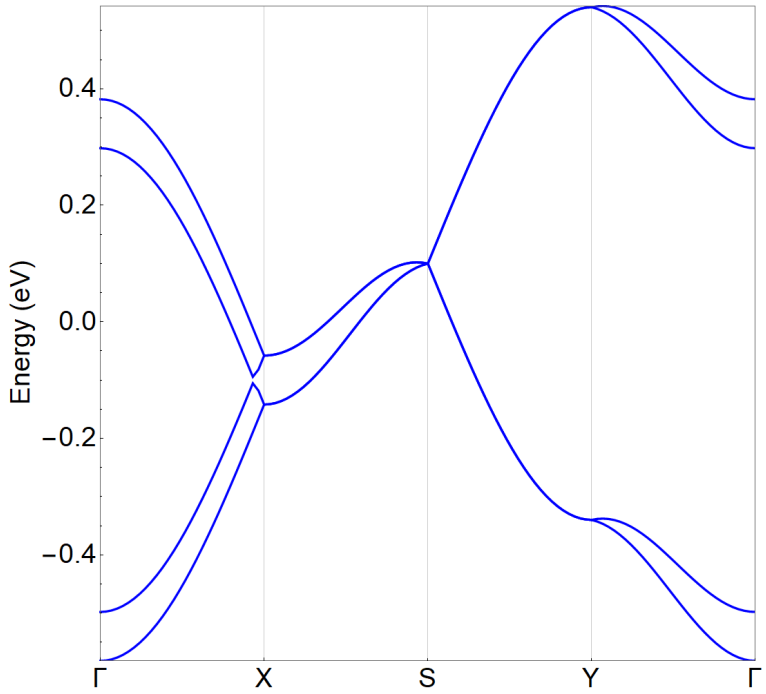

FIGURE 3.2: Band structure in the case 1) with parameters $\varepsilon = 0$, $t_{AA} = -0.050$ eV, $t_{AB} = 0.220$ eV, $t_{BD} = 0.021$ eV.

3) $t_{AB} \neq t_{CD} \neq t_{AC} = t_{BD}$,
4) $t_{AB} \neq t_{CD} \neq t_{AC} \neq t_{BD}$.

In all these cases, which are those shown in Fig. 3.1, the bands are two-fold degenerate at any $\boldsymbol{k}$ vector in the BZ, due to the inversion and the time reversal symmetries. Apart from these symmetries, the system has additional nonsymmorphic symmetries of the crystal structure, which cause the occurrence of a four-fold degeneracy along specific lines of the BZ.

1) In the case 1 of Fig. 3.1, the bands are two-fold degenerate along the ΓX and YΓ lines (where $k_y = 0$ and $k_x = 0$ respectively) of the path reported in Fig. 2.3, and four-fold degenerate along the XS and SY lines ($k_x = \pi$ and $k_y = \pi$ respectively), as we can see in Fig. 3.2. This additional degeneracy of the bands along the XS and SY lines can be explained by presence of the nonsymmorphic symmetries of the crystal structure. Along the XS line, the Hamiltonian respects the following symmetries:

$$\hat{V}_1 = s_z \otimes \tau_x = \begin{pmatrix} 0 & 1 & 0 & 0 \\ 1 & 0 & 0 & 0 \\ 0 & 0 & 0 & -1 \\ 0 & 0 & -1 & 0 \end{pmatrix}, \tag{3.2}$$

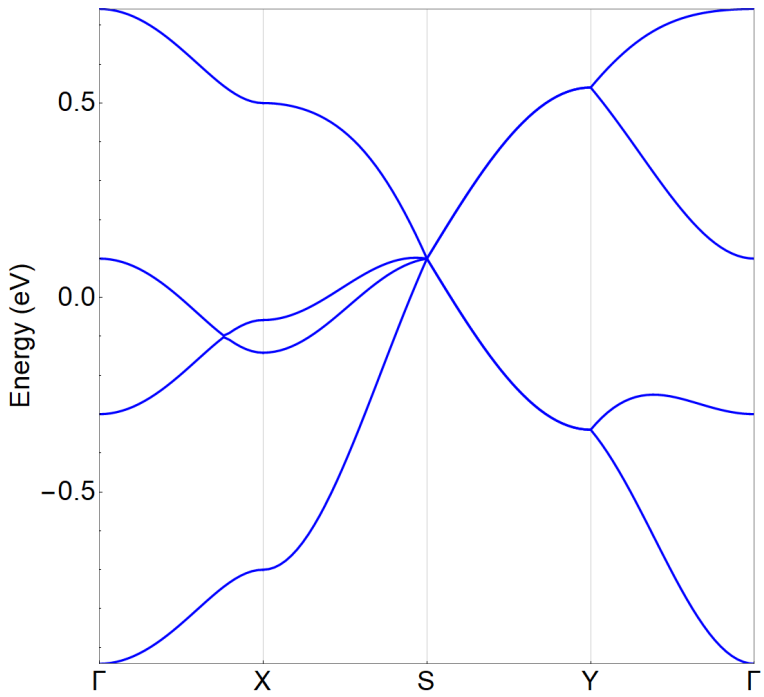

FIGURE 3.3: Band structure in the case 2) with parameters $\varepsilon = 0$, $t_{AA} = -0.050$ eV , $t_{AB} = 0.220$ eV, $t_{BD} = 0.021$ eV, $t_{AC} = 0.300$ eV.

$$\hat{W}_1(k_y) = \begin{pmatrix} 0 & 1 \\ e^{ik_y} & 0 \end{pmatrix} \otimes \tau_0 = \begin{pmatrix} 0 & 0 & 1 & 0 \\ 0 & 0 & 0 & 1 \\ e^{ik_y} & 0 & 0 & 0 \\ 0 & e^{ik_y} & 0 & 0 \end{pmatrix}. \tag{3.3}$$

These are unitary operators that commute with the Hamiltonian along this line:

$$\left[\hat{H}, \hat{V}_1\right] = 0, \quad k_x = \pi, \tag{3.4}$$

$$\left[\hat{H}, \hat{W}_1(k_y)\right] = 0, \quad k_x = \pi, \tag{3.5}$$

and anticommute each other:

$$\left\{\hat{V}_1, \hat{W}_1(k_y)\right\} = 0, \tag{3.6}$$

this ensures a band crossing along this direction.

In fact, if we consider an Hamiltonian that commutes with two unitary operators $\hat{A}$ and $\hat{B}$:

$$\left[\hat{H}, \hat{A}\right] = 0, \tag{3.7}$$

$$\left[\hat{H}, \hat{B}\right] = 0, \tag{3.8}$$

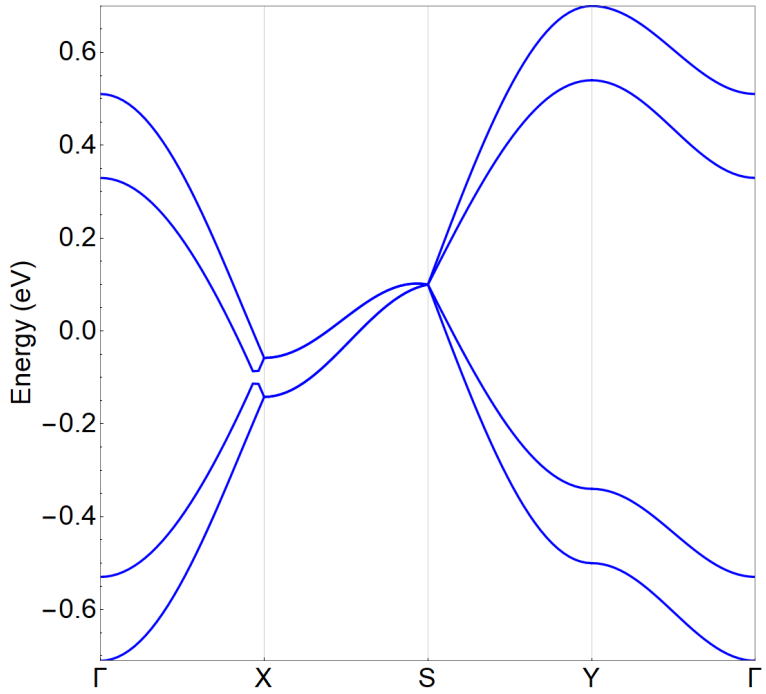

FIGURE 3.4: Band structure in the case 3) with parameters ε= 0, t_{AA}= −0.050 eV, t_{AB}= 0.220 eV, t_{BD}= 0.021 eV, t_{CD}= 0.300 eV.

in the case they anticommute each other:

$$\left\{\hat{A}, \hat{B}\right\} = 0, \tag{3.9}$$

then, if we take an eigenstate of $\hat{A}$ of eigenvalue a that is eigenstate of $\hat{H}$ of energy E:

$$\hat{A}\psi_a = a\psi_a, \tag{3.10}$$

$$\hat{H}\psi_a = E\psi_a, \tag{3.11}$$

we have that:

$$\hat{H}\hat{B}\psi_a = \hat{B}\hat{H}\psi_a = E\hat{B}\psi_a, \tag{3.12}$$

$$\hat{A}\hat{B}\psi_a = -\hat{B}\hat{A}\psi_a = -a\hat{B}\psi_a, \tag{3.13}$$

$\hat{B}\psi_a$ is an eigenstate of $\hat{H}$ of energy E, and an eigenstate of $\hat{A}$ of eigenvalue -a. ψ_a and $\hat{B}\psi_a$ are two orthogonal eigenstates of $\hat{H}$ with the same energy.
Along the SY line, the Hamiltonian respects the following symmetries:

$$\hat{V}_2 = s_z \otimes \tau_0 = \begin{pmatrix} 1 & 0 & 0 & 0 \\ 0 & 1 & 0 & 0 \\ 0 & 0 & -1 & 0 \\ 0 & 0 & 0 & -1 \end{pmatrix}, \tag{3.14}$$

$$\hat{W}_2(k_x) = \begin{pmatrix} 0 & 1 \\ e^{ik_x} & 0 \end{pmatrix} \otimes \tau_x = \begin{pmatrix} 0 & 0 & 0 & e^{ik_x} \\ 0 & 0 & e^{ik_x} & 0 \\ 0 & 1 & 0 & 0 \\ 1 & 0 & 0 & 0 \end{pmatrix}. \tag{3.15}$$

These are unitary operators that commute with the Hamiltonian along this line:

$$\left[\hat{H}, \hat{V}_2\right] = 0, \quad k_y = \pi, \tag{3.16}$$

$$\left[\hat{H}, \hat{W}_2(k_x)\right] = 0, \quad k_y = \pi, \tag{3.17}$$

and anticommute each other:

$$\left\{\hat{V}_2, \hat{W}_2(k_x)\right\} = 0. \tag{3.18}$$

This ensures a band crossing along this direction.

$\hat{V}_1$ acts by exchanging the coordinates of A and B and that of C and D within the unit cell, $\hat{V}_2$ acts only as a phase on atoms C and D ; $\hat{W}_1(k_y)$ and $\hat{W}_2(k_x)$ are instead nonsymmorphic operators involving half translation of the reciprocal lattice and a transformation on the unit cell configurations, which satisfy the following relation:

$$\hat{W}_1^2(k_y) = e^{ik_y}\mathbb{I}, \tag{3.19}$$

whose eigenvalues are $\pm e^{ik_y/2}$, and where $\mathbb{I}$ is the identity matrix [103].

2) In the case 2 of Fig. 3.1, we consider $t_{AB} = t_{CD} \neq t_{AC} \neq t_{BD}$. The additional degeneracy of the bands is broken along the XS line, but not along the SY line, as we show in Fig. 3.3. Along the XS line the degeneracy is broken because the Hamiltonian is no longer invariant upon the action of $\hat{V}_1$.

3) If we have $t_{AB} \neq t_{CD} \neq t_{AC} = t_{BD}$, like in the case 3 of Fig. 3.1, the additional degeneracy of the bands is broken along the SY line, but not along the XS line, and we show this in Fig. 3.4. Along the SY line the degeneracy is broken because the Hamiltonian is no longer invariant upon the action of $\hat{W}_2(k_x)$.

4) If we take $t_{AB} \neq t_{CD} \neq t_{AC} \neq t_{BD}$, like in the case 4 of Fig. 3.1, the degeneracy of the bands is broken both along XS and SY lines, as shown in Fig. 3.5.

The case 2) of Fig. 3.1, due to the peculiar constraints on the hoppings, is what interests us because it corresponds to a 2D simplification of the models for the systems with MnP-type crystal structure. In Sec. 3.3 we will generalize this model to the 3D case. If we look at the Eq. 3.1, the 2D model Hamiltonian in the case 2) (when $t_{CD} = t_{AB}$) can be represented in the form of a tensor product of the Pauli matrices:

$$\begin{aligned} H(k_x,k_y) =& t_1(k_y)s_0 \otimes \tau_0 + t_2(k_x)s_0 \otimes \tau_x + \\ & t_3(k_x,k_y)s_x \otimes \tau_0 + \\ & t_4(k_x,k_y)s_y \otimes \tau_0 + \\ & t_5(k_x,k_y)s_x \otimes \tau_z + \\ & t_6(k_x,k_y)s_y \otimes \tau_z + \\ & t_7(k_x)s_z \otimes \tau_y, \end{aligned} \tag{3.20}$$

where s_i and τ_i represent the Pauli matrices for $i = x, y, z$, and the unit matrices for $i = 0$. The parameters are:

$$\begin{aligned} t_1(k_y) &= \varepsilon + 2t_{AA}cos(k_y) \\ t_2(k_x) &= t_{AB}(1 + cos(k_x)) \\ t_3(k_x,k_y) &= \frac{1}{2}(t_{AC} + t_{BD}cos(k_x) + t_{AC}cos(k_y) + t_{BD}cos(k_x + k_y)) \\ t_4(k_x,k_y) &= \frac{1}{2}(t_{BD}sin(k_x) + t_{AC}sin(k_y) + t_{BD}sin(k_x + k_y)) \\ t_5(k_x,k_y) &= \frac{1}{2}(t_{AC} - t_{BD}cos(k_x) + t_{AC}cos(k_y) - t_{BD}cos(k_x + k_y)) \\ t_6(k_x,k_y) &= \frac{1}{2}(-t_{BD}sin(k_x) + t_{AC}sin(k_y) - t_{BD}sin(k_x + k_y)) \\ t_7(k_x) &= -t_{AB}sin(k_x). \end{aligned} \tag{3.21}$$

We can look now at the Fermi surfaces that can be obtained in these cases. In the case 1), when the bands are degenerate at $k_x = \pi$ and $k_y = \pi$, the pockets of the Fermi surface are forced to be connected on these lines. So we have a limited number of possibilities for the shape of the Fermi surfaces if we fix the number of Fermi points along the XS and SY lines. In Fig. 3.6 we show some possible surfaces obtained with a cut at -0.28 eV, with zero Fermi points along the XS line and two along the SY line, and in Fig. 3.7 some possible surfaces obtained with a cut at -0.03 eV, with four Fermi points along the XS line and zero along the SY line. The lines of the Fermi surface can start from one of the Fermi points at $k_x = \pi$ or $k_y = \pi$ and then end into another one or in the same passing through the BZ or extending in a limited region close to the high symmetry line. These various possibilities are shown in the panels

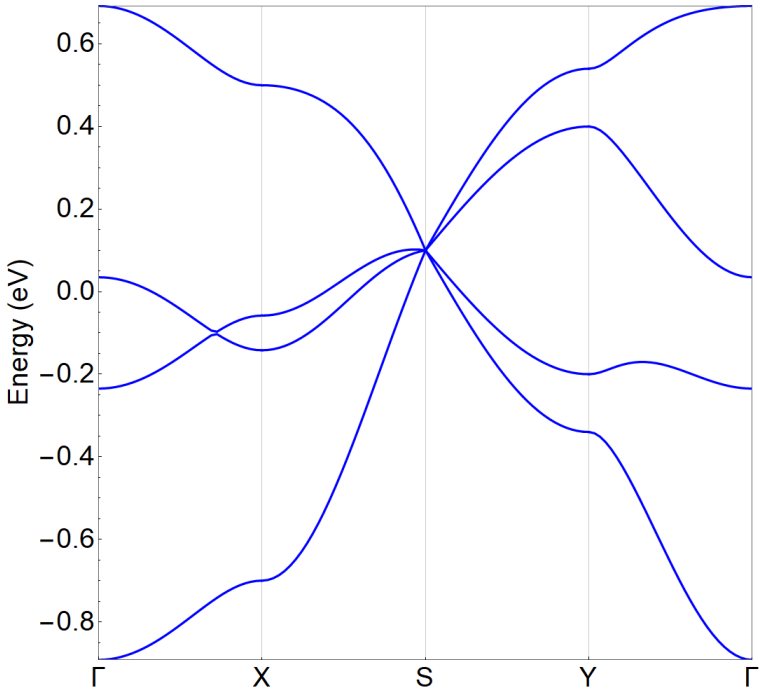

FIGURE 3.5: Band structure in the case 4) with parameters ε= 0, t_{AA}= −0.050 eV, t_{AB}=0.220 eV, t_{BD}=0.021 eV, t_{CD}=0.150 eV, t_{AC}=0.300 eV.

a), b) and c) of the Figures.

We show in Fig. 3.8 some possibilities for the Fermi surfaces in the case 3) obtained with a cut at 8.3 eV. In this case the Fermi points along the SY line are four, differently from the case 1), due to the fact that the degeneracy along this line is broken. Now the surfaces are not forced to be connected on the SY line, differently from the case 1).

In Fig. 3.9 we show some possible surfaces obtained in the case 2) with a cut at 8.55 eV.

The constraints on the Fermi surface given by the nonsymmorphic symmetries will be shown more in detail in the cases of materials like WP, CrAs and MnP in the Sec. 3.4.

3.3 Structural and electronic properties of WP and comparison with CrAs and MnP

3.3.1 DFT computational details

We have performed DFT calculations by using the VASP package. [53] The core and the valence electrons were treated within the PAW method [54] with a cutoff of 400 eV for the plane wave basis. We have used a PAW with 6 valence electrons for the W ($6s^2 5d^4$), 7 valence electrons for the Mn ($4s^1 3d^6$) and 5 valence electrons for the P ($3s^2 3p^3$). The calculations have been performed using a 12×16×10 k-point

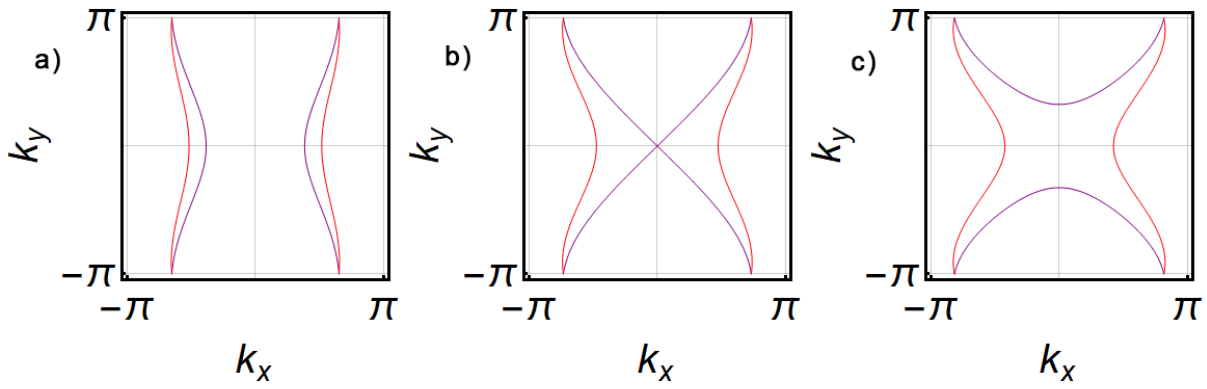

FIGURE 3.6: Surfaces obtained with a cut at − 0.28 eV in the case 1). The hopping parameters are (in eV): a) $t_{AA} = 0.026$, $t_{AB} = 0.220$,$t_{BD} = 0.015$. b) $t_{AA} = 0.051$, $t_{AB} = 0.220$,$t_{BD} = 0.029$. c) $t_{AA} = 0.078$, $t_{AB} = 0.220$,$t_{BD} = 0.045$. The different colors are the contributions of the different bands.

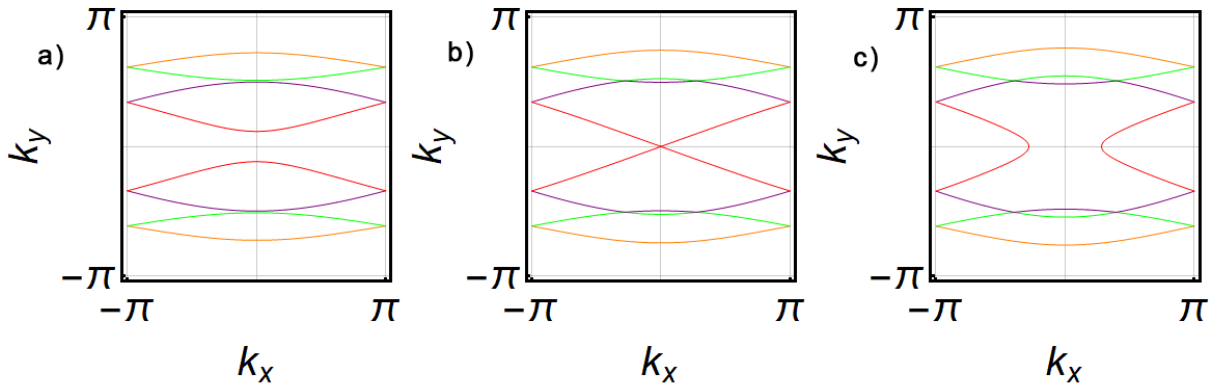

FIGURE 3.7: Surfaces obtained with a cut at − 0.03 eV in the case 1). The hopping parameters are (in eV): a) $t_{AA} = 0.779$, $t_{AB} = 0.300$,$t_{BD} = 0.450$. b) $t_{AA} = 0.674$, $t_{AB} = 0.300$,$t_{BD} = 0.389$. c) $t_{AA} = 0.606$, $t_{AB} = 0.300$,$t_{BD} = 0.35$. The different colors are the contributions of the different bands.

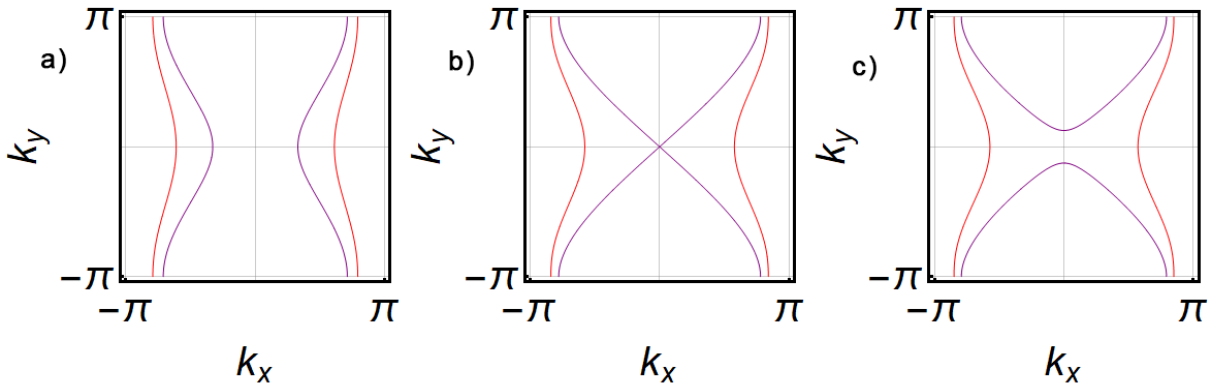

FIGURE 3.8: Surfaces obtained with a cut at − 0.28 eV in the case 3). The hopping parameters are (in eV): a) $t_{AA} = 0.043$, $t_{AB} = 0.220$, $t_{BD} = 0.025$ and $t_{CD} = 0.300$. b) $t_{AA} = 0.065$, $t_{AB} = 0.220$, $t_{BD} = 0.038$ and $t_{CD} = 0.300$. c) $t_{AA} = 0.069$, $t_{AB} = 0.220$, $t_{BD} = 0.04$ and $t_{CD} = 0.300$. The different colors are the contributions of the different bands.

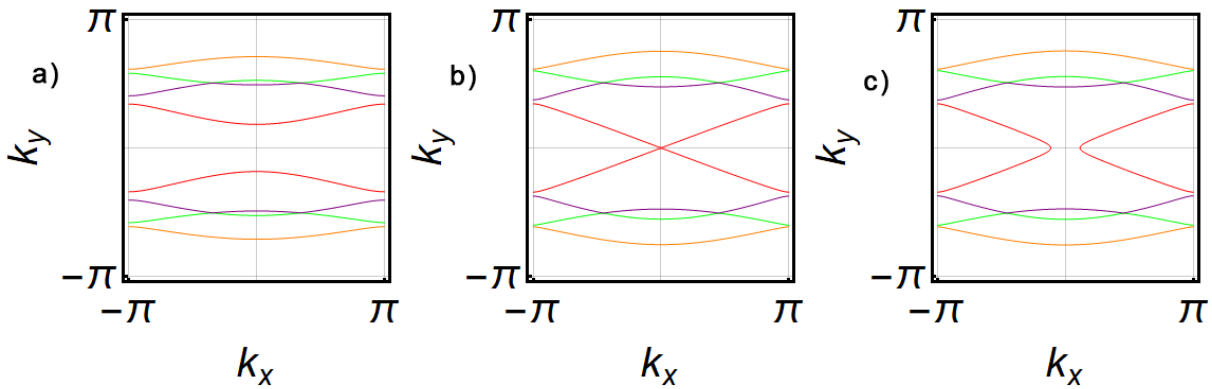

FIGURE 3.9: Surfaces obtained with a cut at − 0.03 eV in the case 2). The hopping parameters are (in eV): a) $t_{AA} = 0.779$, $t_{AB} = 0.300$, $t_{BD} = 0.45$ and $t_{AC} = 0.300$. b) $t_{AA} = 0.613$, $t_{AB} = 0.300$, $t_{BD} = 0.354$ and $t_{AC} = 0.300$. c) $t_{AA} = 0.606$, $t_{AB} = 0.300$, $t_{BD} = 0.350$ and $t_{AC} = 0.300$. The different colors are the contributions of the different bands.

Monkhorst-Pack grid [125] for the non polarized case and a 6×8×6 k-point Monkhorst-Pack grid for the case with SOC. In the first case we have a 240 k-points in the indipendent BZ, while we have 288 k-points in the case with SOC. For the treatment of exchange-correlation, the generalized gradient approximation (GGA) [126] has been used. For the CrAs, we have used the computational setup of the previous chapter.

We have optimized the internal degrees of freedom by minimizing the total energy to be less than 7×10^{-7} eV. After obtaining the Bloch wave functions $\psi_{n,\mathbf{k}}$, the Wannier functions [57, 58] have been built up using the WANNIER90 code [59] generalizing the following formula to get the Wannier functions $W_n(\mathbf{r})$:

$$W_n(\mathbf{r}) = \frac{V}{(2\pi)^3}\int d\mathbf{k}\psi_{n,\mathbf{k}}e^{-i\mathbf{k}\cdot\mathbf{r}}, \tag{3.22}$$

where V is the volume of the unit cell and n is the band index.

To extract the low energy properties of the electronic bands, we have used the Slater-Koster interpolation scheme as implemented in Wannier90. In particular, we have fitted the electronic bands, in order to get the hopping parameters and the SOC constants. This approach has been applied to determine the real space Hamiltonian matrix elements in the maximally localized Wannier function basis, and to find out the Fermi surface with a 50×50×50 k-point grid.

3.3.2 Structural properties

WP belongs to the same family of CrAs, that of transition metal pnictides with the general formula MX (M = transition metal, X = P, As, Sb). At ambient pressure it presents an orthorhombic MnP-type crystal structure (space group Pnma). We will compare the properties of WP with those of CrAs and MnP and for all these three compounds we will focus on the MnP-type phase, being the one where the superconducting phase occurs. As already said in the previous chapter for the CrAs, in these compounds the M atoms are situated in the centre of MX_6 octahedra, which are face-sharing as shown in figure 2.1.

In Table 3.1, we compare the structural properties of WP, CrAs and MnP at ambient pressure with the ideal high-symmetry crystal structure of the WP. The lattice constants of the high-symmetry structure are given by: a=$\sqrt[3]{V\sqrt{2}}$, b=$\sqrt[3]{V/2}$, c=$\sqrt[3]{V\sqrt{2}}$, where V is the volume of primitive cell of the WP. The experimental investigation on WP provided just the lattice constants, without any info about the refinement of the unit cell and the corresponding internal degrees of freedom [12]. Hence, while the internal degrees of freedom used for the DFT calculation of CrAs and MnP have been assumed from the experimental observations, for the WP we had to explicitly calculate them by means of the atomic relaxations within the DFT.
We notice that a and c of the WP are larger than those of CrAs and MnP; the b lattice constant of CrAs is the largest and it is responsible for the antiferromagnetic transition exhibited by this compound [8]. In the Table 3.1, we also report the values of the four inequivalent bonds M-X_1-M-X_4, and observe that M-X_2 and M-X_3 are

TABLE 3.1: Unit-lattice cell parameters, coordinates of the M and X atoms, bond lengths connecting M and X atoms, polyhedral volume (PV) and bond angle variance (BAV), of the transition-metal pnictides MX compared with the ideal high-symmetry structure (HSS). Space group: Pnma. Atomic positions: M: 4c (x, 1/4, z); X: 4c (x, 1/4, z).

	WP [12]	**CrAs** [32]	**MnP** [11, 127]	**HSS**
a(Å)	5.7222	5.60499	5.236	5.4627
b(Å)	3.2434	3.58827	3.181	3.8627
c(Å)	6.2110	6.13519	5.896	5.4627
V(Å^3)	115.27	123.392	98.20	115.27
x_M	0.0138*	0.0070	0.0049	0
z_M	0.1880*	0.2049	0.1965	1/4
x_X	0.1822*	0.2045	0.1878	1/4
z_X	0.5654*	0.5836	0.5686	1/2
Bond length(Å)				
M-X_1	2.5342*	2.5736	2.3938	1.9314
M-X_2	2.4967*	2.5116	2.3379	2.7314
M-X_3	2.4972*	2.5274	2.3848	2.7314
M-X_4	2.4653*	2.4511	2.2803	1.9314
PV(Å^3)	19.212*	20.565	16.367	19.212
BAV (deg.^{2})	191.49*	77.708	142.98	0

* present work

almost degenerate. Finally, we have computed the polyhedral volume (PV), namely the volume of the octahedra that can be build around the M atoms, and the bond angle variance (BAV) of these octahedra, which we define as $\sum_{i=1,6}[\frac{(\theta_i-\theta_0)^2}{n-1}]$ where θ_0 is the ideal bond angle equal to 90° for a regular octahedron. Concerning the PV, we notice that the value for WP is larger than MnP since the atomic radius of W is larger with respect to Mn. Moreover, the PV of CrAs has the largest value because of the large volume of the As. The estimated BAV values show that the WP exhibits a more distorted structure if compared to CrAs and MnP.

3.3.3 DOS and band structure

In this subsection, we present the DFT based results of the electronic properties of WP. First, we look at the DOS for three different sets of parameters, in order to extract the dominant orbital character in the different regions of the energy spectrum and to investigate the effect of the octahedral rotations on the crystal-field energy levels. The first DOS considered is that obtained with the ideal high-symmetry crystal structure as that quoted in the Table 3.1 where there are no octahedral rotations. Then, we consider the experimental volume and the ideal high-symmetry atomic positions where there is the part of the octahedral rotations due to the volume effect. Finally, we examine the experimental structure with the atomic positions calculated from the atomic relaxation procedure with full octahedral rotations.

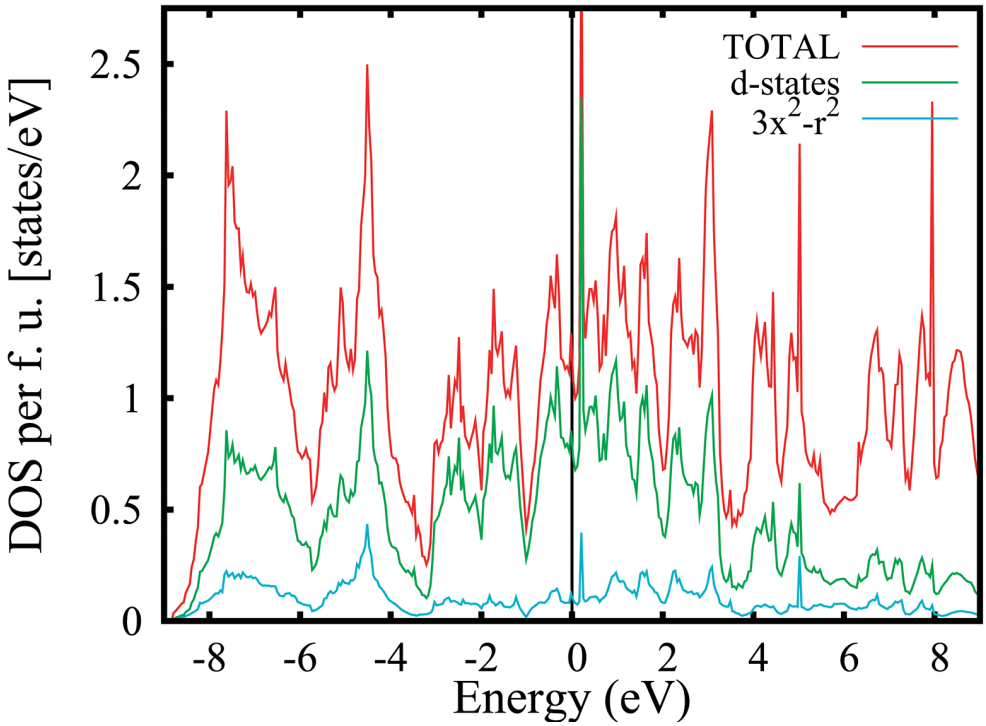

FIGURE 3.10: DOS for the hypothetical high-symmetry structure. The total DOS per formula unit is plotted as red. W states are plotted as green and the $3x^2 - r^2$ states are shown in cyan. The Fermi level is set at the zero energy.

To estimate the effect of the distortions, we follow the evolution of the $d_{3x^2-r^2}$-energy levels where x is the direction orthogonal to the face-sharing surfaces. Without octahedral distortions, these $d_{3x^2-r^2}$ orbital states are the lowest non-degenerate energy levels in the face-shared octahedral crystal field [128]. However, we show that the energy levels change in presence of the strong octahedral distortions of the WP. Therefore, the $d_{3x^2-r^2}$ states give an indication on how close we are to the undistorted case.

In the first case, the $3x^2 - r^2$ DOS presents the largest peak at about 5 eV below the Fermi level as we can see from the Fig. 3.10. In the second case, there is a mixing between different energy levels, producing two large peaks approximately located at -4 eV and +2 eV, as it can be observed by inspection of Fig. 3.11. In the third case, corresponding to the fully distorted structure, the Fig. 3.12 shows that the peak of the $3x^2 - r^2$ DOS is set at about 3 eV above the Fermi level. Thus, moving from the ideal structure to the fully distorted structure, the $3x^2 - r^2$ energy level peaks move from occupied to unoccupied configurations. One of the reasons why the energy levels change so drastically as a function of the structural properties in this family is the weakness of the crystal field. Indeed, in strongly ionic systems, like in transition metal oxides, the transition metal atom is surrounded by atoms with filled p-shells. In these compounds, the transition metal atom is surrounded by atoms with partially filled p-shells, producing a weaker crystal field. Moreover, the strongly distorted structure,

favored by the weak crystal field, produces a mixing of the orbital character of the d-bands making impossible to identify a subset of d-orbital close to the Fermi level. As we can see from Fig. 3.12, referring to the character of the bands, we infer that the bands close to the Fermi level are primarily due to the W degrees of freedom, so they are more flat with respect to the bands that are located 4 eV above and below the Fermi level, and this leads to peaks in the DOS. The latter bands may assigned to P states, and are more delocalized with respect to the W ones.

The character of the DOS from -8.5 eV to -6 eV is predominantly P-3p, while from -6 eV to 4 eV the W-5d states dominate, and finally, above 4 eV there is a mixing between P-3p, P-4s and W-6s states. For completeness, in Fig. 3.13 we show the P-3p states together with the total DOS by using the experimental lattice constants and the internal positions calculated within the DFT.

We remark that, since the W bands are due to 5d orbitals, the bandwidth is much wider than that of CrAs and MnP, so that we may suppose that the WP is the least correlated system between the three transition metal pnictides investigated. As for CrAs [20], it is hopeless to entirely decouple the W-5d states close to the Fermi level from the P-3p states in an accurate way, because of the strong hybridization between them, as we show in Appendix A, where we also comment on the oxidation state of CrAs, WP, and MnP. Nevertheless, an accurate effective model for a reduced number

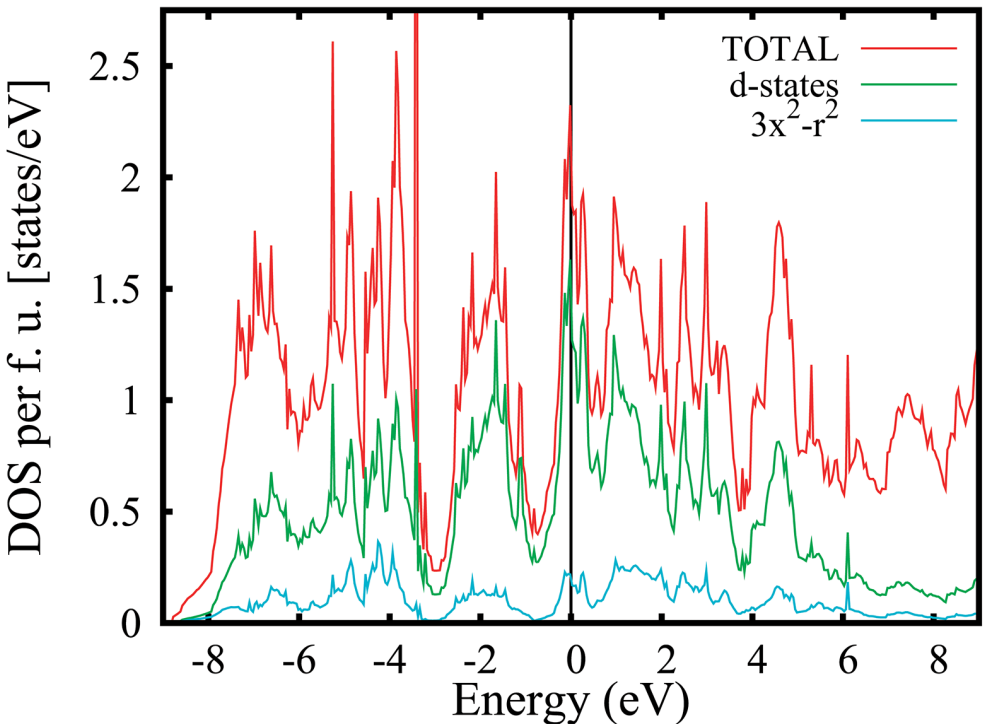

FIGURE 3.11: DOS of the WP obtained considering the experimental lattice parameters and the high-symmetry atomic positions. The total DOS per formula unit is plotted as red. W states are plotted as green and the $3x^2 - r^2$ states are shown in cyan. The Fermi level is set at the zero energy.

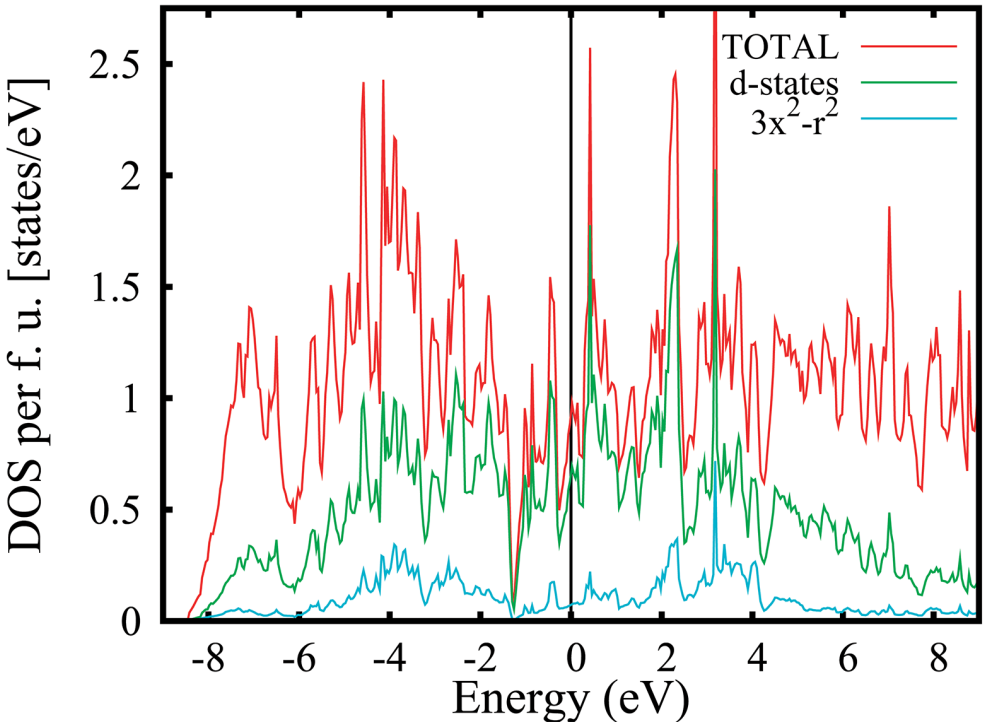

FIGURE 3.12: DOS of the WP by using the experimental lattice constants and the internal positions calculated in this work. The total DOS per formula unit is plotted as red. W states are plotted as green and the $3x^2 - r^2$ states are shown in cyan. The Fermi level is set at the zero energy.

of d-bands can be obtained also in the present case of strong hybridization.

After the analysis of the DOS, we investigate the band structure of WP and its similarities to those of CrAs and MnP.

We show in Figs. 3.14- 3.15 the band spectrum derived from first principle calculations, in the cases where the SOC in included or not in the calculations. The bandwidth is around 16 eV and, as already pointed out for the DOS, there are flat bands near the Fermi level, due to the W degrees of freedom, while the wider bands located far from the Fermi level are mainly due to the phosphorus atoms. As for CrAs, the band structure without SOC presents not only inversion $\hat{P}$ and time-reversal $\hat{T}$ symmetries, but additional nonsymmorphic symmetries. The Kramers degeneracy, protected by the $\hat{P}\hat{T}$ antiunitary operator, is still present under the action of SOC. The additional degeneracies can be two-fold in case of one nonsymmorphic symmetry or four-fold in case of two nonsymmorphic symmetries and are active only along some high-symmetry lines because the corresponding operators are momentum-dependent, as we have already shown in Sec. 3.1. In particular, along the SR line the band structure carries an overall eight-fold degeneracy due to the presence of two nonsymmorphic symmetries. Such multifold degeneracy is also expected to effectively reduce the probability for the bands to cross the Fermi level and thus they can induce some

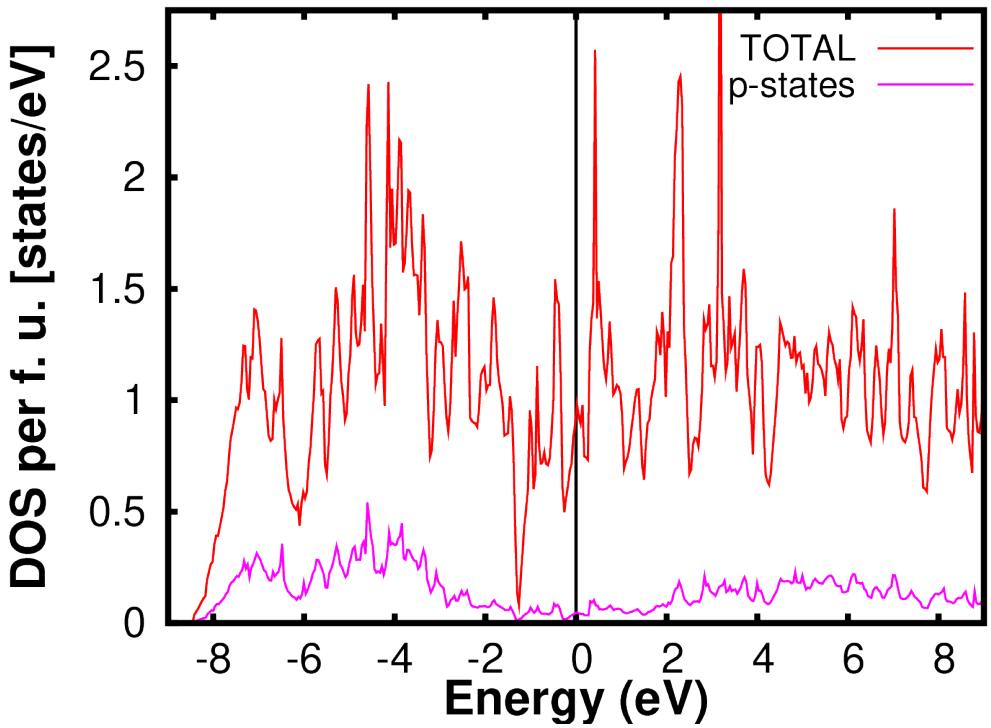

FIGURE 3.13: DOS of the WP by using the experimental lattice constants and the internal positions calculated in this work. The total DOS per formula unit is plotted as red and the P-3p states are plotted as magenta. The Fermi level is set at the zero energy.

consequences on the dimensionality of the Fermi surface, as we will consider in more details in the next sections. For completeness, in Figs. 3.16 and 3.17, we show with different colors the different degeneracies of the bands along the orthorhombic BZ without and with the application of the SOC interaction.

The interplay between the SOC interaction and the inter-orbital degrees of freedom allows for a selective removal along some lines of the BZ of the band degeneracy ascribed to the crystal symmetries. Specifically, the SOC partially removes the degeneracy of the bands along the XS, TZ, YT and SR high-symmetry lines, bringing them from four-fold to two-fold degeneracy along the first three and from eight-fold to two-fold degeneracy along the last one. Instead, at the point R and S, the SOC partially removes the degeneracy bringing it from eight- to fourfold. The splitting due to the SOC along the SR line is relatively small and it does not change the dimensionality of the Fermi surface. We would like to point out that the SOC constants λ estimated from the real space Hamiltonian for the W and P atoms are λ_W=228 meV for the 5d-orbitals of the W atoms and λ_P=55 meV for the 3p-orbitals of the P atoms, respectively. As we have already seen in CrAs, also for WP the SOC related to the d orbitals affects principally the bands close to the Fermi level, because these bands have principally a d character. We have to underline that the SOC splitting is larger in WP compound than in CrAs and MnP systems, therefore the selective removal of the band degeneracy is more visible in this case, even if it is present in all these three

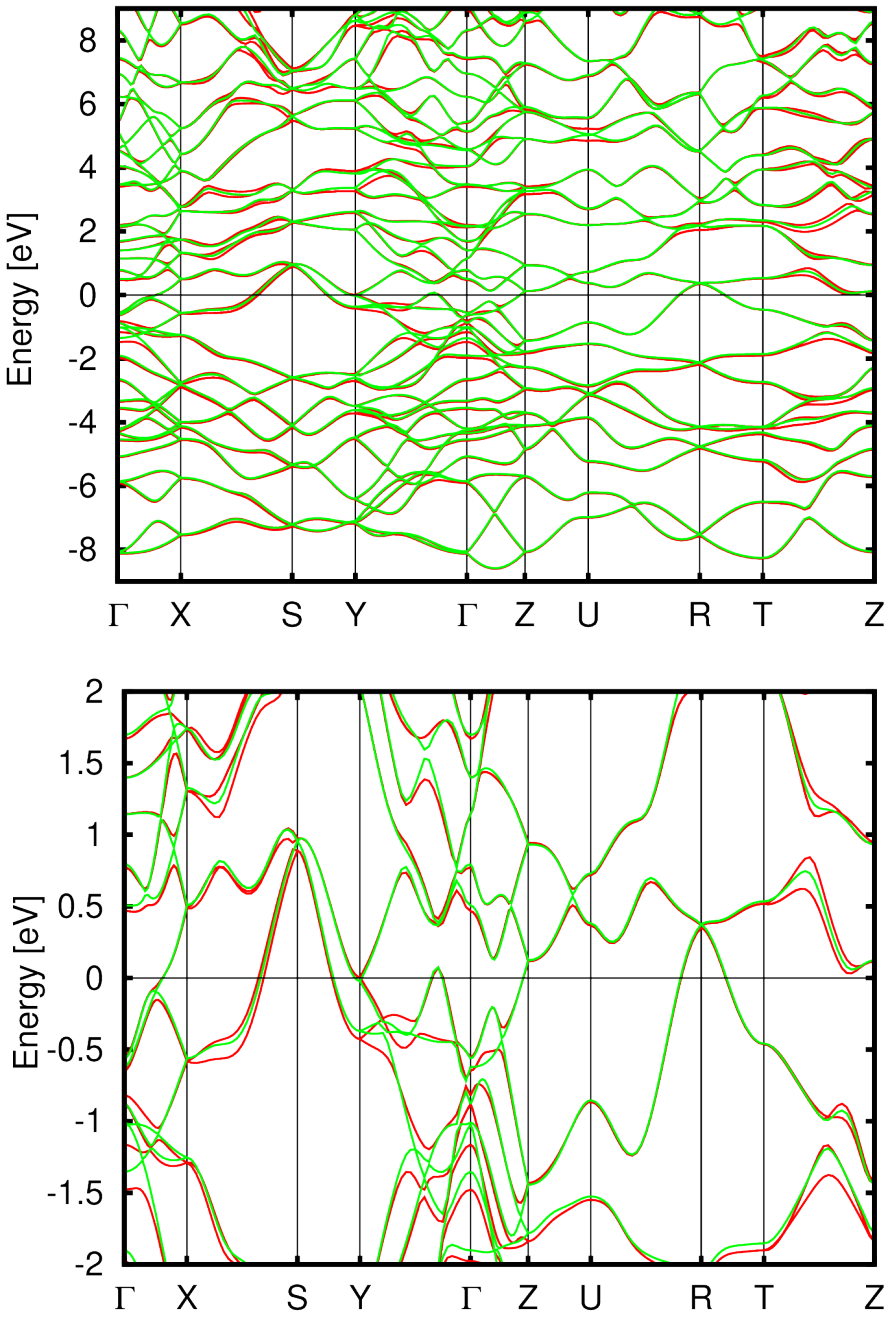

FIGURE 3.14: Band structure of the WP along the high-symmetry path of the orthorhombic BZ without (green lines) and with SOC (red lines). We plot in the energy range from -9 eV to +9 eV (top panel) and from -2 eV to +2 eV (bottom panel). The Fermi level is set at the zero energy.

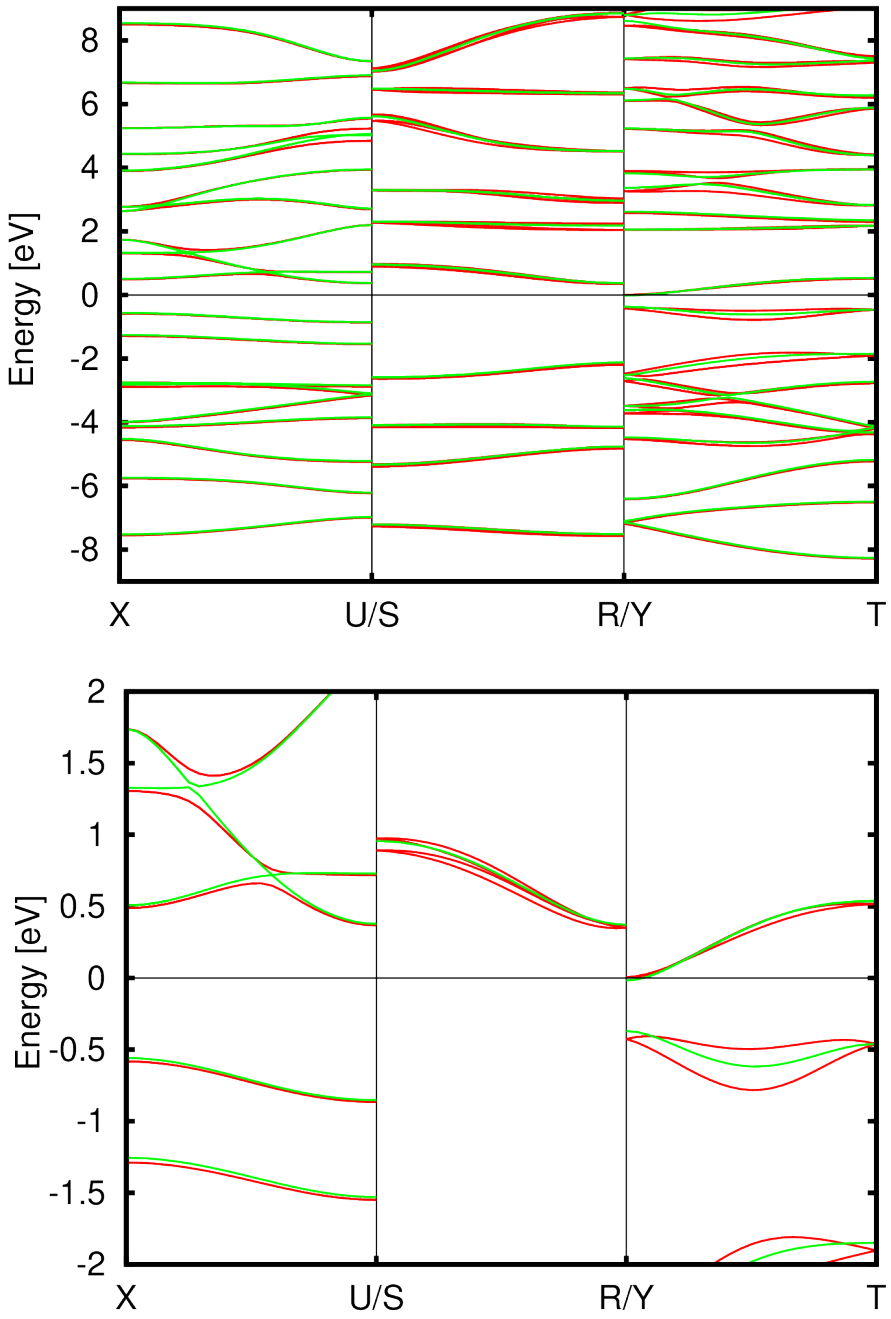

FIGURE 3.15: Band structure of the WP along the remaining high-symmetry lines of the orthorhombic BZ without (green lines) and with SOC (red lines). We plot in the energy range from -9 eV to +9 eV (top panel) and from -2 eV to +2 eV (bottom panel). The Fermi level is set at the zero energy.

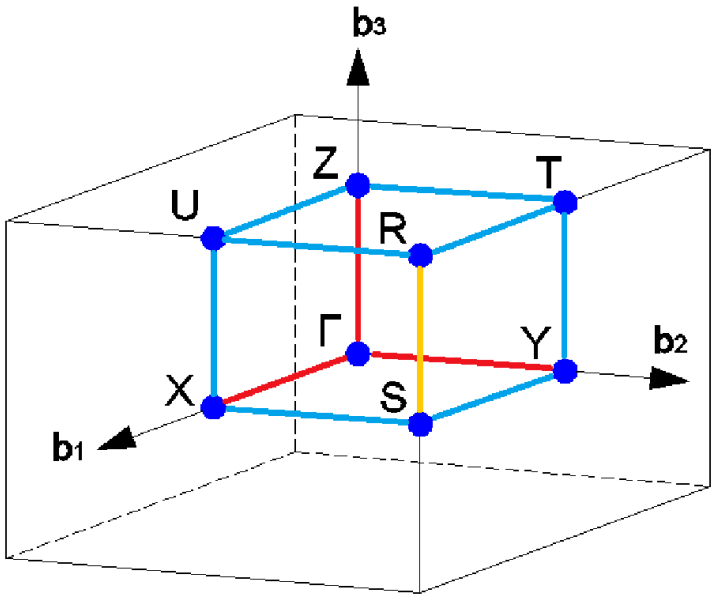

FIGURE 3.16: High-symmetry path in the orthorombic BZ with the different colors of the lines that indicate the different degeneracies of the bands in the case of absence of SOC. With red we indicate a 2-fold degeneracy, with light blue a 4-fold degeneracy and with orange a 8-fold degeneracy.

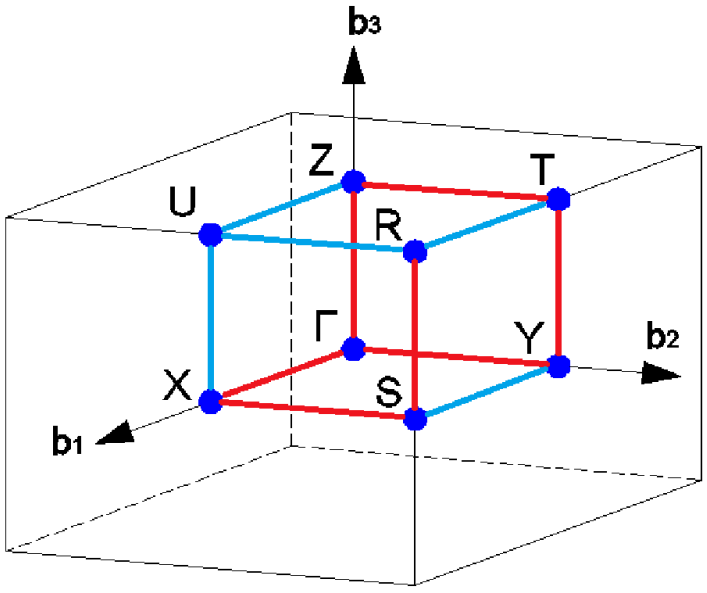

FIGURE 3.17: High-symmetry path in the orthorombic BZ with the different colors of the lines that indicate the different degeneracies of the bands in the case of presence of SOC. With red we indicate a 2-fold degeneracy and with light blue a 4-fold degeneracy.

compounds.

Due to the eight-fold degeneracy and the presence of the two nonsymmorphic symmetries, each minimal model should contain at least four bands, which are equivalent to two bands per formula unit. As a consequence, the system will be always metallic if the time reversal symmetry protection is valid and the sum of p and d electrons per formula unit is odd, like in WP and CrAs.

Because of the symmetries of the system, we will have semi-Dirac-like energy-momentum dispersions near the points X, Y and Z of the BZ. In particular, the semi-Dirac point at Y has been proposed to produce the linear magnetoresistence in CrAs and CrP [26, 129]. The band structure in Figs. 3.14- 3.15 shows a semi-Dirac point at 0.02 eV below the Fermi level suggesting that linear dependent magnetoresistance could be also found in the WP compound. The results for the band spectrum and DOS of WP share robust qualitative features with those of the CrAs and MnP compounds.

3.4 3D model Hamiltonian and eight-fold degeneracy along the SR line

In this section we demonstrate the eight-fold degeneracy along the SR line due to the presence of a pair of nonsymmorphic symmetries [28]. To do this, we extend our 2D model Hamiltonian described in Sec. 3.1 to the 3D case and we show an example in case we consider two orbitals. The elements have been set according to the outcome of the DFT calculations. In particular, we restrict to the representative subspace of two d-orbitals (i.e. d_{xy} and d_{yz}) and consider only non-vanishing projected W-W hopping amplitudes. When the spin degeneracy is considered, one can reduce the analysis by considering separately each spin channel, thus remaining with two 8×8 blocks in the Hamiltonian matrix. We denote by $t^{lmn}_{\alpha_i,\alpha_j}$ the hopping amplitudes between the sites α_i and α_j (where $i, j = A, B, C, D$ as labelled in Fig. 3.18) along the direction $\mathrm{l}\mathbf{x} + \mathrm{m}\mathbf{y} + \mathrm{n}\mathbf{z}$.

The Hamiltonian for each spin-channel is then written as follows:

$$H(k_x, k_y, k_z) = \begin{pmatrix} H_{\alpha\alpha}(k_x, k_y, k_z) & H_{\alpha\beta}(k_x) \\ H_{\beta\alpha}(k_x) & H_{\beta\beta}(k_x, k_y, k_z) \end{pmatrix}, \tag{3.23}$$

where α and β label the d_{xy} and the d_{yz} orbital, and $H_{\beta\alpha}$ is the conjugate transpose of $H_{\alpha\beta}$. The diagonal term of the matrix $H_{\alpha\alpha}$ is expressed as:

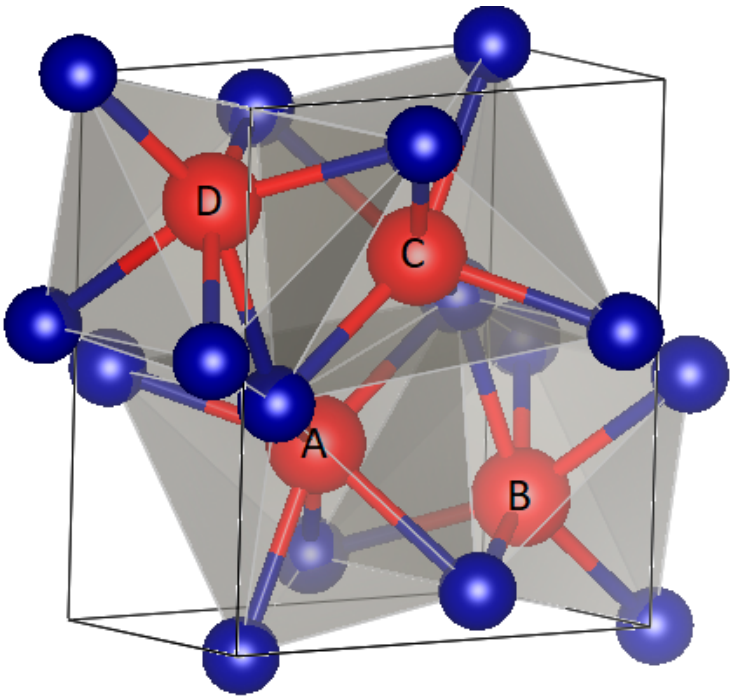

FIGURE 3.18: Crystal structure of the WP in the Pnma symmetry after atomic relaxation. W and P atoms are shown as red and blue balls, respectively. The face-shared WP_6 octahedra are shown in light gray. The W atoms are labelled as A,B,C,D.

$$\begin{aligned} H_{\alpha\alpha}(k_x,k_y,k_z) =& t_1(k_x,k_y,k_z)\sigma_0\otimes\gamma_0 + t_2(k_x)\sigma_0\otimes\gamma_x + \\ &+ t_3(k_x,k_y,k_z)\sigma_x\otimes\gamma_0 + \\ &+ t_4(k_x,k_y,k_z)\sigma_y\otimes\gamma_0 + \\ &+ t_5(k_x,k_y,k_z)\sigma_x\otimes\gamma_z + \\ &+ t_6(k_x,k_y,k_z)\sigma_y\otimes\gamma_z + \\ &+ t_7(k_x)\sigma_z\otimes\gamma_y, \end{aligned} \tag{3.24}$$

where σ_i and γ_i represent the Pauli matrices for $i = x, y, z$, and the unit matrices for $i = 0$. An analogous expression to Eq. (3.24) defines also $H_{\beta\beta}$.
The hopping parameters have the following expressions:

$$\begin{aligned} t_1(k_x,k_y,k_z) =& \varepsilon_0 + 2\sum_{n=1,2,3} t^{n00}_{AA\alpha\alpha}\cos(nk_x) + \\ &+ 2\sum_{n=1,2,3} t^{0n0}_{AA\alpha\alpha}\cos(nk_y) + \\ &+ 2\sum_{n=1,2,3} t^{00n}_{AA\alpha\alpha}\cos(nk_z) \\ t_2(k_x) =& t^{100}_{AB\alpha\alpha}(1+cos(k_x)) \\ t_3(k_x,k_y,k_z) =& \frac{1}{2}(t^{001}_{AC\alpha\alpha} + \\ &+ t^{00\bar{1}}_{AC\alpha\alpha}cos(k_x) + t^{001}_{AC\alpha\alpha}cos(k_y) + \\ &+ t^{00\bar{1}}_{AC\alpha\alpha}cos(k_x+k_y) + t^{00\bar{1}}_{AC\alpha\alpha}cos(k_z) + \\ &+ t^{00\bar{1}}_{AC\alpha\alpha}cos(k_y+k_z) + t^{001}_{AC\alpha\alpha}cos(k_x+k_z) + \\ &+ t^{001}_{AC\alpha\alpha}cos(k_x+k_y+k_z)) \\ t_4(k_x,k_y,k_z) =& \frac{1}{2}(t^{00\bar{1}}_{AC\alpha\alpha}sin(k_x) + \\ &+ t^{001}_{AC\alpha\alpha}sin(k_y) + t^{00\bar{1}}_{AC\alpha\alpha}sin(k_x+k_y) + \\ &+ t^{00\bar{1}}_{AC\alpha\alpha}sin(k_z) + t^{00\bar{1}}_{AC\alpha\alpha}sin(k_y+k_z) + \\ &+ t^{001}_{AC\alpha\alpha}sin(k_x+k_z) + \\ &+ t^{001}_{AC\alpha\alpha}sin(k_x+k_y+k_z)) \end{aligned} \tag{3.25}$$

$$
\begin{aligned}
t_5(k_x,k_y,k_z) &= \frac{1}{2}(t^{001}_{AC\alpha\alpha} - t^{00\bar{1}}_{AC\alpha\alpha}cos(k_x)+ \\
&+ t^{001}_{AC\alpha\alpha}cos(k_y) - t^{00\bar{1}}_{AC\alpha\alpha}cos(k_x+k_y)+ \\
&+ t^{00\bar{1}}_{AC\alpha\alpha}cos(k_z) + t^{00\bar{1}}_{AC\alpha\alpha}cos(k_y+k_z)+ \\
&- t^{001}_{AC\alpha\alpha}cos(k_x+k_z)+ \\
&- t^{001}_{AC\alpha\alpha}cos(k_x+k_y+k_z)) \\
t_6(k_x,k_y,k_z) &= \frac{1}{2}(-t^{00\bar{1}}_{AC\alpha\alpha}sin(k_x)+ \\
&+ t^{001}_{AC\alpha\alpha}sin(k_y) - t^{00\bar{1}}_{AC\alpha\alpha}sin(k_x+k_y)+ \\
&+ t^{00\bar{1}}_{AC\alpha\alpha}sin(k_z) + t^{00\bar{1}}_{AC\alpha\alpha}sin(k_y+k_z)+ \\
&- t^{001}_{AC\alpha\alpha}sin(k_x+k_z)+ \\
&- t^{001}_{AC\alpha\alpha}sin(k_x+k_y+k_z)) \\
t_7(k_x) &= -t^{100}_{AB\alpha\alpha}sin(k_x).
\end{aligned}
\tag{3.26}
$$

The off-diagonal term $H_{\alpha\beta}$ is written as:

$$
\begin{aligned}
H_{\alpha\beta}(k_x) = &\begin{pmatrix} t^{000}_{AA\alpha\beta} & t^{100}_{AB\alpha\beta} & 0 & 0 \\ t^{100}_{AB\beta\alpha} & t^{000}_{AA\alpha\beta} & 0 & 0 \\ 0 & 0 & t^{000}_{AA\alpha\beta} & t^{100}_{AB\alpha\beta} \\ 0 & 0 & t^{100}_{AB\beta\alpha} & t^{000}_{AA\alpha\beta} \end{pmatrix} + \\
&+ e^{ik_x}\begin{pmatrix} 0 & t^{100}_{AB\beta\alpha} & 0 & 0 \\ 0 & 0 & 0 & 0 \\ 0 & 0 & 0 & 0 \\ 0 & 0 & t^{100}_{AB\alpha\beta} & 0 \end{pmatrix} + \\
&+ e^{-ik_x}\begin{pmatrix} 0 & 0 & 0 & 0 \\ t^{100}_{AB\alpha\beta} & 0 & 0 & 0 \\ 0 & 0 & 0 & t^{100}_{AB\beta\alpha} \\ 0 & 0 & 0 & 0 \end{pmatrix},
\end{aligned}
\tag{3.27}
$$

where $t^{100}_{AB\alpha\beta} \neq t^{100}_{AB\beta\alpha}$. Note that all the hoppings are written in units of a, b and c. The values of the hopping parameters of the model that fits the bands around the S and R points are reported in Appendix B.

We will now focus on the tight-binding Hamiltonian along the SR line $H(k_z)$, where we keep fixed $(k_x,k_y)=(\pi,\pi)$. We notice that, along that high symmetry line, the $t_2(k_x)$,...,$t_7(k_x)$ hybridization terms in the intra-orbital subspace do vanish. This circumstance reduces $H(k_z)$ in a non block-diagonal form, where only the intra-orbital sectors $H_{\alpha\alpha}(k_z)$ and $H_{\beta\beta}(k_z)$ are diagonal.

When we take both spin-channels, we can then consider the two unitary operators:

$$\hat{Q} = s_0 \otimes \tau_0 \otimes \sigma_y \otimes \gamma_y, \tag{3.28}$$

$$\hat{U}(k_z) = \begin{pmatrix} 0 & 1 \\ e^{ik_z} & 0 \end{pmatrix} \otimes \tau_0 \otimes \sigma_z \otimes \gamma_y, \tag{3.29}$$

where s_i, τ_i, σ_i and γ_i represent the Pauli matrices for $i = x, y, z$, and the unit matrices for $i = 0$. s_i act in the subspace of spins, τ_i in the subspace of orbitals, σ_i and γ_i in the subspace set by the atomic states in the unit cell. The operators $\hat{Q}$ and $\hat{U}(k_z)$ commute with the Hamiltonian $H(k_z)$ along the SR path:

$$\left[\hat{H}, \hat{Q}\right] = 0, \quad at\ (k_x, k_y) = (\pi, \pi), \tag{3.30}$$

$$\left[\hat{H}, \hat{U}(k_z)\right] = 0, \quad at\ (k_x, k_y) = (\pi, \pi). \tag{3.31}$$

Moreover, they anticommute with each other:

$$\left\{\hat{Q}, \hat{U}(k_z)\right\} = 0. \tag{3.32}$$

In particular, $\hat{Q}$ acts by exchanging the coordinates of A and D atoms within the unit cell; $\hat{U}(k_z)$ is instead a nonsymmorphic operator, similar to those of Sec. 3.1, involving half translation of the reciprocal lattice and a transformation on the unit cell configurations, which satisfies the following relation:

$$\hat{U}^2(k_z) = e^{ik_z}\mathbb{I}\ , \tag{3.33}$$

whose eigenvalues are $\pm e^{ik_z/2}$, and where $\mathbb{I}$ is the identity matrix [103].
Along the SR line, $H(k_z)$ also commutes with other two unitary operators:

$$\hat{V} = s_0 \otimes \tau_0 \otimes \sigma_z \otimes \gamma_y, \tag{3.34}$$

$$\hat{W}(k_z) = \begin{pmatrix} 0 & 1 \\ e^{ik_z} & 0 \end{pmatrix} \otimes \tau_0 \otimes \sigma_y \otimes \gamma_y, \tag{3.35}$$

$$\left[\hat{H}, \hat{V}\right] = 0, \quad at\ (k_x, k_y) = (\pi, \pi), \tag{3.36}$$

$$\left[\hat{H}, \hat{W}(k_z)\right] = 0, \quad \text{at}\ (k_x, k_y) = (\pi, \pi). \tag{3.37}$$

Moreover, $\hat{V}$ and $\hat{W}(k_z)$ anticommute with each other:

$$\left\{\hat{V}, \hat{W}(k_z)\right\} = 0. \tag{3.38}$$

We notice that $\hat{V}$ acts by exchanging the coordinates of B and C atoms within the unit cell, while $\hat{W}(k_z)$, apart from acting on the intra-unit cell orbital degrees of freedom, is a nonsymmorphic operator involving half translation of the reciprocal lattice. Furthermore, we have that the operators $\hat{Q}$, $\hat{V}, \hat{W}(k_z)$ and $\hat{U}(k_z)$ fulfill the following algebra:

$$\left\{\hat{Q}, \hat{V}\right\} = 0, \tag{3.39}$$

$$\left[\hat{Q}, \hat{W}(k_z)\right] = 0, \tag{3.40}$$

$$\left[\hat{U}(k_z), \hat{V}\right] = 0, \tag{3.41}$$

$$\left[\hat{U}(k_z), \hat{W}(k_z)\right] = 0. \tag{3.42}$$

Since $\hat{U}$ and $\hat{V}$ commute between each other and with the Hamiltonian, it is possible to choose a common eigenstate ψ_{uv}, labeled by the corresponding u and v eigenvalues of $\hat{U}$ and $\hat{V}$, associated to the same energy $E(k_z)$:

$$\hat{U}\psi_{uv} = u\psi_{uv} \qquad \hat{V}\psi_{uv} = v\psi_{uv}, \tag{3.43}$$

$$H(k_z)\psi_{uv} = E(k_z)\psi_{uv}. \tag{3.44}$$

Then, by using the commutation and anticommutation relations between the above operators (see the Eqs. (3.32), (3.38) and (3.39) – (3.42)), one can have:

$$\hat{U}(\hat{Q}\psi_{uv}) = -u(\hat{Q}\psi_{uv}) \qquad \hat{V}(\hat{Q}\psi_{uv}) = -v(\hat{Q}\psi_{uv}), \tag{3.45}$$

$$\hat{U}(\hat{W}\psi_{uv}) = u(\hat{W}\psi_{uv}) \qquad \hat{V}(\hat{W}\psi_{uv}) = -v(\hat{W}\psi_{uv}), \tag{3.46}$$

$$\hat{U}(\hat{Q}\hat{W}\psi_{uv}) = -u(\hat{Q}\hat{W}\psi_{uv}) \qquad \hat{V}(\hat{Q}\hat{W}\psi_{uv}) = v(\hat{Q}\hat{W}\psi_{uv}), \tag{3.47}$$

Eqs. (3.43) – (3.47) show that it is possible to construct a subspace associated to the same energy eigenvalue, spanned by the four orthogonal basis states: ψ_{uv}, $\hat{Q}\psi_{uv}$, $\hat{W}\psi_{uv}$ and $\hat{Q}\hat{W}\psi_{uv}$. The dimensionality of this subspace equals the four-fold degeneracy which is obtained along the SR line, for each of the spin channels. We finally point out that the inclusion of the SOC interaction in the tight-binding Hamiltonian partially removes the degeneracy, bringing it from eight-fold to two-fold. This is because the total Hamiltonian is no longer invariant upon $\hat{Q}$, $\hat{U}$, $\hat{V}$ and $\hat{W}$. On the contrary, the SOC interaction does not remove the time-inversion degeneracy associated to the combination of inversion and time reversal symmetry. The results of the presented analysis allow us to conclude that the four-fold degeneracy for each spin channel is due to the existence of two couples of anticommuting symmetry operators, two of

them being nonsymmorphic, which satisfy the algebra given by Eqs. (3.32), (3.38) and (3.39) – (3.42).

3.5 Effect of the nonsymmorphic symmetries on the Fermi surface

In this section we investigate the evolution of the Fermi surfaces (FS) as a function of the electron filling. In the first subsection, we will discuss some general consideration while in the second we will report the DFT results. In the second subsection, we will start by considering the case of vanishing SOC, while at the end of this section the effects of the SOC term will be discussed. The FS of the WP are deduced at ambient pressure whereas those of the CrAs and MnP are derived at the critical pressures where the magnetism is suppressed and the superconductivity comes in. In the case of CrAs, we use the results from the literature [32]. Instead, for the MnP the experimentally measured pressure amplitude that suppresses the magnetism is 7 GPa [65], while from our *ab-initio* calculations we find that the magnetization goes to zero with a metamagnetic transition when the volume is uniformly reduced by 5.8 %. Therefore, we apply the theoretically predicted volume, which is reduced of 5.8 % with respect to the ambient pressure, for proceeding further about the determination of the Fermi surface. For completeness, we mention that the metamagnetic transition can be accounted by considering the peaks of the DOS close to Fermi level [65, 66].

3.5.1 General considerations

We first consider the case of Fermi points along the SR line. If the bands along the SR direction cross the Fermi level, we have eight Fermi points $(\pm\pi, \pm\pi, \pm k_F)$ due to the inversion and mirror symmetry in this class of compounds. The Fermi points $(\pm\pi, \pm\pi, \pm k_F)$ are eight-fold degenerate, four-fold because of the intracell orbital degrees of freedom, which are connected by two nonsymmorphic symmetries, and two-fold because of the inversion-time reversal symmetry. Since the electronic structure along the SR line does not have a semimetallic behavior, due to the time-inversion degeneracy in the whole BZ, in any plane that includes the SR line there are four Fermi lines emerging from the Fermi points which can evolve in various ways by ending into the other Fermi points. Many combinations are possible, however, an even number of Fermi points should be connected because of inversion and mirror symmetries.

At this stage we would like to discuss the connection between the degeneracy of electronic states along the high symmetry lines and the dimensionality and topology of the multiple Fermi surface sheets. Let us start with a basic observation. The fact of having an eightfold degenerate Fermi point along the SR line implies that there will be four separate Fermi lines (i.e. two times four due to the twofold degeneracy arising from the time-inversion symmetry in the whole BZ) around it in any given plane

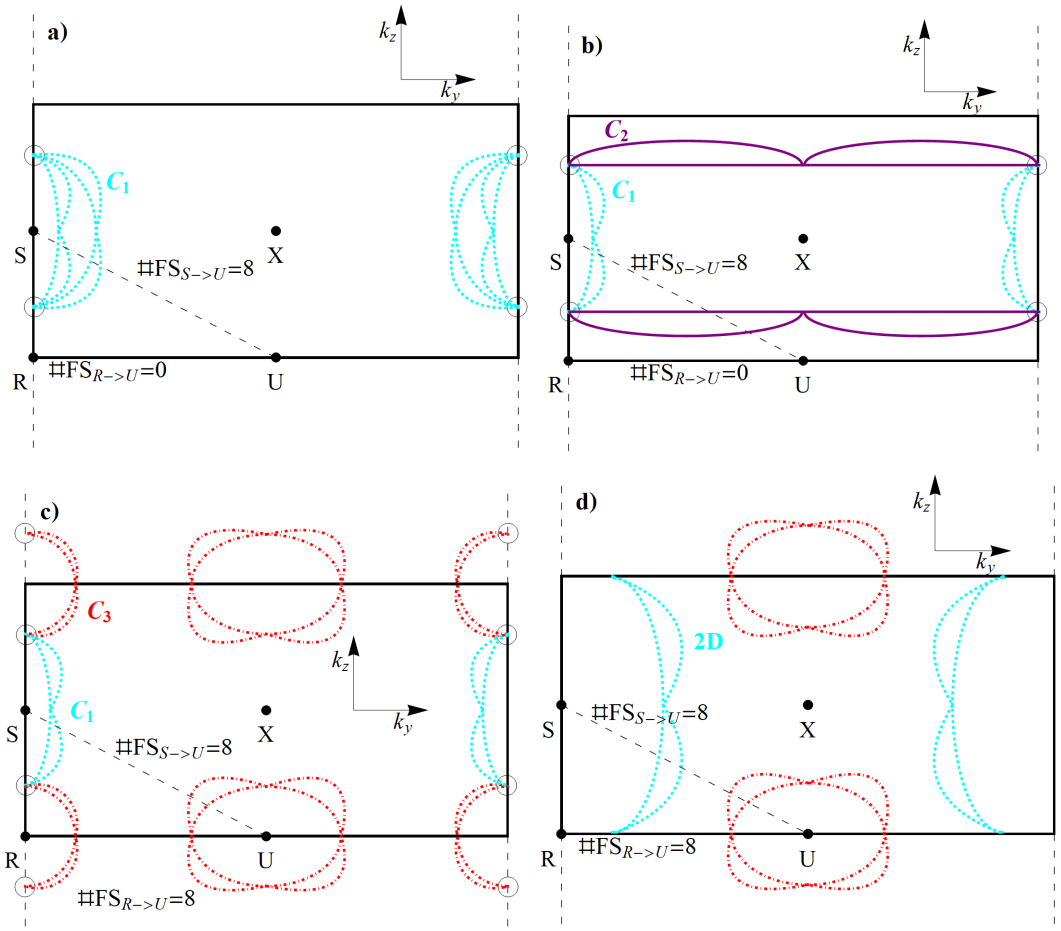

FIGURE 3.19: (k_y,k_z) plane side view of the connections obtained in the MnP compound. a) Schematic Fermi surface for $n_2 \ll n < n_1$. b) Schematic Fermi surface for $n_2 < n \ll n_1$. c) Schematic Fermi surface for $n_3 < n < n_2$. d) Schematic Fermi surface for $n < n_3$. The Fermi points at $(\pm\pi, \pm\pi, \pm k_F)$ are represented by the open circles in the a), b) and c) panels. The critical fillings n_1, n_2 and n_3 are defined in Fig. 3.21.

containing the Fermi point itself. These lines can start from one of the Fermi points along the SR line and then end into another one or in the same passing through the BZ or extending in a limited region close to the high symmetry line. Since different lines can have inequivalent connecting properties, the resulting topological aspect of the closed Fermi loops is highly nontrivial and its evolution is tied to the multifold character crossing points within the Brilluoin zone.

As example of this class of compounds, we examine the case of the MnP that shows many different Fermi surface topologies close to the nominal filling. We show (k_y,k_z) side view of the FS sketch since it is the only one interesting in this case. In order to be more illustrative, we have deviced different topological configurations of the connecting lines between the Fermi points on the SR high symmetry line (see Figs. 3.19 (a)-(c)). A distinct state is then represented by an evolved configuration with respect to the previous ones but without Fermi points along the SR line. This is represented in Fig. 3.19 (d) where the connecting lines are between Fermi points

belonging to the RU cut. In Fig. 3.19 (a) we have depicted a situation where all the lines connect the two Fermi points without intersecting the zone boundaries. This type of connecting line is indicated as C_1. Another possibility is that some of the lines connect the same Fermi point by crossing the whole BZ and are labeled as C_2 and others are C_1-like (see Fig. 3.19(b)). Finally, we report a relevant physical case for the MX studied compounds, corresponding to the presence of two Fermi pockets centered around the S and R points of the BZ (see Fig. 3.19 (c)), respectively.

To move further in the discussion, we observe that the cases in Figs. 3.19(a) and (b) can be connected if two of the C_1 lines get closer to the X point and cross with the mirror symmetric ones. On the other hand, the configuration in Fig. 3.19 (b) can evolve into that one in Fig. 3.19 (c) if the C_2 lines cross the RU cut. These modifications of the Fermi lines are not directly linked with the multifold degeneracy along the SR line. On the contrary, we would like to focus on the electronic transition between the case with two Fermi pockets around S and R (Fig. 3.19(c)) and that one with two open Fermi lines depicted in Fig. 3.19(d). Indeed, if the change of filling is moving the Fermi points from S to R, then the Fermi pockets associated to the lines C_3 shrink and disappear while, due to the fourfold degeneracy along the RU cut, the C_1 lines keep staying connected with the Fermi points now evolving along the RU cut. Such electronic transition is constrained by the fact that there is an eightfold degeneracy along the SR line while it is only fourfold along the RU cut. We recall that the degeneracy of the RU line is dictated by the presence of only one nonsymmorphic symmetry transformation instead of two as for the SR cut. The electronic changeover exhibits a simultaneous modification of the Fermi surface dimensionality and topology. Indeed, the C_3 Fermi pockets disappear (red dots) while the C_1 pockets become open creating the 2D FSs.

Another remark, concerning a soft connection of the multifold degeneracy and the topology of the Fermi surface, is that when the nonsymmorphic symmetries are absent, the hybridization between the bands create the bonding-antibonding splitting producing a large bandwidth, so that the bands have higher probability to cross the Fermi level because they have a significant overlap with the other bands in the BZ. On the other hand, in the presence of the two nonsymmorphic symmetries, the electronic states collapse onto a unique band and the smaller bandwidth reduces the probability for the bands to cross the Fermi level. This is shown in Fig. 3.20.

Now, let us move to statements more specific about the MX class of compounds. The band structure that is 8-fold degenerate at R by symmetry splits in two fourfold degenerate branches along RU as shown in Fig. 3.21. When the band structure can be described with an effective single orbital, the Hamiltonian (3.23) is suffice to describe the low energy electronic structure. At R we have one eigenvalue eightfold degenerate: $E(R) = t_1(\pi, \pi, \pi)$. We can follow the evolution of the eigenvalues from R to U:

$$E_{\pm}(\pi, \pi - \epsilon, \pi) = t_1 \pm \sqrt{t_3^2 + t_4^2}. \tag{3.48}$$

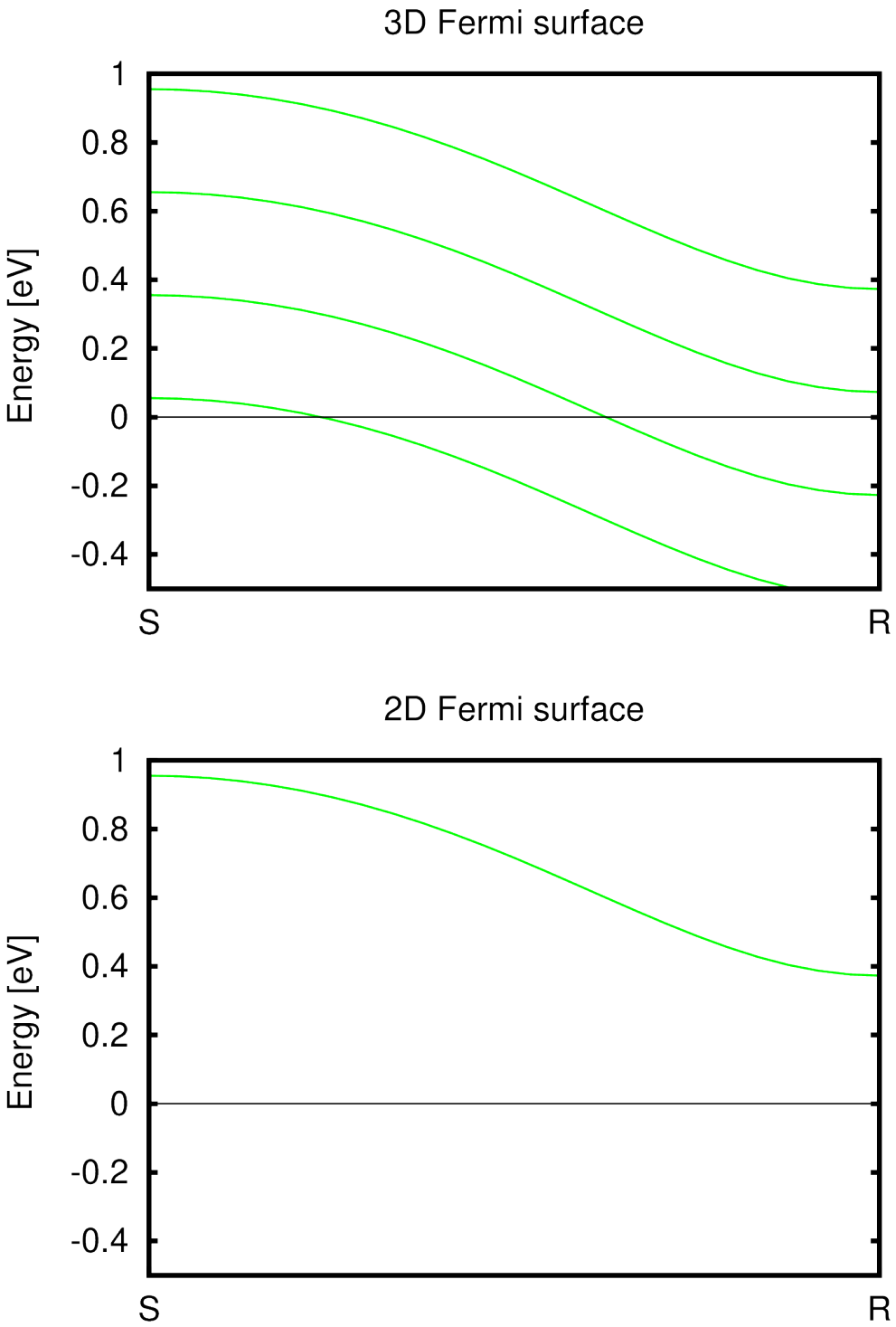

FIGURE 3.20: Schematic example of the band structure along the SR line without (left panel) and with nonsymmorphic symmetries (right panel).

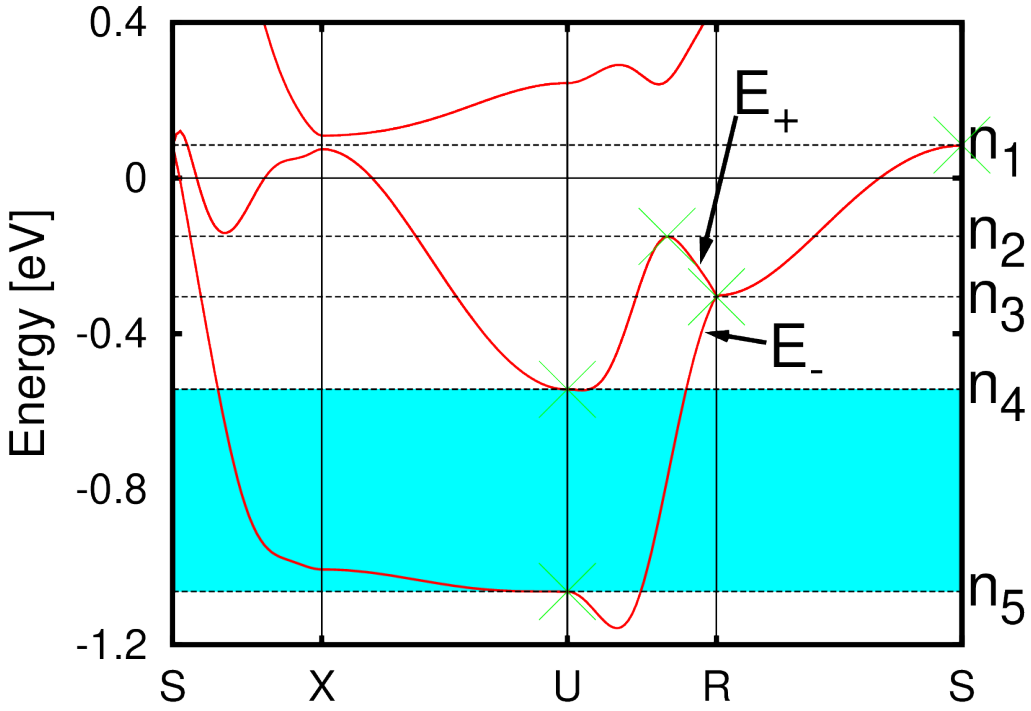

FIGURE 3.21: Band structure of MnP along the S-X-U-R-S high-symmetry lines of the orthorhombic BZ without SOC. We plot in the energy range from -1.2 eV to +0.4 eV. The topological region is shown in cyan. The Fermi level at the nominal filling is set at the zero energy.

The series expansion at first order in ϵ gives:
$t_1(\pi, \pi-\epsilon, \pi) \simeq t_1(\pi,\pi,\pi)$, $t_3(\pi, \pi-\epsilon, \pi) \simeq 0$ and $t_4(\pi, \pi-\epsilon, \pi) \simeq (t^{001}_{AC\alpha\alpha} - t^{00\bar{1}}_{AC\alpha\alpha})\epsilon$, from which we can conclude that the two eigenvalues

$$E_{\pm}(\pi, \pi-\epsilon, \pi) = t_1(\pi,\pi,\pi) \pm |(t^{001}_{AC\alpha\alpha} - t^{00\bar{1}}_{AC\alpha\alpha})|\epsilon \tag{3.49}$$

have an opposite and Dirac-like linear behaviour in ϵ as shown in Fig. 3.21.

When the branch along SR is monotonic, the RU branch in the same energy range of the SR branch generates the four C_3 FSs while the RU branch with opposite slope generates four open FS. If the branch along SR is weakly dispersive, the four open FSs are mostly 2D. In summary, if the SR branch is monotonic, weakly dispersive and can be described by a single orbital as likely in this class of compounds, these systems show four 2D FSs for a certain filling.

3.5.2 DFT results

At this stage it is useful to follow the band structure of the MnP along the path S-X-U-R-S (see Fig. 3.21) and investigate the evolution of the Fermi surfaces as function of the filling of the system n within DFT. The nominal filling for the MnP is $n = 10$ per formula unit, while the numerical values for the critical fillings, associated with

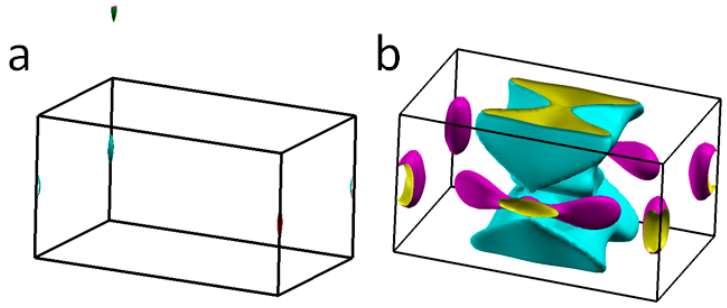

FIGURE 3.22: Fermi surface of MnP in the first BZ without SOC with filling $n_2 \ll n < n_1$. In panel a) we show two Fermi surfaces emerging from the Fermi points along the RS line, while in panel b) all the other Fermi surfaces. For a better visualization we plot one FS in the BZ and another in the reciprocal unit cell.

the presence of Fermi points along the SR cut are n_1=10.1 and n_3=9.3 per formula unit. The critical filling n_2 is related to the maximum of the band structure along the RU line. The critical fillings n_4=8.9 and n_5=8.2 are linked to the energy eigenvalues at the U point. These critical fillings define regions where we can observe different Fermi surfaces topologies.

When n is slightly larger than n_1, we have some Fermi pockets close to the S point but we do not have Fermi points along the RS line. When $n=n_1$ we have an eight-fold Fermi point at S. When $n_2 \ll n < n_1$ we have four connections of the kind C_1 as schematically shown in Fig. 3.19a). Two connections from the real band structure are shown in Fig. 3.22a) and two are shown in Fig. 3.22b). When $n_2 < n \ll n_1$ we have two connections of the kind C_1 in Fig. 3.23a) and two connection of the kind C_2 in Fig. 3.23b) while the simplified scheme is shown in Fig. 3.19b). When $n_3 < n < n_2$ we have two connections of the kind C_1 in Figs. 3.24a) and two connections of the kind C_3 in Fig. 3.24b), the schematic FS is shown in Fig. 3.19c). Below n_3, the C_1 FSs evolve in 2D FSs. Between, n_4 and n_5 the system can sustain topological superconductivity. In summary, two connections are always of the kind C_1, while the other two evolve from C_1 to C_2 and finally to C_3.
When $n=n_3$ the Fermi points reach the R point. Reducing n and considering that the Fermi surfaces of the kind C_1 cannot disappear, the Fermi points can only move along k_y forming the 2D Fermi surfaces. This implies that there will be open Fermi surfaces almost parallel to k_z. Finally, when $n < n_3$ the two Fermi pockets of the kind C_1 evolve in two 2D-Fermi surfaces, while the two Fermi pockets of the kind C_3 disappear. We thus obtain the 2D FS, as we show in Fig. 3.25a) and 3.25b).

We now proceed with the explicit comparison of the Fermi surfaces (FS) of the normal phase of the CrAs, MnP and WP compounds. We point out that those materials are characterized by different fillings, which fall into the distinct regimes above considered. The number of pnictide-p and metal-d bands is 16 per formula unit. For CrAs and WP there are 9 electrons per formula unit, while in the case of MnP we have 10 electrons per formula unit. In the case of CrAs and WP, the bands

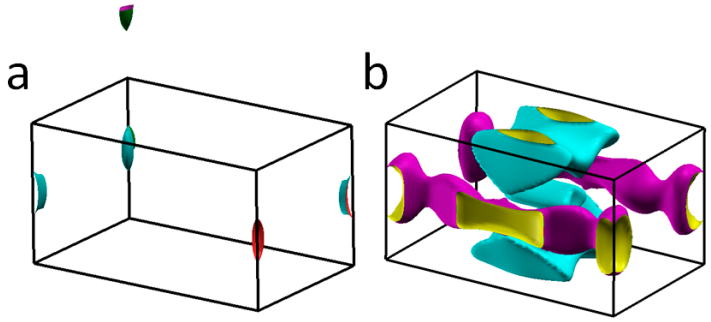

FIGURE 3.23: Fermi surface of MnP in the first BZ without SOC with filling $n_2 < n \ll n_1$. In panel a) we show two Fermi surfaces emerging from the Fermi points along the RS line, while in panel b) all the other Fermi surfaces. For a better visualization we plot one FS in the BZ and another in the reciprocal unit cell.

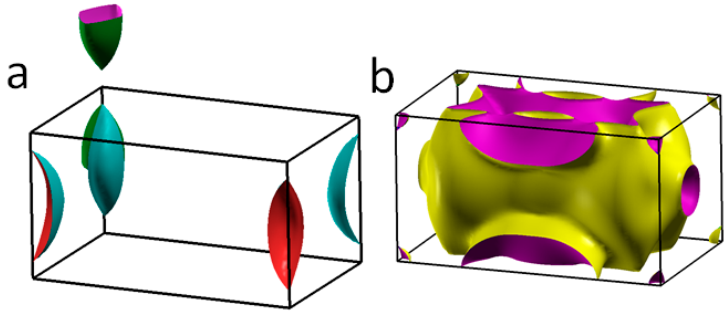

FIGURE 3.24: Fermi surface of MnP in the first BZ without SOC with filling $n_3 < n < n_2$. In panel a) we show two Fermi surfaces emerging from the Fermi points along the RS line, while in panel b) all the other Fermi surfaces. For a better visualization we plot one FS in the BZ and another in the reciprocal unit cell.

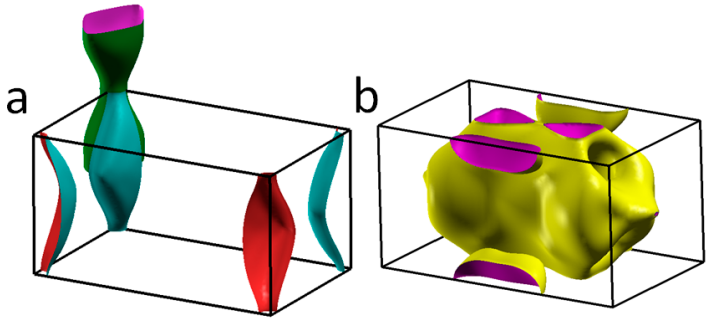

FIGURE 3.25: Fermi surface of MnP in the first BZ without SOC with filling $n_4 < n < n_3$. In panel a) we show two Fermi surfaces emerging from the Fermi points along the RS line, while in panel b) all the other Fermi surfaces. For a better visualization we plot one FS in the BZ and another in the reciprocal unit cell.

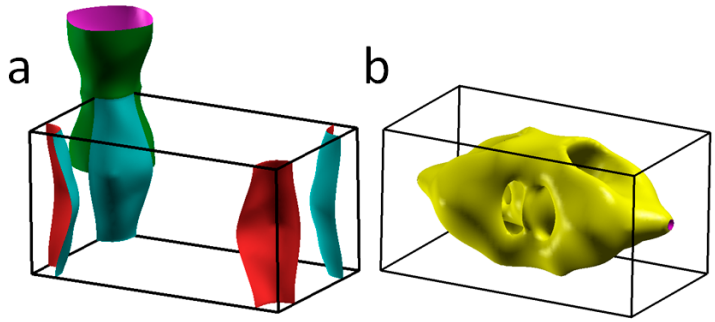

FIGURE 3.26: Fermi surface of WP at ambient pressure in the first BZ without SOC. In panel a) we show the 2D sheets, while in panel b) the three-dimensional surface around the Γ point. Since the two 2D FS are concentric, for a better visualization we plot one FS in the BZ and another in the reciprocal unit cell.

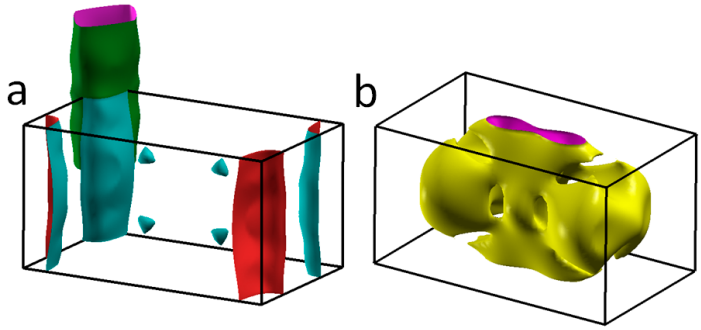

FIGURE 3.27: Fermi surface of CrAs at P=0.94 GPa in the first BZ without SOC. In panel a) we show the 2D sheets, while in panel b) the three-dimensional surface around the Γ point. Since the two 2D FS are concentric, for a better visualization we plot one FS in the BZ and another in the reciprocal unit cell.

along the SR line do not cross the Fermi level forming two-dimensional Fermi surface sheets centered around the SR line at $(k_x,k_y)=(\pi,\pi)$ and propagating along the k_z direction.

Let us discuss the 2D and 3D features of the FS of the WP plotted in Fig. 3.26a) and 3.26b). The FS displays a three-dimensional surface around the Γ point and two holelike 2D hourglass shaped sheets centred around the SR high-symmetry line, namely at $(k_x,k_y)=(\pi,\pi)$, and in the ab plane. We have to point out that the bands along the SR line are eight-fold degenerate, but when we move along the XS and the SY they splits in two four-fold bands. One of this four-fold bands crosses the Fermi level, as we can see from the bands along the XS and SY lines plotted in Fig. 3.14.

This produces the two 2D surfaces that are doubly degenerate due to the inversion-time reversal symmetry and are constrained by the crystal symmetry to be connected along the lines where the degeneracy is four-fold. We emphasise that in this class of compounds a single nonsymmorphic symmetry is not enough to create a Fermi surface with reduced dimensionality, but we need two nonsymmorphic symmetries

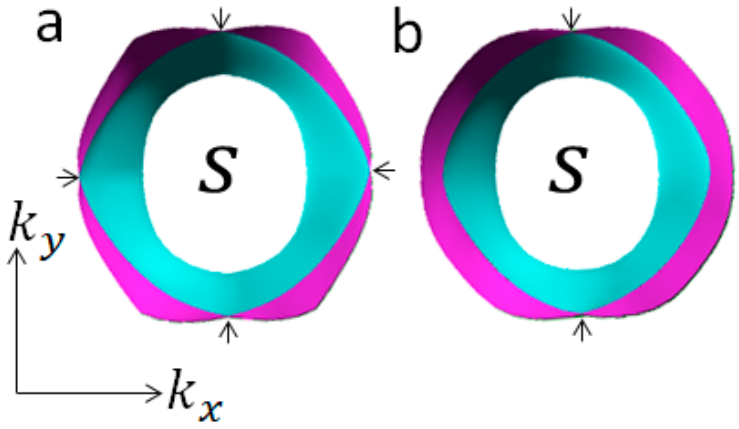

FIGURE 3.28: Top view of the 2D Fermi surface of WP centred at S point. In panel a) we report the result without SOC while in panel b) the result under the action of SOC. The arrows indicate the points of the Fermi surface four-fold degenerate, where the surfaces are forced by the crystal symmetry to be connected.

as above claimed. Since the two nonsymmorphic symmetries are present also in the non-magnetic phase of CrAs and MnP, it is likely to find two 2D Fermi surface sheets propagating along the k_z direction and centred around the SR line. Indeed, from Fig. 3.27a) and 3.27b), we see that also the CrAs shows a three-dimensional surface around the Γ point and two 2D FS. Even in this case, there are two holelike 2D surfaces in the *ab* plane centred around the SR line, but the FS are more cylindrical than those found in the WP. However, in the magnetic phase, the 2D surfaces around the SR line disappear but other 2D FS appear along other high-symmetry lines of the BZ where one a single nonsymmorphic symmetry takes place.

Finally, we investigate the effect of the SOC on the Fermi surfaces of the WP as representative case of this class. Though the SOC is too small to change the dimensionality of the Fermi surface, it produces selective splittings in the points where the FS is degenerate. We report the two 2D Fermi surfaces of the WP without SOC in Fig. 3.28a) and including SOC in Fig. 3.28b). The time-inversion degeneracy is always present. Without SOC, the two FS are constrained by the nonsymmorphic symmetry to be connected in the four points intersecting the SX and SY lines resulting in a four-fold degeneracy. When the SOC acts, we observe a selective removal of the degeneracy. In particular, the FS are still forced to be connected on the SY line while the SOC splits them along the SX line.

3.6 Discussion

Concerning the superconducting phases in MX compounds, various considerations are in order.

The first observation refers to the presence of nonsymmorphic symmetries associated with the glide planes and screw axes within the Pnma crystal structure of the targeted compounds. These symmetries can lead to different predictions concerning the

nature of the superconducting state and the emergence of non-trivial topological superconductivity. Indeed, focusing on the case of a glide plane symmetry represented by $g = \{m|\boldsymbol{\tau}\}$ with m being a mirror operator and $\boldsymbol{\tau}$ a non-primitive translation operator along a direction in the mirror plane, we observe that, independently of the electronic structure at the Fermi level, there are two basic guiding principles for establishing whether one would end up into a topological nonsymmorphic crystalline superconductor. First, one needs to evaluate whether the superconducting order parameter preserves (even case) or spontaneously breaks (odd case) the glide plane symmetry. Second, one has to assess the relationship of the glide parities between any given electronic state close to the Fermi level and its particle-hole partner that enters into the pairing [70]. Indeed, the particle-hole symmetry can either preserves the glide parity or mixes the parities and such behavior is always opposite for the momentum high symmetry lines in the glide symmetric plane at $\mathbf{k}\cdot\boldsymbol{\tau} = 0$ and $\mathbf{k}\cdot\boldsymbol{\tau} = \pi/2$. This symmetry aspect allows to have a topological invariant only along those one-dimensional cuts and not a global one in the two-dimensional glide invariant plane. As a consequence, depending on the glide parity of the superconducting order parameter, there will be Majorana modes or gap closing topologically protected that occur in correspondence with the projected lines in the momentum space at $\mathbf{k}\cdot\boldsymbol{\tau} = 0$ or $\mathbf{k}\cdot\boldsymbol{\tau} = \pi/2$. One can argue that indipendently of the glide symmetry of the superconducting order parameter, for the high symmetry lines in the glide symmetric plane there will always be emerging topological features that can manifest at the edge of the superconductor [70].

A more specific prediction for the possibility of achieving a topological nonsymmorphic crystalline superconductor can be deduced by considering the topology of the Fermi surface obtained within our *ab-initio* calculations. In this case, benefiting of the construction of the topological invariants performed in Ref. [27], it is possible to link the $\mathbb{Z}_4$ (glide odd pairing) and $\mathbb{Z}_2$ (glide even pairing) topological invariants for time-reversal symmetric odd-parity superconductors to the number of Fermi surfaces intersecting two distinct connecting paths in the BZ. Our results, in this context, are particularly useful because the knowledge of the Fermi surface allows to give specific expectations on the possibility to achieve non-trivial topological superconducting phases with glide protected surface states. Taking into account the explicit expressions of the $\mathbb{Z}_4$ and $\mathbb{Z}_2$ topological invariants, one needs to evaluate the number of Fermi sheets ($\#FS$) that are encountered along the $R \to U$ and $S \to U$ cuts, including the twofold degeneracy due to time and inversion symmetries. In particular, we recall that $\theta_4^{(a)}(\pi) = \#FS_{R\to U}/2 (\mathrm{mod}\, 4)$ and $\theta_4^{(n)}(\pi) = \#FS_{S\to U}/2 (\mathrm{mod}\, 4)$ [27]. With these elements we can summarize the resulting odd parity superconducting phases for the MnP and WP as a function of the filling n for the two glide planes indicated as a-glide and n-glide [27].

The results indicate that for the nominal filling all the candidates odd parity pairing states for the WP compound are nontrivial topological crystalline nonsymmorphic

TABLE 3.2: We consider the number of Fermi sheets intersecting specific cuts in the BZ and topological invariants for the MnP at different filling n and WP at the nominal electron concentration. In the Table we report the number of intersecting Fermi surface along the high symmetry lines ($\#FS_{R\to U}$ and $\#FS_{S\to U}$) and the amplitude of the $\mathbb{Z}_4$ topologial invariant [27] corresponding to the a-glide ($\theta_4^{(a)}(\pi)$) and the n-glide symmetry ($\theta_4^{(n)}(\pi)$), respectively. Informations about the glide even superconducting phases can be directly deduced by observing that the $\mathbb{Z}_2$ topological invariants are half of the $\mathbb{Z}_4$ ones[27].

	$\#FS_{R\to U}$	$\theta_4^{(a)}(\pi)$	$\#FS_{S\to U}$	$\theta_4^{(n)}(\pi)$	2D FS
MnP with n$> n_1$	0	0	0	0	NO
MnP with n$_2 < n < n_1$	0	0	8	0	NO
MnP with n$_3 < n < n_2$	8	0	8	0	NO
MnP with n$_4 < n < n_3$	8	0	8	0	YES
MnP with n$_5 < n < n_4$	4	2	4	2	YES
WP with n=9	4	2	4	2	YES

superconductors. As a consequence of this type of topological character and of the bulk-boundary correspondence, one expects to observe surface states protected by the glide appears on the surfaces $(2k, 2p+1, 0)$ or $(0, 2k+1, 2p+1)$ (k and p being integers) and with in-gap states having a Möbius type electronic structure [27]. On the other hand, the MnP compound can be topological only upon doping, because for the nominal filling $n = 10$ the eight Fermi surfaces emerging around the S point lead to a zero topological invariant (see the second line of the Table 3.2). Here, we find a direct connection of the multifold degeneracy along the SR line and the potential topological nature of the superconducting phase. Only a variation of the filling can induce a topological transition and according to the Table 3.2 it has to be a hole-like doping. The topological region is explicitly highlighted in cyan in the Fig. 3.21. We notice that other energy windows that are much farther from the Fermi level can be also topologically interesting with respect to the nonsymmorphic symmetries.

A final observation concerning the possibility of achieving an unconventional superconducting phase in the MX compounds arises directly from the multifold degeneracy of the electronic dispersion along the SR line. Indeed, if there are Fermi points along the SR line, due to the high degeneracy, one can expect that a high-spin pairing can be realized, in analogy to the unconventional superconductivity proposed in Refs. [130, 131]. Such observation can be deduced because at any given momentum k close to k_F there are 4-degenerate states for each spin polarization that, thus, realize a quartet for a pseudospin $T = 3/2$. We remind that the configurations associated with the quartet include sublattice and atomic orbital degrees of freedom. Then, combining the angular momentum of the quartet with the spin $s = 1/2$, the single particle electronic states at a given k close to k_F can be cast in a configuration with effective total angular momentum $J = L+s$ with amplitude $J = \{1, 2\}$. Starting from this consideration, we conclude that the pairing between the particle-hole partners at $\{k, -k\}$ can be obtained by composing single particle configurations with a given J thus building

up a total pair angular momentum J_{pair} that can range from 0 to 4. This result implies that the superconducting pairing can be in an effective high-spin state thus going beyond the conventional singlet-triplet classification. Although, the high-spin pairing can be achieved only along the SR high-symmetry lines, we observe that such occurrence would also influence the character of the pairing away from it. Assuming that the superconducting order parameter is smoothly changing across the BZ, we expect that the pairing state evolves in a way that is symmetrically compatible with the presence of a high-spin configuration along the high-symmetry SR line.

Let us now consider the possible implications of the evaluated electronic structure with respect to the magnetic properties of the MX compounds. One direct consequence of the multifold degeneracy is that there are peaks in the DOS, close to the crossing points, which naturally lead, in the presence of interaction, to a tendency to get a Stoner-like instability. On the other hand, according to our results, the fact that a two-dimensional Fermi surface can be observed and that there are almost flat Fermi lines crossing the BZ, which arise from the constraint of the nonsymmorphic symmetries, we expect pronounced nesting effects and thus the possibility of density wave instabilities. One relevant observation pertains to the removal of degeneracy in the presence of a magnetic instability. Although there are no induced gap opening, we expect that, in a similar fashion as for the Peierls instability[34], the removal of the degeneracy associated with a magnetic broken symmetry phase leads to an energy gain that stabilizes the corresponding phase. In this context, we observe that a collinear magnetic state can affect the band degeneracy in a twofold way: i) by splitting the states protected by the crystalline nonsymmorphic symmetry, and ii) by inducing new nonsymmorphic invariance and related multiple band crossings [114, 132, 133]. More specifically, for the MX materials a collinear antiferromagnetic order has been shown to partially remove the band degeneracy. Depending on the antiferromagnetic pattern, the system can selectively present multifold degenerate bands along inequivalent high symmetry lines. It is only with a noncollinear magnetic order that one achieves a complete removal of the band degeneracies. We argue that, following the comment on the energy gain by band splitting, it is such mechanism which can account for the observed magnetic order in the CrAs and MnP compounds.

Moreover, it is worth pointing out that the eight-fold degeneracy along the SR line permits to achieve a band insulating phase only for fillings which are multiple of eight contrary to the conventional twofold filling constraint due to the time-inversion degeneracy.

Finally, it is worth mentioning that evidences of spin-triplet superconductivity have been experimentally found for both CrAs and UCoGe [44, 134] along the suggested theoretical predictions. Here, due to the symmetry analogy, our results on the structure of the Fermi surface indicate that unconventional superconductivity can be also observed in WP and MnP with distinct signatures of topological superconductivity manifested by non-trivial zero-energy symmetry protected edge states. According to

our findings, in this framework, the WP could be a topological nonsymmorphic crystalline superconductor while MnP would be a trivial superconductor manifesting a topological transition only upon suitable doping.

3.7 Conclusions

In this Chapter we have studied the symmetry properties of compounds belonging to the Pnma space group with MnP-type crystal structure [28]. The band structure of these compounds, other than the time-reversal and inversion symmetries, exhibits nonsymmorphic symmetries that bring to four- or eight-fold degeneracy of the bands along some high-symmetry lines of the BZ. As a first step, we built a model Hamiltonian describing the 2D case and that allowed us to study the effects of the nonsymmorphic symmetries on the band structure and Fermi surface in this simpler problem. Then, by combining DFT with an effective low-energy model Hamiltonian which is the 3D generalization of the 2D model previuosly obtained, we have studied the electronic and structural properties of the WP compound in the presence of SOC. The emerging electronic properties are representative of the MnP-type family and also share common features with other members as CrAs and MnP compounds. As already seen for CrAs, also for the WP compound the d states dominate close to the Fermi level, while the p states are located both above and below the Fermi level. The bandwidth of WP is wider respect to that of CrAs and MnP and the structure is more distorted. This distorted structure, favored by a weak crystal field potential, produces a strong orbital mixing of the d-bands making quite difficult the identification of a reduced subset of d-orbitals for an effective model for the low energy description. The presence of the nonsymmorphic symmetries have strong implications on the multiplicity and dimensionality of the Fermi surface [135]. Moreover, the evolution of the Fermi surface topology is linked to the presence or not of Fermi points along some high symmetry directions. If the Fermi level crosses the bands along the SR line, there are eight Fermi surfaces with the presence of Fermi pockets and stripes. Depending on the electron filling, the size of Fermi pockets can increase until creating open Fermi surfaces. The electronic changeover exhibits a simultaneous modification of the Fermi surface dimensionality and topology of the Fermi surface. This picture brings towards four concentric 2D-Fermi surfaces in this class of materials. When the role of the SOC is considered, we show that the interplay between the SOC interaction and the inter-orbital degrees of freedom allows a selective removal of the band degeneracy. We point out that 2D Fermi surfaces were observed also in quasi 2D-superconductors like cuprates [2, 136], iron-pnictides [4, 137, 138] and ruthenates [3, 48, 66, 139, 140, 141]. However, while in the iron-pnictides the FS are electron-like, in this class of compounds they are hole-like. Furthermore, the transition-metal pnictides MX are intrinsically 3D while cuprates [2, 136], iron-pnictides [4, 137, 138] and ruthenates [3, 48, 66, 139, 140, 141] may be considered such as quasi 2D systems [140]. Moreover,

the presence of these 2D sheets could affect the transport and superconducting properties of this class of materials. We would like also to stress that the study of nodal excitations could also be relevant when the phonons effects are concerned, allowing to explain the unusual resistivity behavior [49] and possibly shedding light on the mechanism beyond the superconducting pairing [44, 134].

Chapter 4

The quasi-one-dimensional superconductor $K_2Cr_3As_3$

In this Chapter we present the construction of a minimal tight-binding model Hamiltonian, which reproduces with high accuracy the band structure of the quasi-one-dimensional superconductor $K_2Cr_3As_3$ around the Fermi level, as obtained via first-principle calculations. We demonstrate that such description can be derived starting from a minimal set of five quasi-atomic orbitals with mainly d character, namely four planar orbitals (d_{xy} and $d_{x^2-y^2}$ for each of the two planes KCr_3As_3 and $K_3Cr_3As_3$) and a single out-of-plane one (d_{z^2}). Moreover, we derive an explicit simplified analytical expression of our five-band tight-binding model, which includes three nearest-neighbor (NN) hopping terms along the z direction and one NN within the xy plane.

Such tight-binding representation of the $K_2Cr_3As_3$ band structure is obtained within a three-stage approach consisting of the following steps: (i) Guided by first-principles DFT calculations, we first construct the model based on the atomic Cr and As orbitals and use it to investigate the orbital character and the symmetry of the bands which dominate in a certain energy window around the Fermi level; (ii) we use the Löwdin procedure to downfold the original full Hamiltonian into a much smaller space spanned by a set of atomic Cr and As orbitals which are symmetric with respect to the basal plane; iii) the knowledge of the results of steps i) and ii) allows to formulate, within a Wannier projection, a tight-binding description based on five atomic-like orbitals of mainly d character, which are spatially localized around virtual lattice sites located at the center of the Cr-triangles of the $K_3Cr_3As_3$ planes, stacked along the chain direction.

We point out that this minimal model well reproduces all the details of the low-energy band structures in a broad energy region around the Fermi level, which makes it a remarkable improvement with respect to previous three-band models. Moreover, we expect that, by solving such minimal model and its extensions using suitable approximations, one may obtain information about the superconducting pairing mechanism especially for the pairing symmetry, starting from a more complete band structure.

The Chapter is organized as follows: the first section is devoted to the state of the art, in the second section we analyze the band structure with a DFT method, in the third we study the electronic properties by using a tight-binding method and then we

apply the Löwdin procedure, the fourth is devoted to the building up of our minimal five-bands model, and in the last section we give the conclusions.

4.1 State of the art

Very recently the ambient-pressure superconductivity was discovered at 6.1 K in a Cr-based arsenide, $K_2Cr_3As_3$, and, subsequently, in a whole class represented by the family $A_2Cr_3As_3$, with A being Na [13], K [14], Rb [15] or Cs [16]. Remarkably, these Cr-based superconductors have a quasi-one-dimensional (Q1D) crystal structure that consists of $[(Cr_3As_3)^{2-}]_\infty$ double-walled nanotubes in which chromium atoms form the inner wall and arsenic atoms the outer one. These nanotubes are in turn separated by columns of A^+ ions [13, 14, 15, 16]. These novel superconductors display intriguing physical properties, both in the normal and in the superconducting phase, which are under intense investigations especially to clarify the role played by the reduced dimensionality and by the electronic correlations.

Focusing on $K_2Cr_3As_3$ and first on its normal properties, a large specific heat coefficient of 70-75 mJ K^{-2} mol^{-1} indicates strong electron correlations and a linear temperature dependence of the resistivity from 7 to 300 K supports the hypothesis of a Tomonaga-Luttinger liquid (TLL) behavior [14], that how we said before is predictable for Q1D systems with strong correlations. Other points in favour of a TLL behavior come from preliminary ARPES investigations [142] and NMR measurements [143] of the nuclear spin-lattice relaxation rate $1/T_1$. The first indicate the presence of two Q1D Fermi surface sheets with linear dispersions and a spectral weight of the Q1D bands decreasing near the Fermi level according to a linear power law, in an energy range of $\sim$ 200 meV [142]. The second show a strong enhancement in the Cr nanotubes of the spin fluctuations above T_c, with the power-law temperature dependence $1/T_1T \sim T^{-\gamma}$ ($\gamma \simeq 0.25$) [143]. Differently, Kong et al. [144] report a T^3 dependence of resistivity from 10 to 40 K, giving rise to a long and still unresolved debate on the unidimensionality of the system. The Debye temperature is found to be 220 K and the specific heat jump at the superconducting transition is 2.2 T_C [144]. The upper critical field is anisotropic with different amplitudes between fields parallel and perpendicular to the rodlike crystals [144].

Regarding the magnetism, in the case of $K_2Cr_3As_3$ Jiang et al. [145] substain that the triangular geometry tends to frustrate antiferromagnetism, so that the nonmagnetic phase is the most stable one, while Wu et al. [146] predict that $K_2Cr_3As_3$ and $Rb_2Cr_3As_3$ possess strong frustrated magnetic fluctuations and are nearby to a novel in-out co-planar magnetic ground state. Interestingly, the magnetism increase in the $A_2Cr_3As_3$ when we go from the K to the heavier Cs. In 2018 Taddei et al. [147, 148] found significant phonon instability, which, under energy minimization, corresponds to a frustrated orthorhombic distortion in $K_2Cr_3As_3$. This discovery suggest a more

complex phase diagram with subtle interplays of structure, electron-phonon and magnetic interactions [147] and that needs of further investigation for $K_2Cr_3As_3$ and other superconductors belonging to the same class.

There are many experiments that point towards an unconventional kind of superconductivity. One indication is given by NMR measurements [143] and is the absence of the Hebel-Slichter coherence peak in $1/T_1$ below T_C. The same kind of indication comes from muon-spin rotation measurements [149], which provide evidence of a possible d-wave superconducting pairing, as well as from measurements of the temperature dependence of the penetration depth $\Delta\lambda = \lambda(T) - \lambda(0)$ [150]. For the latter, a linear behavior is observed for $T \ll T_c$, instead of the exponential behavior of conventional superconductors, indicating the presence of line nodes in the superconducting gap and thus supporting the hypothesis of an unconventional nature of the superconducting phase [150].

Theoretical studies aimed at the analysis of the electronic, magnetic and superconducting properties of $K_2Cr_3As_3$ have been developed. DFT investigations [145] show that Cr-3d orbitals, specifically the d_{z^2} , d_{xy} and $d_{x^2-y^2}$ ones, dominate the electronic states near the Fermi energy. Three bands crossing the Fermi level to form one 3D Fermi surface sheet and two Q1D sheets [145]. Based on this, three- [119] and six-band [151] models have been built and they show in both weak and strong coupling limits that a triplet p_z-wave pairing is the leading pairing symmetry for physically realistic parameters. Another theoretical work, based on the study of a twisted Hubbard tube modelling the $[(Cr_3As_3)^{2-}]_\infty$ structure, shows that the system tends to exhibit triplet superconducting instabilities within a reasonable range of the interaction parameters [152]. By using an extended Hubbard model with three molecular orbitals in each unit cell, Zhou et al. [153] find that, both for small and large U, dominant pairing channel is always a spin-triplet one.

$K_2Cr_3As_3$ presents a Q1D and hexagonal crystal structure at room temperature that consists of double walled $[(Cr_3As_3)^{2-}]_\infty$ nanotubes separated by columns of K^+ ions, with chromium atoms forming the inner wall and arsenic atoms the outer one, as represented in Fig. 4.1.

4.2 Band structure using DFT

In this section, we present the first-principle calculations which supply a basis for constructing the tight-binding modeling of the $K_2Cr_3As_3$ band structure that will be described in the following sections. The real space Hamiltonian matrix elements have been set according to the outcome of DFT calculations, performed by using the VASP package [50, 51, 52, 53]. In such an approach, the core and the valence electrons have been treated within the PAW method [54] and with a cutoff of 500 eV for the plane

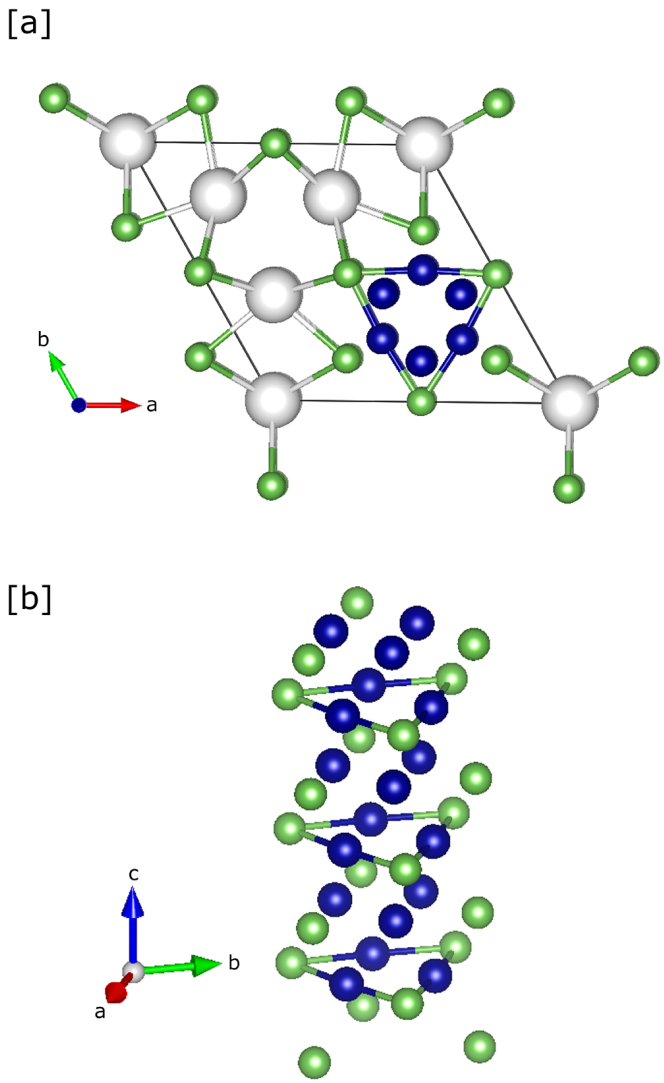

FIGURE 4.1: Crystal structure of $K_2Cr_3As_3$. The colours blue, green and white denote Cr, As and K atoms, respectively. (a) Top view of the primitive cell. (b) The double-walled nanotube formed by Cr and As atoms.

wave basis. All the calculations have been performed using a 4×4×10 k-point grid. For the treatment of the exchange correlation, the LDA and the Perdew-Zunger [55] parametrization of the Ceperley-Alder [56] data have been considered. After obtaining the Bloch wave functions, the maximally localized Wannier functions [57, 58] are constructed using the WANNIER90 code [59]. To extract the Cr 3d and As 4p electronic bands, the Slater-Koster interpolation scheme has been used, in order to determine the real-space Hamiltonian matrix elements [59].

The role of the electronic correlations on the energy spectrum of $K_2Cr_3As_3$ has also been explored. To this purpose, we have performed first-principle calculations taking into account the effect of the local Hubbard interactions, assumed to be non-vanishing on all the Cr d orbitals, and efficiently parametrized by a finite number of Slater integrals. We follow the convention [154] of identifying U with the Slater integral F^0 and the Hund coupling with F^2 and F^4. The direct calculation gives for the intra-t_{2g} orbital Hund interaction the value $J_H = 0.15\ U$ [155]. Considering that previous studies [145] indicate that the system is moderately correlated, we have assumed for U values ranging in a interval going from 0 to 4 eV. The band structure obtained in the two limiting cases of $U = 0$ and $U = 4$ eV is reported in Fig. 4.2. As far as the $U = 0$ case is concerned, the results are in agreement with the literature [145]. The character of the bands at low energies is mainly due to the d states of Cr atoms, whereas the p states of the As atoms are located few electronvolts above and below the Fermi level, as also found for CrAs.

We can see that, apart from a slight increase of the energy bandwidth corresponding to the chromium states being pushed away from the Fermi level, electronic correlations on chromium orbitals barely affect the energy spectrum. In particular, the band energy separation occurring when the Coulomb repulsion is turned on is one order of magnitude lower than the value of U considered in the calculation. This result thus seems to confirm that $K_2Cr_3As_3$ is in a moderate-coupling regime, characterized by a robust metallic phase, expected to remain stable also under the influence of pressure, strain or doping. As also found for CrAs, the nonmagnetic and the antiferromagnetic phases turn out to be very close in energy. In the case of $K_2Cr_3As_3$, the triangular geometry tends to frustrate antiferromagnetism, so that the nonmagnetic phase is the most stable one.

4.3 Tight binding analysis of the electronic properties and Löwdin procedure

In this section, we derive a tight-binding model obtained from a basis set of localized atomic orbitals at each site of the crystal structure. Our starting point will be the most reliable tight-binding description that is capable to reproduce the LDA band structure close to the Fermi level. This description will then be used to examine in detail the orbital character of the energy bands, which will be resolved both with respect to the energy itself and to the k vector in the main high-symmetry points of

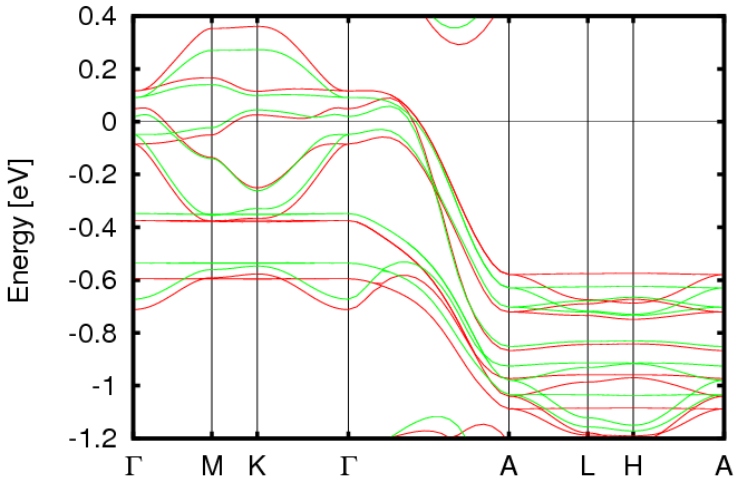

FIGURE 4.2: LDA+U band structure near the Fermi level for $U = 0$ (green lines) and $U = 4$ eV (red lines).

the BZ [29, 30].

We construct the tight-binding model by considering all the atomic orbitals that participate to conduction, namely Cr $3d$ and As $4p$ orbitals. The basis in the Hilbert space is given by the vector

$$\phi_i^\dagger = (d_{i,xy}^\dagger, d_{i,x^2-y^2}^\dagger, d_{i,z^2}^\dagger, p_{i,x}^\dagger, p_{i,y}^\dagger, d_{i,yz}^\dagger, d_{i,xz}^\dagger, p_{i,z}^\dagger), \tag{4.1}$$

where i is the lattice index and the orbitals are ordered having first those symmetric with respect to the basal plane and then the antisymmetric ones.

The tight-binding Hamiltonian is defined as

$$H = \sum_i \phi_i^\dagger \hat{\varepsilon}_i \phi_i + \sum_{i,j} \phi_i^\dagger \hat{t}_{i,j} \phi_j \tag{4.2}$$

where i and j denote the positions of Cr or As atoms in the crystal, and $\hat{\varepsilon}_i$ and $\hat{t}_{i,j}$ are matrices whose elements have indices associated with the different orbitals involved. The first term of the Hamiltonian takes into account the on-site energies, with $(\hat{\varepsilon}_i)^{\alpha\beta} = \varepsilon_i^\alpha \delta_{\alpha,\beta}$, while the second term describes hopping processes between distinct orbitals, with amplitudes given by the matrix elements $t_{ij}^{\alpha\beta}$. The latter are given by the expectation values of the residual lattice potential $V(\mathbf{r})$ on the complete orthogonal set of the Wannier functions $\phi_\alpha(\mathbf{r} - \mathbf{R}_i)$:

$$t_{ij}^{\alpha\beta} = \left\langle \phi_\alpha(\mathbf{r} - \mathbf{R}_i) | V(\mathbf{r}) | \phi_\beta(\mathbf{r} - \mathbf{R}_j) \right\rangle . \tag{4.3}$$

Their values are obtained according to the procedure described in the previous section. The Hamiltonian in Eq. (4.2) is a 48×48 matrix because the primitive cell contains six Cr and six As atoms and we have to consider five d orbitals for each Cr

atom and three p orbitals for each As atom.

We have carried out a detailed analysis in order to address the nature of the electronic bands provided by *ab-initio* calculations, in particular with respect to its supposed one-dimensionality. Such study reveals that considering only the hoppings between the orbitals of the atoms that lie within a single sub-nanotube fails completely to describe the in-plane band structure, not even allowing the correct description of the band structure along the z axis. Such result is also in agreement with previous DFT calculations showing that, in contrast with other quasi-1D superconductors, $K_2Cr_3As_3$ exhibits a relatively complex electronic structure and the Fermi surface contains both 1D and 3D components [145]. In the following, we perform the calculations by first considering the hopping processes within the quasi one-dimensional $[(Cr_3As_3)^{2-}]^{\infty}$ double-walled nanotubes only, and then including step by step inter-tube and longer-range intra-tube processes.

1) The most relevant sub-geometry of the $K_2Cr_3As_3$ lattice is a quasi-one dimensional double-walled sub-nanotube extending mainly along the z-axis. So, as a first step, we consider only hopping processes between intra-tube atoms. Referring to the notation $\boldsymbol{R} = n_1\boldsymbol{a}_1 + n_2\boldsymbol{a}_2 + n_3\boldsymbol{a}_3$, we start by limiting ourselves to the primitive cells denoted by (n_1,n_2,n_3)=(0,0,0), (0,0,1) and (0,0,-1), as shown in Fig. 4.3(a-b).

The band structure that we have obtained is shown in Fig. 4.4 in an energy window around the Fermi level, with the DFT spectrum being also reported for comparison. We can clearly see that this choice of hoppings not only misses completely the in-plane band structure, but it does not even allow to describe correctly the band structure along the ΓA line. This unveils an overlooked relevance of in-plane virtual processes that affect the z-axis physics. It is evident that more reliable results require in any case the inclusion of hopping processes involving longer range intra-tube cells as well as inter-tube ones.

2) As a second step, we include in the diagonalization procedure inter-tube hoppings in the x-y plane ($n_3 = 0$), taking into account the contributions coming from the cells (1,0,0), (-1,0,0), (0,1,0), (0,-1,0), (1,-1,0), (-1,1,0), (1,1,0) and (-1,-1,0) (see Fig. 4.3(c)). The comparison of the band structure correspondingly obtained with the one given by DFT (see Fig. 4.5) makes evident that the agreement improves along the ΓA line as well as along the other lines of the BZ, though there are still some qualitative differences, also at the Fermi level.

3) In order to get a truly satisfactory agreement, it is necessary to include all hopping processes up to the fifth-neighbor cells along the z-axis (from $n_3 = 5$ to $n_3 = -5$), together with the in-plane hoppings up to the second-neighbor cells (see Fig. 4.6). Our analysis suggests that the LDA results arise from a delicate combination of several very

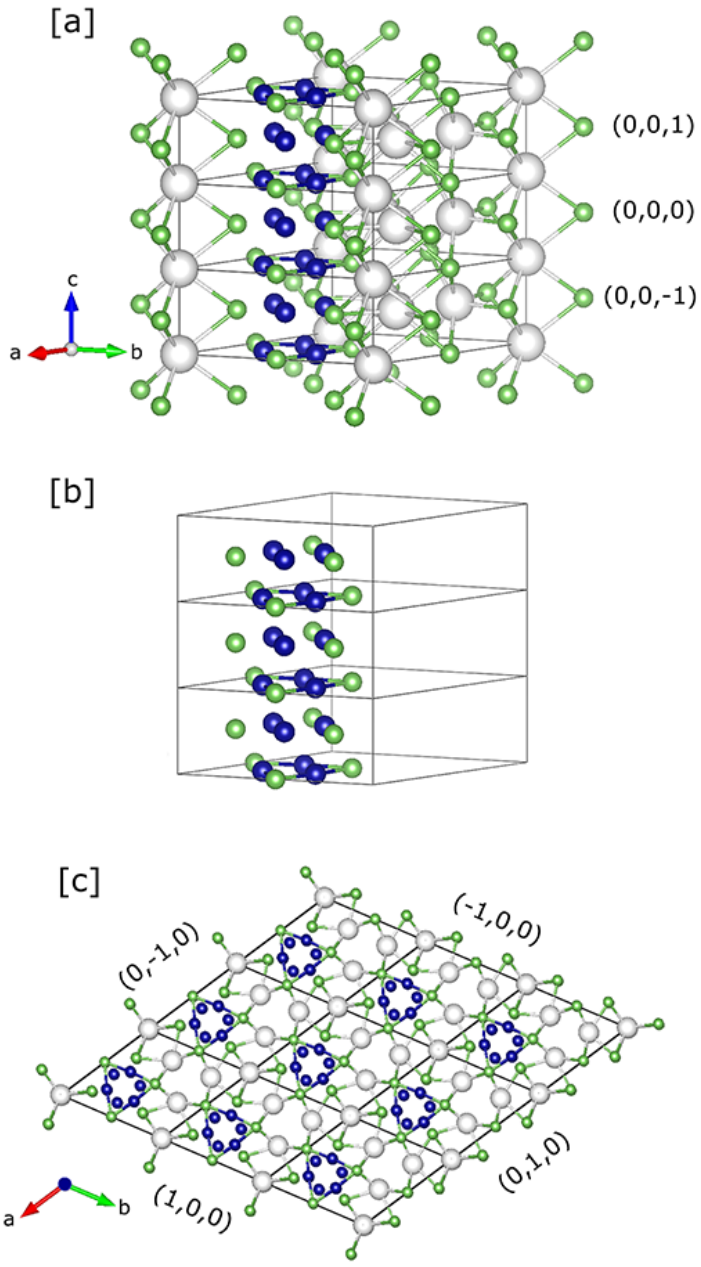

FIGURE 4.3: (a) (0,0,0), (0,0,1) and (0,0,-1) primitive cells of $K_2Cr_3As_3$. (b) Atoms taken into account in the diagonalization procedure when only short-range intratube hopping processes are considered. (c) (0,0,0), (1,0,0), (-1,0,0), (0,1,0), (0,-1,0), (1,-1,0), (-1,1,0), (1,1,0) and (-1,-1,0) primitive cells.

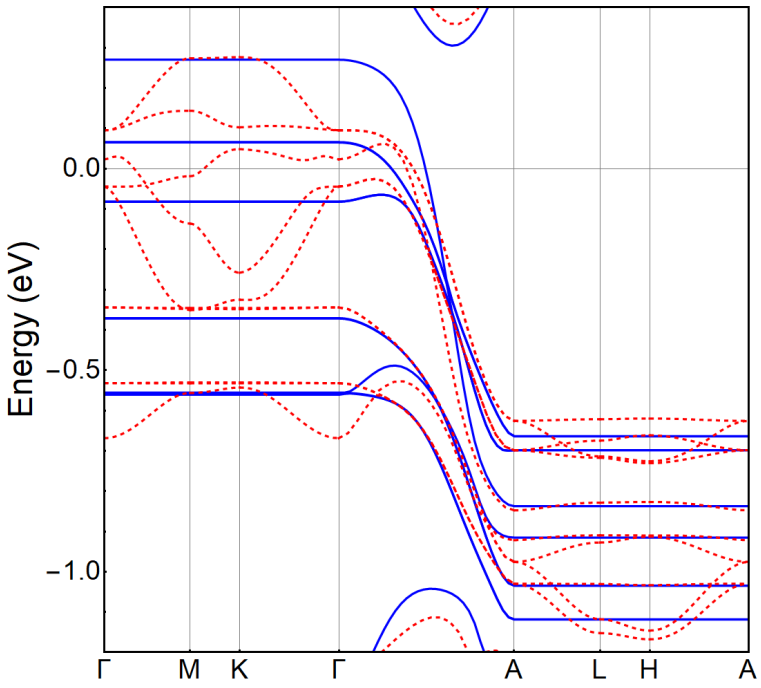

FIGURE 4.4: Comparison between the tight-binding band structure obtained considering hoppings within the (0,0,0), (0,0,1) and (0,0,-1) primitive cells (blue lines) and the DFT band structure (red dashed lines), in an energy range around the Fermi level (set equal to zero).

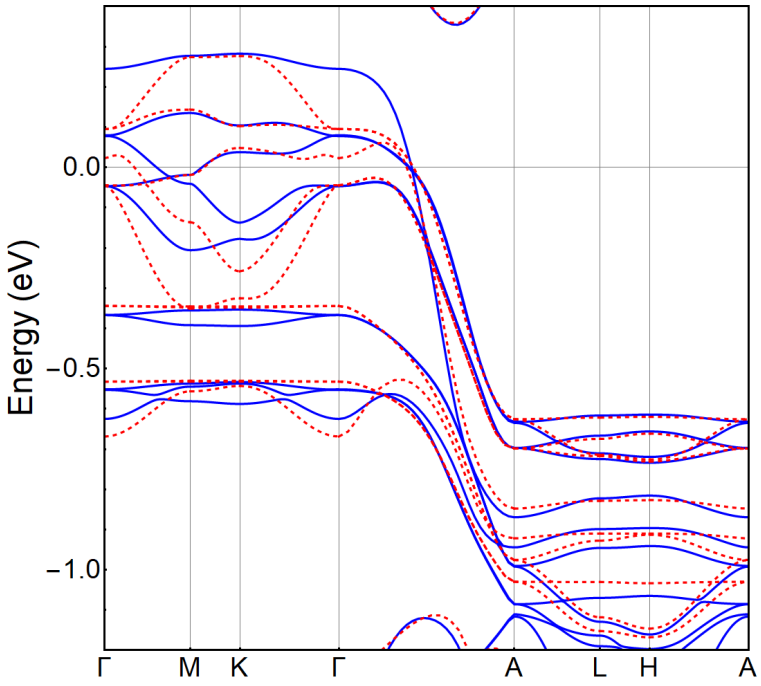

FIGURE 4.5: Same as in Fig. 4.4, with the tight-binding calculations extended to hopping processes in the (1,0,0), (-1,0,0), (0,1,0), (0,-1,0), (1,-1,0), (-1,1,0), (1,1,0) and (-1,-1,0) primitive cells.

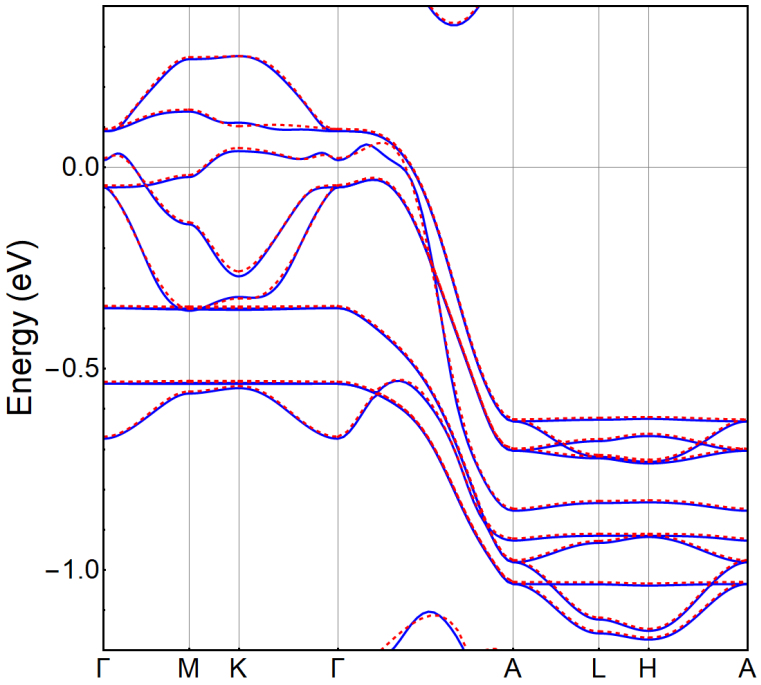

FIGURE 4.6: Same as in Fig. 4.5, with the tight-binding calculations further extended to fifth neighbour cells along the$z$-axis (from $n_3 = 5$ to $n_3 = -5$) and to second-neighbor in-plane cells.

small contributions, which are crucial in order to faithfully determine the dispersion of the bands that cut the Fermi level perpendicular to the chain direction ($\Gamma MK\Gamma$ path).

Diagonalizing the Hamiltonian in Eq. 4.2 and retaining the hopping terms of the step 3), we obtain an energy spectrum that perfectly matches the one for $U = 0$ in Fig. 4.2 (see Fig. 4.6), as evaluated along the high symmetry path of the hexagonal BZ considered in Ref. [60]. Accordingly, the results presented in this section have been obtained within this framework. However, although the agreement is extremely satisfactory, we cannot consider successfully concluded our quest for a minimal model because of the need for so many hopping parameters. Therefore, in order to gain sufficient insight in the behavior of the system and design an efficient reduction procedure leading us to a real minimal model, we proceed with the analysis of the partial DOS and of the orbital character of the bands.

In order to evaluate the orbital character of the low-energy excitations around the Fermi level, we calculate the total DOS, together with its projection on the Cr and As relevant orbitals. The total DOS is obtained from the standard definition (see Eq. 2.7). Our grid here consists of $6 \times 6 \times 12$ $\boldsymbol{k}$ points. The variance is assumed to be $\sigma = 0.025$ eV. The total DOS reported in Fig. 4.7 exhibits, as expected, peaks in correspondence of the flat portions of the energy spectrum. Similarly to what found for CrAs, the DOS has a predominant As character at energies of the order of ± 2 eV away from the Fermi level. The peaks near -0.5 eV and 1 eV are instead associated with

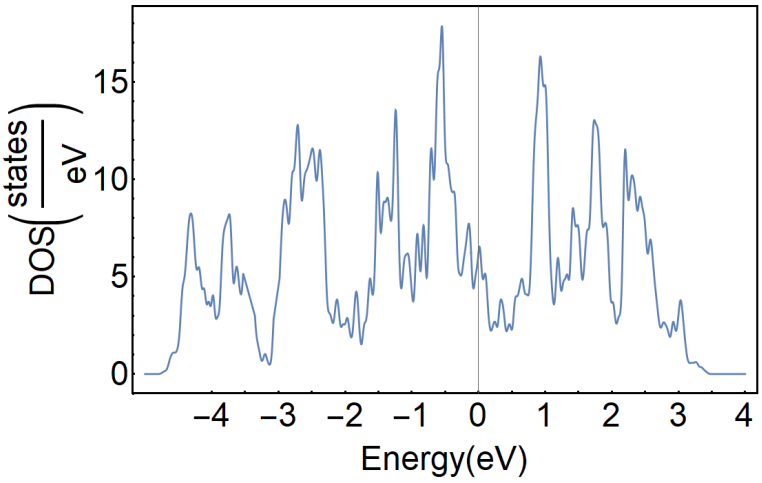

FIGURE 4.7: Total DOS of $K_2Cr_3As_3$ (Fermi level is at zero energy).

the Cr-d_{yz} and d_{xz} orbitals, whereas, differently from what happens for CrAs, there is no clear prevalence of Cr states around the Fermi energy, but rather the Cr-d_{xy}, $d_{x^2-y^2}$ and d_{z^2} and the As-p_x and p_y contributions are all relevant, as we will point out below in more detail.

We have also determined the projections of the total DOS on the orbitals of the Cr or As atoms of the material. These are defined as

$$\rho_\alpha(\epsilon) = \frac{1}{N}\sum_{\boldsymbol{k}} |\langle \psi_{\boldsymbol{k}} | f_\alpha \rangle|^2 \delta(\epsilon - \epsilon_{\boldsymbol{k}}) \tag{4.4}$$

where $\psi_{\boldsymbol{k}}$ are the eigenstates of our problem and f_α represents the orbital on which we project (the delta functions are approximated with Gaussians). The projected DOSs associated with the orbitals symmetric with respect to the basal plane, i.e. d_{xy}, $d_{x^2-y^2}$, d_{z^2}, p_x, p_y, are shown in Fig. 4.8, while those associated with the antisymmetric ones, i.e. d_{yz}, d_{xz}, p_z, are presented in Fig. 4.9.

Their behavior confirms the results of first-principle calculations, namely the orbitals that dominate the low-energy excitations are the chromium d_{xy}, $d_{x^2-y^2}$ and d_{z^2} [145], with the highest contribution corresponding to a pronounced peak at the Fermi energy associated with the d_{xy} and $d_{x^2-y^2}$ orbitals. Nonetheless, we see that an appreciable contribution also comes from As p_x and p_y orbitals, this signaling the difficulty of reducing the full Hamiltonian (4.2) to a simpler effective one where the d and the p orbital degrees of freedom are efficiently disentangled. Finally, from Fig. 4.9 we see that the projected DOS for antisymmetric orbitals exhibits negligible contribution at the Fermi energy, providing evidence of the decoupling between the two sectors corresponding to orbitals symmetric or antisymmetric with respect to the basal plane.

To gain a better insight into the nature of the isolated set of ten bands in the energy window [-1.2 eV, 0.4 eV] around the Fermi level, we have performed a detailed analysis of the orbital character of each energy level along the main directions in the BZ. This

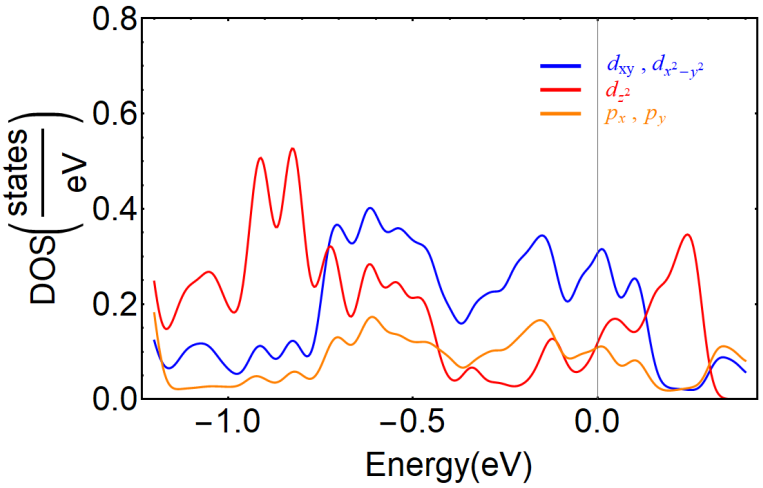

FIGURE 4.8: DOSs per atom of $K_2Cr_3As_3$ projected onto orbitals symmetric with respect to the basal plane, i.e. d_{xy} and $d_{x^2-y^2}$ (blue line), d_{z^2} (red line) and p_x and p_y (orange line). The curves have been obtained averaging the projected DOSs over all the atoms of the unit cell.

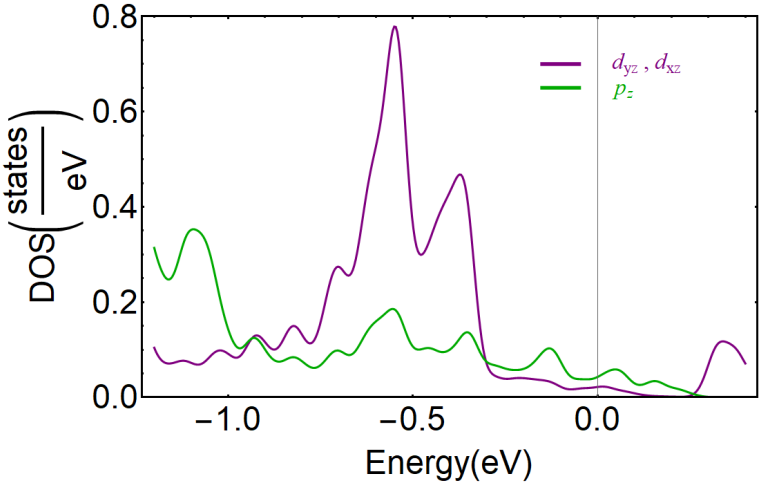

FIGURE 4.9: Same as in Fig.4.8 for antisymmetric orbitals, i.e. d_{yz} and d_{xz} (purple line) and p_z (green line).

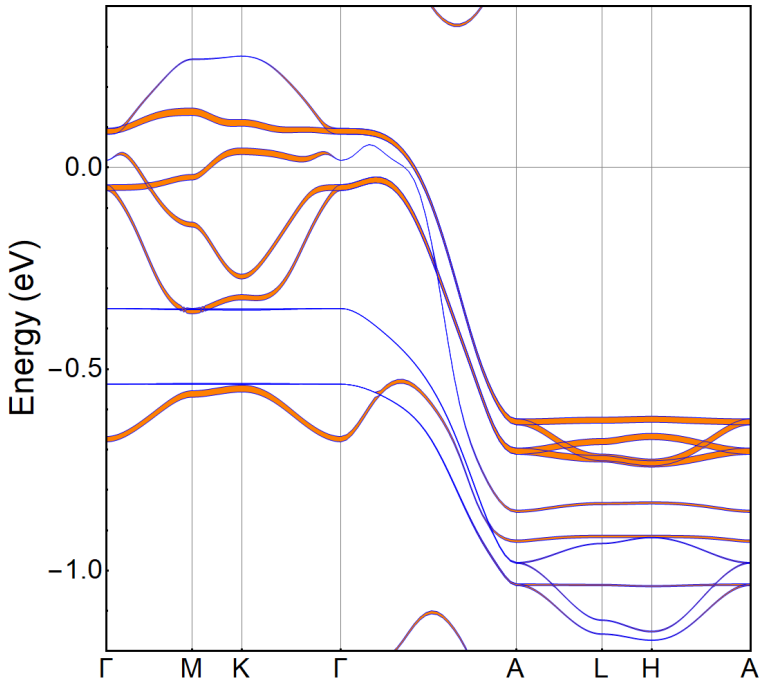

FIGURE 4.10: Contribution to the tight binding band structure (blue curve) of the d_{xy} and $d_{x^2-y^2}$ orbitals, represented as fat band (in orange).

is provided through the "fat bands" representation, where the width of each band-line is proportional to the weight of the corresponding orbital component, as shown in Figs. 4.10-4.14. One can notice that an accurate description of the conduction and valence bands along the various paths involves both Cr and As. As one can see, the three bands crossing the Fermi level are mainly built from the d_{xy}, $d_{x^2-y^2}$, d_{z^2} orbitals of Cr, with a degree of mixing which is highly dependent on the selected path in the BZ.

As our previous analysis suggests, the symmetric orbitals d_{xy}, $d_{x^2-y^2}$, d_{z^2}, p_x and p_y dominate at the Fermi level, so one can project out the low-lying degrees of freedom using the Löwdin downfolding procedure [62].

Schematically, given the basis defined in Eq.(4.1), the matrix has the structure

$$H = \left[\begin{array}{c|c} H_{ss} & H_{sa} \\ \hline H_{as} & H_{aa} \end{array}\right], \tag{4.5}$$

where H_{ss} is the submatrix including hoppings between symmetric orbitals, H_{sa} hoppings between symmetric and anti-symmetric orbitals, and H_{aa} hoppings between anti-symmetric orbitals.

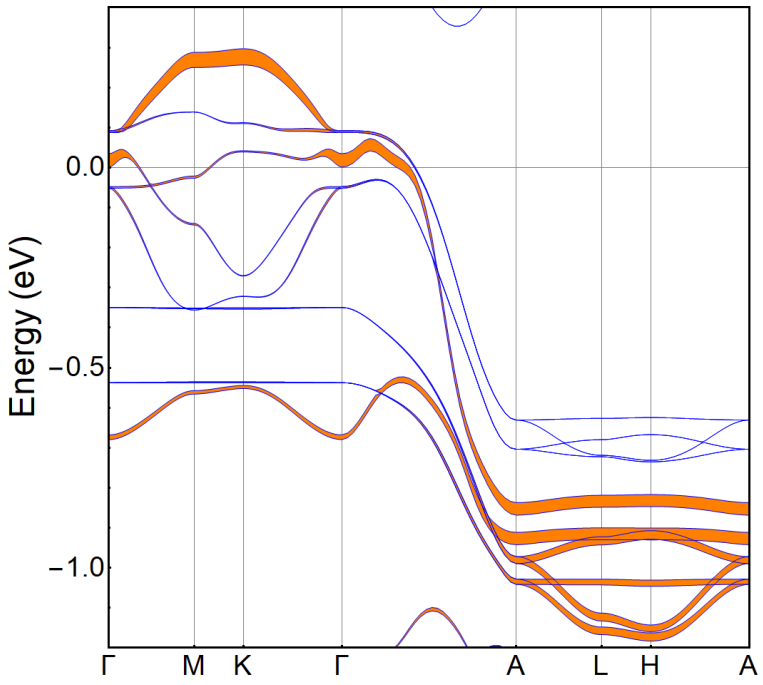

FIGURE 4.11: Same as in Fig.4.10, referred to the d_{z^2} orbital.

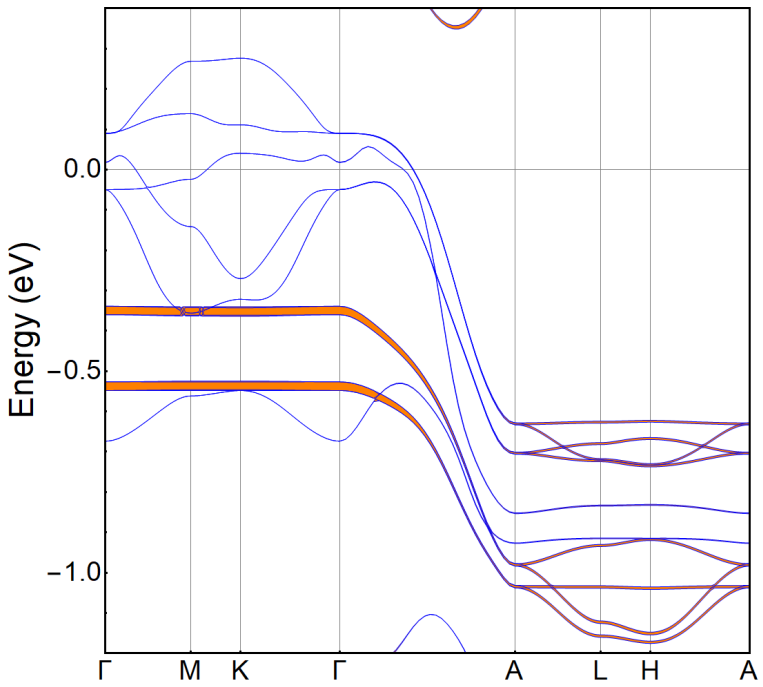

FIGURE 4.12: Same as in Fig.4.10, referred to the d_{xz} and d_{yz} orbitals.

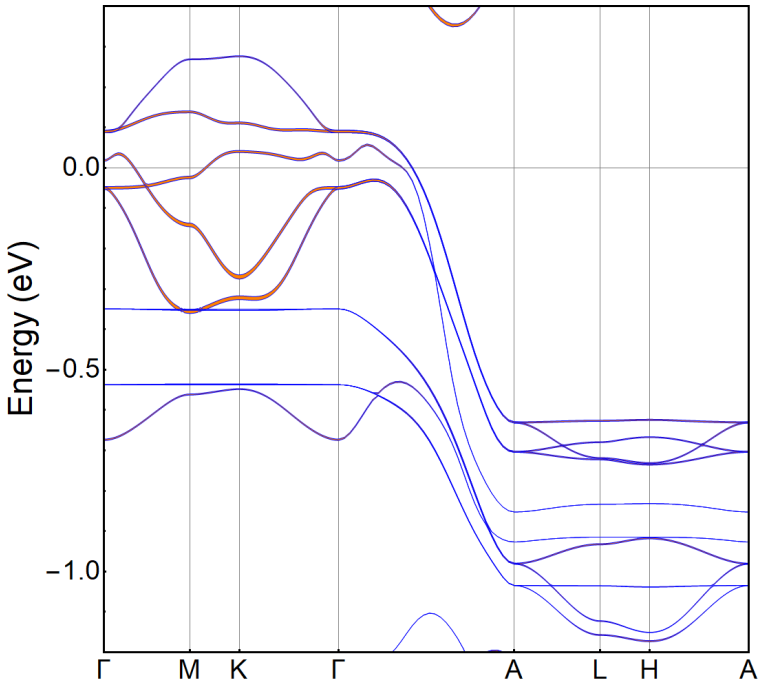

FIGURE 4.13: Same as in Fig.4.10, referred to the p_x and p_y orbitals.

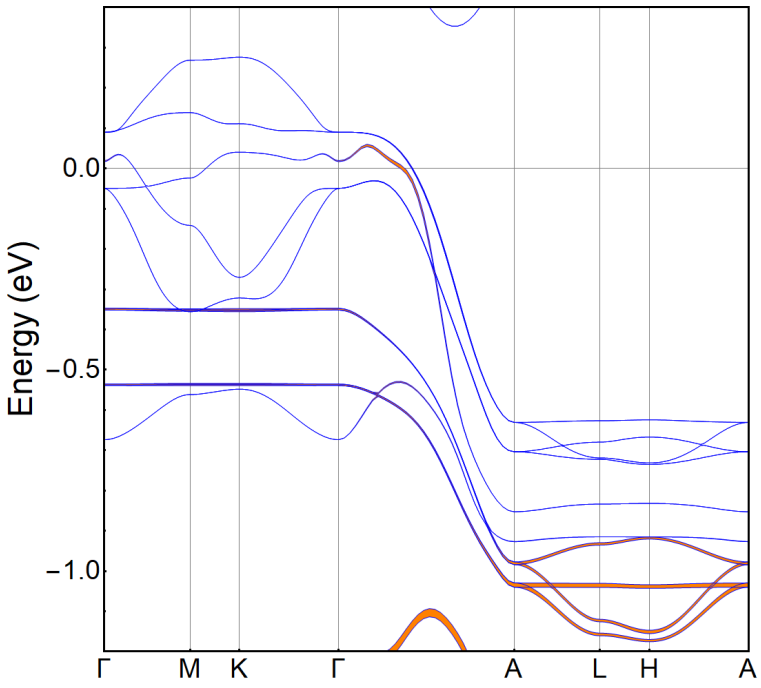

FIGURE 4.14: Same as in Fig.4.10, referred to the p_z orbital.

The submatrices are in turn made of block matrices. Considering for instance H_{ss}, we have

$$H_{ss} = \left[\begin{array}{c|c} H_{Cr_sCr_s} & H_{Cr_sAs_s} \\ \hline H_{As_sCr_s} & H_{As_sAs_s} \end{array}\right], \tag{4.6}$$

where the subscripts indicate the orbitals involved, so that

$$H_{Cr_sCr_s} = \begin{bmatrix} H_{xy/xy} & H_{xy/x^2-y^2} & H_{xy/z^2} \\ H_{x^2-y^2/xy} & H_{x^2-y^2/x^2-y^2} & H_{x^2-y^2/z^2} \\ H_{z^2/xy} & H_{z^2/x^2-y^2} & H_{z^2/z^2} \end{bmatrix},$$

$$H_{As_sAs_s} = \begin{bmatrix} H_{x/x} & H_{x/y} \\ H_{y/x} & H_{y/y} \end{bmatrix}.$$

and similarly for $H_{Cr_sAs_s}$. Here xy, x^2-y^2, z^2, yz and xz denote the five d orbitals of the Cr atoms, while x, y and z denote the three p orbitals of the As atoms. For example, H_{xy/x^2-y^2} is the submatrix that includes all the hopping processes between the d_{xy} and $d_{x^2-y^2}$ orbitals belonging to the six chromium atoms.

Referring to the matrix of Eq. (4.5) and downfolding the H_{aa} submatrix, the solution of the original eigenvalue problem is mapped to that of a corresponding effective Hamiltonian $\widetilde{H}_{ss}$, whose rank is 30, with $\widetilde{H}_{ss}$ given by [22]

$$\widetilde{H}_{ss}(\varepsilon) = H_{ss} - H_{sa}\left(H_{aa} - \varepsilon\mathbb{I}\right)^{-1} H_{as}\,. \tag{4.7}$$

Using this technique, we get the low-energy effective Hamiltonian projected into the subsector given by the symmetric orbitals, going beyond the simpler complete Wannier function method. The band structure that we have obtained applying the Löwdin procedure is shown in Fig. 4.15, where the DFT spectrum near the Fermi level is also reported for comparison. We can see that the band structure near the Fermi level is caught to a high degree of approximation and the agreement is almost complete. The d and p anti-symmetric orbitals thus can be fully disentangled from the symmetric ones, as a consequence of the peculiar geometry corresponding to the arrangement of the chromium atoms.

It is worth noting that we still have a disagreement in the A-L-H-A region. Such an occurrence is due to the predominance of the weight of the d_{z^2} orbital in that region of the BZ, although the corresponding bands are somehow distant from the Fermi surface.

4.4 Derivation of a minimal five-band tight-binding model

On the basis of the indications provided by the orbital characterization of the band structure and by the Löwdin procedure, we now introduce a minimal tight-binding model allowing to satisfactorily reproduce the energy spectrum around the Fermi energy in the whole **k**-space. We start by referring to the isolated set of ten bands

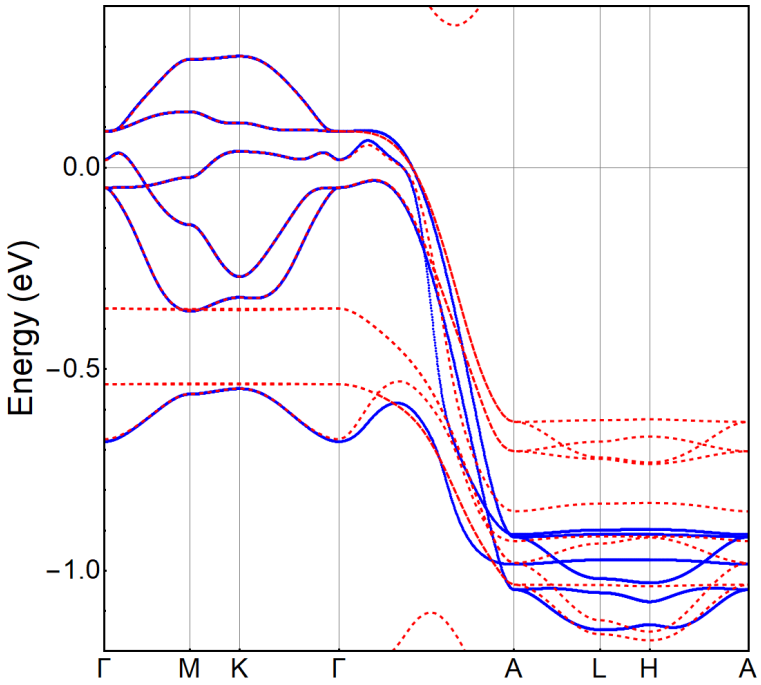

FIGURE 4.15: Comparison in the energy range around the Fermi level between the DFT band structure (red dashed lines) and the one obtained from the Löwdin downfolding procedure described in the text (blue lines).

developing in the energy range going approximately from -1.2 to 0.4 eV (see, for instance, Fig. 4.15). The fat band representation used in Figs. 4.10-4.14 provides evidence that these bands have mainly the character of the orbitals that are symmetric with respect to the basal plane. The Löwdin projection clearly demonstrated that downfolding the ten bands over the six symmetric ones, it is possible to obtain a very good description of the energy bands in proximity of the Fermi energy. These results naturally suggest a further refinement of our calculations, consisting in an application of the Wannier method taking explicitly into account the predominant weight of the symmetric states. We eventually find that this combination of the Löwdin and the Wannier approaches allows to obtain a fully reliable minimal tight-binding model.

We observe that the non-dispersive bands in the k_z=0 plane present an anti-symmetric character with weight mainly coming from d_{xz} and d_{yz} orbitals. Moreover, as one can see from the behavior of the DOS shown in Fig. 4.9, the contribution at the Fermi level of these bands, as well as the one of the p bands, is small compared to that of the symmetric ones. This suggests to exclude the anti-symmetric bands from the construction of a simplified model Hamiltonian, and thus to consider only the six symmetric ones, associated with two d_{xy}, two $d_{x^2-y^2}$ and two d_{z^2} orbitals. A further simplification is applied limiting to one the number of the d_{z^2} orbital, in consideration of the fact that the corresponding band is the one lying farther from the Fermi energy. We thus perform the Wannier calculation referring to a five-band effective model, consistently with the fact that four bands cut the Fermi level, one of

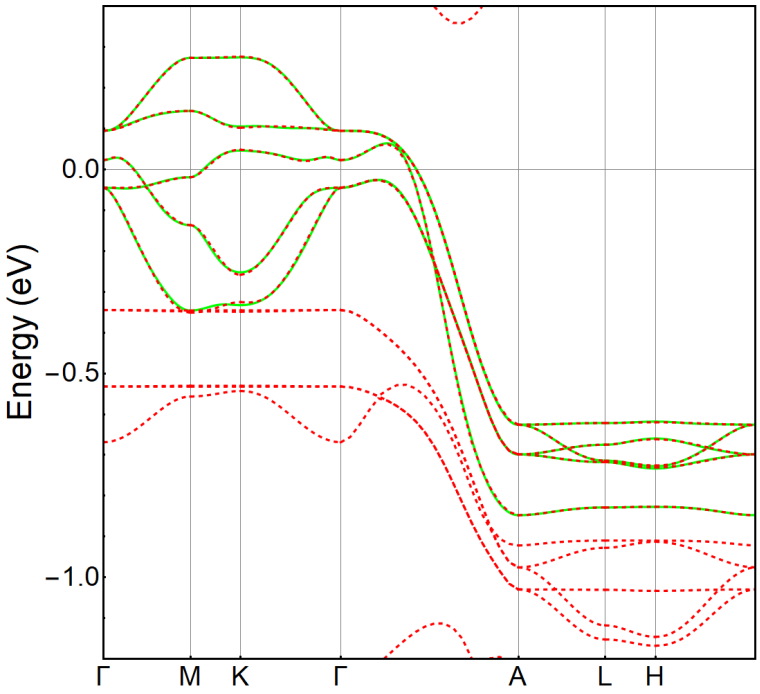

FIGURE 4.16: Comparison between the LDA band structure (red dashed lines) and the one obtained from the five-band model described in the text (green solid lines).

them being doubly degenerate at Γ point.

Since chromium-based compounds, such as $K_2Cr_3As_3$, exhibit weak or moderate electronic correlations, they have a covalent character rather than a ionic one, so that, in the case of low-dimensional systems, a Wannier function can also be placed between equivalent atoms [20]. Our choice is to place d_{xy}, $d_{x^2-y^2}$, and d_{z^2} wave functions in the middle of the Cr-triangle belonging to the KCr_3As_3 plane, locating the other two d_{xy} and $d_{x^2-y^2}$ wave functions in the middle of the Cr-triangle lying in the $K_3Cr_3As_3$ plane. The interpolated band structure obtained by this method is shown in Fig. 4.16 together with the DFT band structure. We can observe a perfect match between the two spectra, thus demonstrating that our five-band model allows to describe the low energy physics in a range of about 0.3 eV around the Fermi level with the same accuracy provided by DFT. We also notice that the mixing of two different types of orbital which is at the basis of the model, suggests that $K_2Cr_3As_3$ might actually behave as a two-channel Stoner d-electron metallic magnet [156]. Interestingly, this effect can drive pressure-induced transitions between ferromagnetic and antiferromagnetic ground states.

We also show in Fig. 4.17 the Fermi surface obtained with our minimal model. The Fermi surface is quite similar to the DFT one reported in Refs. [145, 146]. It consists of two quasi-1D sheets formed by the α and β bands and one 3D sheet formed by the γ band. The quasi-1D surfaces are in excellent agreement with the literature, while the 3D surface shows some differences due to the different exchange-correlation

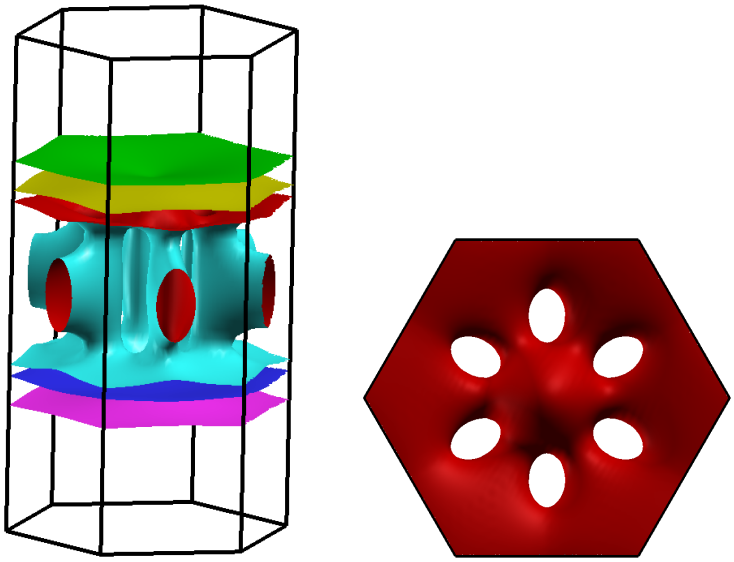

FIGURE 4.17: Fermi surface obtained with our minimal model (left panel) and top view of the 3D surface due to the γ band (right panel).

functional used.

We now derive the analytic expression of our tight-binding model, including in the calculation three NN hopping terms along z, one in the plane and one along the diagonal. We will denote by α_1 and α_2 the Wannier functions relative to the orbitals in the plane at $z = c/2$ with predominant xy and $x^2 - y^2$ character, $c/2$ being the distance between KCr_3As_3 and $K_3Cr_3As_3$ planes, and by α_3, α_4 and α_5 those relative to the orbitals with predominant xy, $x^2 - y^2$ and z^2 character, respectively, in the plane with $z = 0$. We will also denote by $t^{lmn}_{\alpha_i,\alpha_j}$ the hopping amplitudes between the Wannier states α_i and α_j along the direction $\mathrm{l}\mathbf{x} + \mathrm{m}\mathbf{y} + \mathrm{n}\mathbf{z}$. Since the system exhibits inversion symmetry along the z axis and the orbitals under consideration are even, we will get terms proportional to $cos(nk_zc/2)$ for the hopping along z, n being an even (odd) integer for hopping between homologous (different) orbitals.

According to the above assumptions, the Hamiltonian in momentum space is represented as a 5×5 matrix, with elements H_{α_i,α_j}. Concerning the diagonal elements, i.e. those referring to the same Wannier state, they result from the sum of different contributions related to on-site, out-of-plane and in-plane amplitudes, respectively. They thus read as

$$H_{\alpha_i,\alpha_i}(k_x, k_y, k_z) = H^0_{\alpha_i,\alpha_i} + H^{\perp}_{\alpha_i,\alpha_i}(k_z) + H^{\parallel}_{\alpha_i,\alpha_i}(k_x, k_y)$$

	on site	out of plane			in plane	
	000	001	002	003	100	010
α_1	-86.6	154.1	-53.0	-6.3	23.0	-3.5
α_2	-86.6	154.1	-53.0	-6.3	-12.3	14.2
α_3	-37.0	165.0	-41.9	-2.9	30.9	-0.2
α_4	-37.0	165.0	-41.9	-2.9	-10.6	20.6
α_5	0	271.6	-63.9	-14.2	-15.4	-15.4

TABLE 4.1: On-site energies and out-of-plane and in-plane hopping integrals between the same Wannier states. The on-site energy of the z^2-like function is set to zero (energy units in meV).

where

$$\begin{aligned} H^0_{\alpha_i,\alpha_i} &= t^{000}_{\alpha_i,\alpha_i} \equiv \varepsilon^0_{\alpha_i} \\ H^{\perp}_{\alpha_i,\alpha_i}(k_z) &= \sum_{n=1,2,3} 2t^{00n}_{\alpha_i,\alpha_i} \cos(nk_z c) \\ H^{\parallel}_{\alpha_i,\alpha_i}(k_x,k_y) &= 2t^{100}_{\alpha_i,\alpha_i} \cos(k_x a) \\ &\quad + 4t^{010}_{\alpha_i,\alpha_i} \cos(k_x \frac{a}{2}) \cos(k_y a \frac{\sqrt{3}}{2}) \,, \end{aligned}$$

with the numerical values of the hopping parameters being reported in Table 4.1.

Going to the off-diagonal elements connecting different Wannier states, we first observe on a general ground that when a crystal structure exhibits a reflection symmetry with respect to the x axis, one has for pure d-orbitals $t^{100}_{xy,x^2-y^2} = 0$ and $t^{010}_{xy,x^2-y^2} = t^{0\bar{1}0}_{xy,x^2-y^2}$. As regards $K_2Cr_3As_3$, we have that its crystal structure is symmetric with respect to the y-axis, but not with respect to the x-axis. Since the Wannier functions keep this missing symmetry, we have $t^{100}_{\alpha_1,\alpha_2} \neq 0$ and $t^{010}_{\alpha_1,\alpha_2} \neq t^{0\bar{1}0}_{\alpha_1,\alpha_2}$. We stress that in our tight-binding model this effect is explicitly taken into account, differently from previous approaches where the above-mentioned x-axis symmetry is nonetheless applied [119, 151]. As in the previous case, we have that the non-diagonal elements of the Hamiltonian result from in-plane and out-of-plane contributions associated with hopping processes connecting different Wannier states. Their expressions are reported in Appendix C, together with the Tables giving the numerical values of the hopping amplitudes involved.

4.5 Conclusions

We have studied the electronic properties of the quasi-one-dimensional superconductor $K_2Cr_3As_3$, and our results give clear indication that the physics of the system is significantly affected by in-plane dynamics, in spite of the presence in the lattice of well-defined quasi-1D nanotube structures [29, 30]. The results presented here also make evident the minor role played by the local electronic correlations in determining

the physical properties of the compound. Indeed, the inclusion within a LDA+U calculation scheme of a non-vanishing Hubbard repulsion developing in the Cr d-orbitals leads to only slight quantitative differences with respect to the non-interacting case.

A method that combines the Löwdin and the Wannier procedures allowed us to derive a minimal five-band tight-binding model correctly describing the low-energy physics of $K_2Cr_3As_3$ in terms of four planar orbitals (d_{xy} and $d_{x^2-y^2}$ for each of the two planes KCr_3As_3 and $K_3Cr_3As_3$) and a single out-of-plane one (d_{z^2}). We are confident that this combined method can be applied to other transition-metal compounds, including the iron-based superconductors.

We point out that the model may be used to study transport properties, magnetic instabilities, as well as superconductivity in anisotropic crystal structures [157], also allowing to investigate dynamical effects in this class of superconductors [158]. In this case, the evidence that the main features of the energy spectrum around the Fermi level are essentially determined by the three symmetric d_{xy}, $d_{x^2-y^2}$ and d_{z^2} Cr orbitals and by the p_x and p_y As ones, provides a constraint on the form of the superconducting order parameter that should be assumed in the development of the theory.

Chapter 5

Conclusions

In this thesis, the transition metal compounds belonging to the space group Pnma, namely CrAs, MnP and WP, and the quasi-one-dimensional class of materials $A_2Cr_3As_3$, with the element A being K, Rb, Cs or Na have been investigated. These compounds are at the center of today's debate for their many and varied properties, starting from peculiar kind of symmetries and going to the transition from magnetic to superconducting phases. They still need a deep analysis to better understand the interplay between structural, electronic, magnetic and superconducting properties and their connections to the topological features. We have used tight-binding and *ab initio* methods in order to analyze the electronic, magnetic, transport and symmetry features of these materials. This investigation allowed us to do important steps towards the understanding of the role and the position of these compounds in the wider "zoology" of the unconventional superconductors.

Going more specifically, after an introduction in Chapter 1, in Chapter 2 we have used a method that combines the tight-binding approximation and the Löwdin procedure, with the hopping parameters coming from DFT calculations, in order to obtain the low energy band structure, the DOS and the Fermi surface of CrAs. This method allowed us to disentangle the Cr from the As degrees of freedom, in this way we went beyond the *ab initio* calculations that did not allow us to do this. Then we have studied some transport and magnetic properties, taking advantage of the model Hamiltonian thus built up. Finally, the SOC interaction has been considered and we have studied the effects of this on the electronic properties of CrAs.

The band structure of CrAs and of the other compounds belonging to the Pnma space group reflect the symmetries of the crystal and in particular the nonsymmorphic glide and screw symmetries. These involve not only point group operations but also non-primitive lattice translations; the glide consists in a reflection respect to a plane and then a translation along a line parallel to that plane, while the screw is the composition of a rotation about an axis and a translation along this axis. Therefore, in Chapter 3 we analyzed the symmetry properties of these compounds, by using a 2D and then a 3D model Hamiltonian. Particular attention has been given to the recently discovered WP, for what, by using *ab initio* techniques we determined the

structural and the electronic features in absence and presence of SOC. The nonsymmorphic symmetries bring to four- or eight-fold degeneracy of the bands along some high-symmetry lines of the BZ and give rise to some effects on the dimensionality of the Fermi surface. Thus, the role of the nonsymmorphic symmetries on the Fermi surface topology of WP, MnP and CrAs was also investigated and the presence of 2D sheets at some fillings was observed. These 2D sheets could affect the transport and superconducting properties of this class of materials.

In Chapter 4 we have instead studied the quasi-one-dimensional superconductor at ambient pressure $K_2Cr_3As_3$. Also in this case we have used a tight-binding Hamiltonian in which the hopping parameters come from DFT calculations and we have discovered the importance of the in-plane dynamics in the electronic structure, in spite of the presence in the lattice of well-defined quasi-1D nanotube structures. This led us to highlight some differences of this material from other Q1D compounds. Then, by using a combination of Wannier and Löwdin procedure we obtained a minimal five-band model correctly describing the low-energy physics of $K_2Cr_3As_3$ in terms of four planar orbitals (d_{xy} and $d_{x^2-y^2}$ for each of the two planes KCr_3As_3 and $K_3Cr_3As_3$) and a single out-of-plane one (d_{z^2}). This model may be used to study transport properties, magnetic instabilities, as well as superconductivity in anisotropic crystal structures, also allowing to investigate dynamical effects in this class of superconductors.

Many questions are still open for further investigation of these compounds, from the the symmetry and the microscopic origin of the superconducting pairing still under debate to the complex topological features. Future developments of this work are the analysis of the effects of the nonsymmorphic symmetries on the magnetic and superconducting properties in transition metal pnictides of the Pnma space group and the investigation of the topological, magnetic and superconducting features in the $A_2Cr_3As_3$ materials.

Regarding the Pnma transition metal pnictides, one direct consequence of the multifold degeneracy is that there are peaks in the DOS, close to the crossing points, which naturally lead, in the presence of interaction, to a tendency to get a Stoner-like instability. Other than this, the degeneracy of the bands, the new symmetries in presence of magnetic interactions and the possible nesting effects, due to the presence of two-dimensional Fermi surfaces which implies density wave instabilities can be analyzed. The nonsymmorphic symmetries can lead to predictions about the nature of the superconducting pairing and the emergence of non-trivial topological superconductivity. Daido et al. [27] proposed that MnP-compounds like CrAs and UCoGe can be topological nonsymmorphic crystalline superconductors and some of these can be classified in $\mathbb{Z}_4$ topological phases. Furthermore, one can also expect that in these compounds a high-spin pairing can be realized, in analogy to the unconventional superconductivity proposed in Refs.[130, 131]. Since the onsets of the superconductivity

are close to phase transitions, that break the symmetries according to the Landau theory, the superconductivity could be studied when there is a small perturbation that slightly breaks the nonsymmorphic symmetry.

This analysis can be extended to non magnetic transition metal oxides belonging to the same space group like $SrIrO_3$, $CaIrO_3$ and $CaRuO_3$.

The resistance of the WP follows the behavior of the Bloch-Grüneisen $\sim T^5$, therefore we can assume that in CrAs the different behavior of the Bloch-Grüneisen [49] is due to a strong magnon-phonon interaction. We should also study how this strong magnon-phonon interaction influences the superconductivity of CrAs.

For the $K_2Cr_3As_3$ compund, Taddei et al. [148] found significant phonon instability, which corresponds to a frustrated orthorhombic distortion. They found that the Cr-triangles in the double walled subnanotubes are no longer equilateral, this could lead to an absence of frustration. These results suggest a more complex phase diagram with subtle interplay of structural, electron-phonon and magnetic interactions. Therefore it is really important to study the properties of these compounds in the case of the distortions predicted by Taddei et al. [148], especially regarding to the magnetism and its connection with the topological features. We also point out that, with a filling of four electrons shared among two kinds of orbitals, the planar d_{xy} and $d_{x^2-y^2}$ and the out-of-plane d_{z^2} ones, the $K_2Cr_3As_3$ might be in the Hund's metal regime. In this framework, it has been proposed that Hund's coupling may lead to an orbital decoupling that makes the orbitals independent from each other, so that some of them can acquire a remarkably larger mass enhancement with respect to the other ones. Furthermore, a possible connection between the orbital selective correlations and superconductivity might be investigated: the selective correlations could be the source of the pairing glue or, alternatively, could strengthen the superconducting instability arising from a more conventional mechanism based on the exchange of bosons or spin fluctuations.

The centrality of these topics in contemporary condensed matter physics is testified by the continuous discoveries in this field. For example in this year the superconductivity in chromium nitrides $Pr_3Cr_{10-x}N_{11}$ has been reported by Wu et al. [159], the superconductivity in Al-doped CrAs has been investigated [34] and interesting studies on topology in $A_2Cr_3As_3$ have been done [160, 161].

Acknowledgements

First of all, I immensely thank Prof. Canio Noce, already Supervisor of my Bachelor and Master Theses, for all the scientific and ethical teachings, for his constant presence, his affection and for believing in me. I thank him for giving me the opportunity to work with him and his research group in projects of great scientific relevance. He has been my point of reference during all these years, starting from the third year of my university studies.

I really thank Dr. Carmine Autieri, already Co-Supervisor of my Master Thesis, for following me on this long way, for being always present even from a distance. I thank him for teaching me many computational techniques and important methods in the field of solid state physics and for being a fundamental reference during my period in Warsaw not only from a scientific but also a human point of view.

I want to thank all the members of the research group; I had the honor of collaborating with them and I learned a lot. In particular, I would like to thank Dr. Mario Cuoco and Dr. Filomena Forte; they gave me part of their great experience and taught me to take care of every detail of the scientific work. Special thanks to Prof. Adolfo Avella, Dr. Maria Teresa Mercaldo and Prof. Alfonso Romano for their great availability, the valuable suggestions and discussions about the quasi-one-dimensional superconductor $K_2Cr_3As_3$. I also want to thank the PhD Coordinator Prof. Carmine Attanasio for all the time he has devoted to all of us PhD students with great attention and sympathy.

I thank the whole research team of the International Research Centre Magtop, Institute of Physics, Polish Academy of Sciences of Warsaw, in particular Prof. Tomasz Dietl for welcoming me and giving me the opportunity to collaborate with his research team. I also thank Dr. Victor Fernandez Becerra and Dr. Marcin Wysokinski for the stimulating discussions.

I thank K. Sen for the Fig. 2.17 and for the useful discussions.

A big thank you to my friends and collegues of Salerno: Alfonso, Luciano, Luca, Alex, Onofrio, Gianpaolo, Gaetano and Giuseppe. I felt their affection and support at all times, they allowed me to work in a peaceful and cheerful environment. Another big thank you to my friends and collegues of Warsaw: Rajibul, Tania, Nguyen, Konrad, Saeed, Ashutosh and Pradosh. They made me feel at home, with them I shared beautiful moments.

Finally, I thank my family and friends who have always been close to me.

Appendix A

p-d hybridization and oxidation state of transition metal pnictides

A.1 p-d hybridization

Here we examine a p-d toy model, in order to demonstrate that it is not possible to reduce to a simple minimal model for the entire subset of d-bands close to the Fermi level. We start by considering three d and two p bands, where the p-bands have a large dispersion, while the d-bands are flat in the region between -0.1 and 0.1 eV. In Fig. A.1 we show the case in which the hybridization between the d- and p-orbitals is turned off, while in Fig. A.2 we plot the band structure when the hybridization is switched on. From an inspection to these figures, we conclude that one can distinguish the different contribution of the orbitals to the bands in the first case, whereas the same bands are strongly entangled when the d-p hybridization is switched on.

This simple example shows that we cannot obtain an accurate minimal model for all three d-bands. When the p-d hybridization is larger than the difference between the on-site energies of the p- and d-states, the d- and p-manifolds cannot be disentangled. However, an effective minimal model can be achieved by limiting to the single d-band crossing the Fermi level, as we can see in Fig. A.2. The possibility describe the band structure close to the Fermi level in terms of a minimal set of bands having mainly d character has been demonstrated in other transition metal pnictides. We also point out that, when magnetic properties are concerned, the strong hybridizations requires the p-channel to be included, like in the Anderson model [162, 163], thus allowing for a correct interpretation of the magnetism for this class of compounds [156].

The impossibility to decouple the p-bands from the d-bands depends on the covalence and electronegativity of CrAs, WP and MnP not on the group symmetry. Indeed, in other Pnma structure like the perovskite oxide ABO_3, it is straightforward to decouple the low energy d-bands from all the other bands [164].

A.2 Oxidation state

The oxidation state of CrAs and WP is predominantly 0, while in MnP the oxidation state is more subtle. Indeed, if the oxidation state of Mn had been zero, then Mn

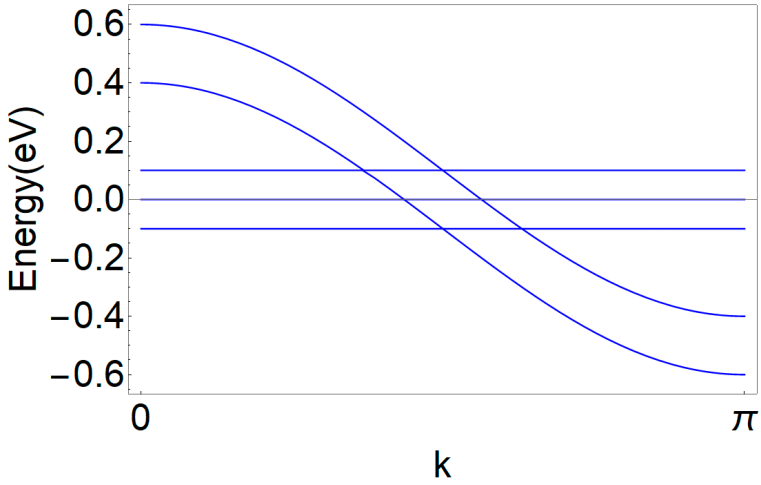

FIGURE A.1: Band structure of three flat d-bands and two wide p-bands when the d-p hybridization is turned off. The Fermi level is set at zero energy.

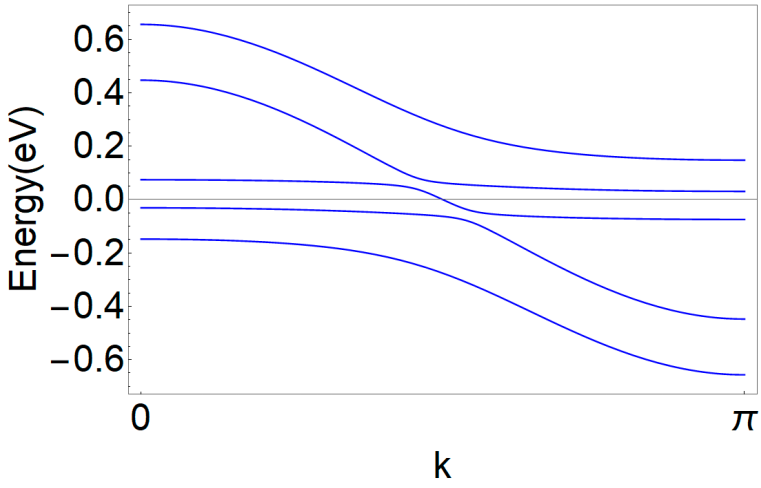

FIGURE A.2: Band structure of three flat d-bands and two wide p-bands when the d-p hybridization is switched on. The Fermi level is set at zero energy.

would have been in $3d^7$ configuration with a maximum magnetic moment of 3 μ_B. However, with GGA+U calculations [165] and at high volumes [65], we can see that the magnetization exceeds 3 μ_B per Mn atom. Therefore, the Mn oxidation state cannot be zero for the metallic MnP compound. We have calculated the oxidation for the non magnetic case obtaining +0.6 for the Mn and -0.6 for the P. This suggests that also the oxidation state of the Cr can be of the order of +0.6 or +1 in CrP.

Appendix B

Minimal tight-binding model for MnP-type compounds

Here we report the values of the parameters of our tight binding minimal model, in which we have included three NN hopping terms along x, y and z direction, one in the plane and two along the diagonal, and whose expression is the same reported in Chapter 3 Sec 3.3.

In Table B.1, we report the values of the hopping parameters obtained by fitting.

TABLE B.1: Values of the hopping parameters of our tight-binding minimal model.

Parameters	**Values**
ε_0	-0.33842
t_{AA}^{100}	-0.28409
t_{AA}^{200}	0.00975
t_{AA}^{300}	-0.00395
t_{AA}^{010}	-0.19479
t_{AA}^{020}	0.08098
t_{AA}^{030}	-0.05264
t_{AA}^{001}	0.04979
t_{AA}^{002}	-0.03154
t_{AA}^{003}	0.00419
t_{AB}^{100}	0.08162
t_{AC}^{001}	0.00074
t_{AC}^{001}	0.31910

In Figs. B.1 and B.2 we show the fit of the DFT bands using our tight-binding minimal model along the high-symmetry path of the orthorhombic Brillouin zone. As we can see, we well describe the bands around the S and R points, thus reconstructing the 2D sheets of the FS.

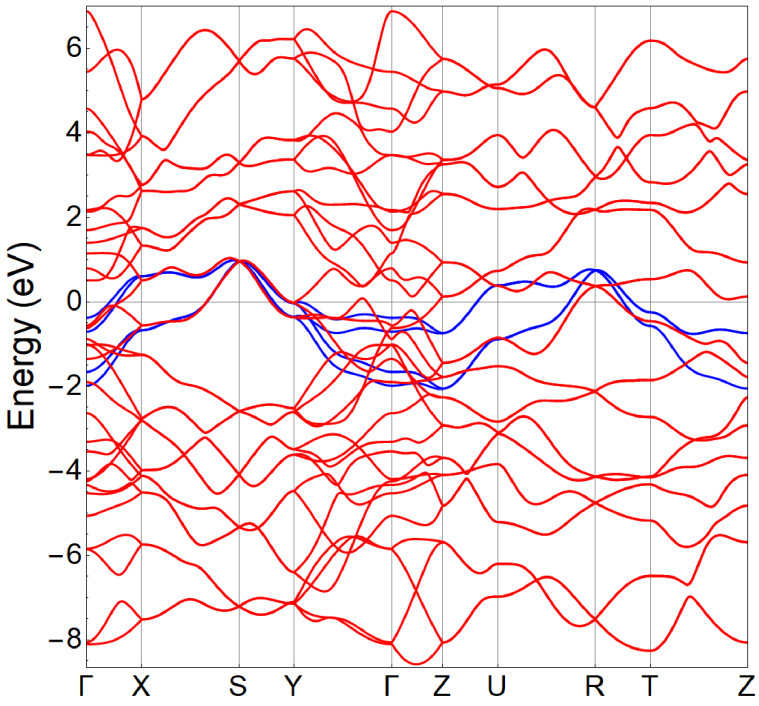

FIGURE B.1: Fit of the DFT bands (red lines) using our tight-binding model (blue lines) along the high-symmetry path of the orthorhombic Brillouin zone. The Fermi level is set at zero energy.

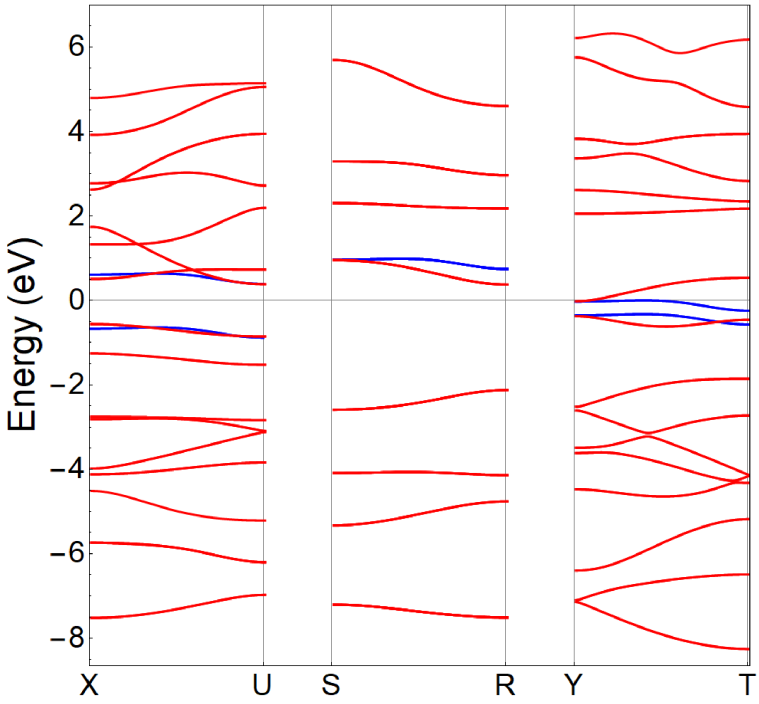

FIGURE B.2: Fit of the DFT bands (red lines) using our tight-binding model (blue lines) along the remaining high-symmetry lines of the orthorhombic Brillouin zone. The Fermi level is set at zero energy.

Appendix C

Off diagonal elements of the minimal model for $K_2Cr_3As_3$

We report here the expressions of the off-diagonal elements $H_{\alpha_i,\alpha_j}(k_x,k_y,k_z)$ $(\alpha_i \neq \alpha_j)$ of the tight-binding Hamiltonian introduced in Chapter 4 Sec. 4.3. They refer to hopping processes which connects different Wannier states and have the following form:

$$
\begin{aligned}
H_{\alpha_1,\alpha_3} &= \sum_{n=0,1,2} 2t^{00n+\frac{1}{2}}_{\alpha_1,\alpha_3}\cos\left((n+\frac{1}{2})k_zc\right) \\
&+4t^{100}_{\alpha_1,\alpha_3}\cos\left(k_xa\right)\cos\left(k_zc/2\right) \\
&+4t^{010}_{\alpha_1,\alpha_3}e^{i(k_ya\frac{\sqrt{3}}{2})}\cos\left(k_xa/2\right)\cos\left(k_zc/2\right) \\
&+4t^{0\bar{1}0}_{\alpha_1,\alpha_3}e^{-i(k_ya\frac{\sqrt{3}}{2})}\cos\left(k_xa/2\right)\cos\left(k_zc/2\right) \\
H_{\alpha_2,\alpha_4} &= \sum_{n=0,1,2} 2t^{00n+\frac{1}{2}}_{\alpha_2,\alpha_4}\cos\left((n+\frac{1}{2})k_zc\right) \\
&+4t^{100}_{\alpha_2,\alpha_4}\cos\left(k_xa\right)\cos\left(k_zc/2\right) \\
&+4t^{010}_{\alpha_2,\alpha_4}e^{i(k_ya\frac{\sqrt{3}}{2})}\cos\left(k_xa/2\right)\cos\left(k_zc/2\right) \\
&+4t^{0\bar{1}0}_{\alpha_2,\alpha_4}e^{-i(k_ya\frac{\sqrt{3}}{2})}\cos\left(k_xa/2\right)\cos\left(k_zc/2\right) \\
H_{\alpha_1,\alpha_2} &= 2it^{100}_{\alpha_1,\alpha_2}\sin\left(k_xa\right)+2it^{010}_{\alpha_1,\alpha_2}e^{i(k_ya\frac{\sqrt{3}}{2})}\sin\left(k_xa/2\right) \\
&+2it^{0\bar{1}0}_{\alpha_1,\alpha_2}e^{-i(k_ya\frac{\sqrt{3}}{2})}\sin\left(k_xa/2\right) \\
H_{\alpha_1,\alpha_4} &= 4it^{100}_{\alpha_1,\alpha_4}\sin\left(k_xa\right)\cos\left(k_zc/2\right) \\
&+4it^{010}_{\alpha_1,\alpha_4}e^{i(k_ya\frac{\sqrt{3}}{2})}\sin\left(k_xa/2\right)\cos\left(k_zc/2\right) \\
&+4it^{0\bar{1}0}_{\alpha_1,\alpha_4}e^{-i(k_ya\frac{\sqrt{3}}{2})}\sin\left(k_xa/2\right)\cos\left(k_zc/2\right)
\end{aligned}
$$

	out of plane			in plane		
	001	002	003	100	010	$0\bar{1}0$
$\alpha_1\alpha_3$	7.9	7.3	14.6	-7.4	-6.9	1.4
$\alpha_2\alpha_4$	7.9	7.3	14.6	-1.2	-1.7	-9.9

TABLE C.1: Hopping integrals between α_1-α_3 and α_2-α_4 Wannier states (energy units in meV).

$$
\begin{aligned}
H_{\alpha_1,\alpha_5} &= 4it^{100}_{\alpha_1,\alpha_5}\sin(k_xa)\cos(k_zc/2) \\
&\quad +4it^{010}_{\alpha_1,\alpha_5}e^{i(k_ya\frac{\sqrt{3}}{2})}\sin(k_xa/2)\cos(k_zc/2) \\
&\quad +4it^{0\bar{1}0}_{\alpha_1,\alpha_5}e^{-i(k_ya\frac{\sqrt{3}}{2})}\sin(k_xa/2)\cos(k_zc/2) \\
H_{\alpha_2,\alpha_3} &= 4it^{100}_{\alpha_2,\alpha_3}\sin(k_xa)\cos(k_zc/2) \\
&\quad +4it^{010}_{\alpha_2,\alpha_3}e^{i(k_ya\frac{\sqrt{3}}{2})}\sin(k_xa/2)\cos(k_zc/2) \\
&\quad +4it^{0\bar{1}0}_{\alpha_2,\alpha_3}e^{-i(k_ya\frac{\sqrt{3}}{2})}\sin(k_xa/2)\cos(k_zc/2) \\
H_{\alpha_2,\alpha_5} &= 4t^{100}_{\alpha_2,\alpha_5}\cos(k_xa)\cos(k_zc/2) \\
&\quad +4t^{010}_{\alpha_2,\alpha_5}e^{i(k_ya\frac{\sqrt{3}}{2})}\cos(k_xa/2)\cos(k_zc/2) \\
&\quad +4t^{0\bar{1}0}_{\alpha_2,\alpha_5}e^{-i(k_ya\frac{\sqrt{3}}{2})}\cos(k_xa/2)\cos(k_zc/2) \\
H_{\alpha_3,\alpha_4} &= 2it^{100}_{\alpha_3,\alpha_4}\sin(k_xa)+2it^{010}_{\alpha_3,\alpha_4}e^{i(k_ya\frac{\sqrt{3}}{2})}\sin(k_xa/2) \\
&\quad +2it^{0\bar{1}0}_{\alpha_3,\alpha_4}e^{-i(k_ya\frac{\sqrt{3}}{2})}\sin(k_xa/2) \\
H_{\alpha_3,\alpha_5} &= 2it^{100}_{\alpha_3,\alpha_5}\sin(k_xa)+2it^{010}_{\alpha_3,\alpha_5}e^{i(k_ya\frac{\sqrt{3}}{2})}\sin(k_xa/2) \\
&\quad +2it^{0\bar{1}0}_{\alpha_3,\alpha_5}e^{-i(k_ya\frac{\sqrt{3}}{2})}\sin(k_xa/2) \\
H_{\alpha_4,\alpha_5} &= 2t^{100}_{\alpha_4,\alpha_5}\cos(k_xa)+2t^{010}_{\alpha_4,\alpha_5}e^{i(k_ya\frac{\sqrt{3}}{2})}\cos(k_xa/2) \\
&\quad +2t^{0\bar{1}0}_{\alpha_4,\alpha_5}e^{-i(k_ya\frac{\sqrt{3}}{2})}\cos(k_xa/2)
\end{aligned}
$$

The numerical values of the hopping parameters in the above expressions are reported in Tables C.1 and C.2. In particular we see from Table C.2 that the most relevant hopping amplitudes, larger than 30 meV, occur between the planar α_1 and α_2 and between the planar α_3 and α_4 Wannier states in the xy plane.

	100	010	$0\bar{1}0$
$\alpha_1\alpha_2$	-15.0	30.3	-0.2
$\alpha_1\alpha_4$	-7.1	-2.7	2.6
$\alpha_1\alpha_5$	-9.1	-8.6	-0.5
$\alpha_2\alpha_3$	-2.4	-7.3	-2.1
$\alpha_2\alpha_5$	-4.7	-5.6	10.2
$\alpha_3\alpha_4$	17.4	0.6	-35.4
$\alpha_3\alpha_5$	13.0	-1.0	14.1
$\alpha_4\alpha_5$	-8.7	15.7	-6.9

TABLE C.2: Hopping integrals between different Wannier states, other than those listed in Table II (energy units in meV).

Bibliography

[1] R. Movshovich, M. Jaime, J. D. Thompson, C. Petrovic, Z. Fisk, P. G. Pagliuso, and J. L. Sarrao, Phys. Rev. Lett. **86**, 5152–5155 (2001).

[2] D. J. Van Harlingen, Rev. Mod. Phys. **67**, 515–535 (1995).

[3] A. P. Mackenzie and Y. Maeno, Rev. Mod. Phys. **75**, 657–712 (2003).

[4] I. I. Mazin, D. J. Singh, M. D. Johannes, and M. H. Du, Phys. Rev. Lett. **101**, 057003 (2008).

[5] G. Goll, Springer Tracts in Modern Physics (Springer, 2006).

[6] R. Y. Chen and N. L. Wang, Reports on Progress in Physics **82**, 012503 (2018).

[7] W. Wu, X. Zhang, Z. Yin, P. Zheng, N. Wang, and J. Luo, Science China Physics, Mechanics and Astronomy **53**, 1207–1211 (2010).

[8] W. Wu, J. Cheng, K. Matsubayashi, P. Kong, F. Lin, C. Jin, N. Wang, Y. Uwatoko, and J. Luo, Nature Communications **5**, 5508 (2014).

[9] H. Kotegawa, S. Nakahara, H. Tou, and H. Sugawara, Journal of the Physical Society of Japan **83**, 093702 (2014).

[10] M. R. Norman, Science **332**, 196–200 (2011).

[11] J.-G. Cheng, K. Matsubayashi, W. Wu, J. P. Sun, F. K. Lin, J. L. Luo, and Y. Uwatoko, Phys. Rev. Lett. **114**, 117001 (2015).

[12] Z. Liu, W. Wu, Z. Zhao, H. Zhao, J. Cui, P. Shan, J. Zhang, C. Yang, P. Sun, Y. Wei, S. Li, J. Zhao, Y. Sui, J. Cheng, L. Lu, J. Luo, and G. Liu, Phys. Rev. B **99**, 184509 (2019).

[13] Q.-G. Mu, B.-B. Ruan, B.-J. Pan, T. Liu, J. Yu, K. Zhao, G.-F. Chen, and Z.-A. Ren, Phys. Rev. Materials **2**, 034803 (2018).

[14] J.-K. Bao, J.-Y. Liu, C.-W. Ma, Z.-H. Meng, Z.-T. Tang, Y.-L. Sun, H.-F. Zhai, H. Jiang, H. Bai, C.-M. Feng, Z.-A. Xu, and G.-H. Cao, Phys. Rev. X **5**, 011013 (2015).

[15] Z.-T. Tang, J.-K. Bao, Y. Liu, Y.-L. Sun, A. Ablimit, H.-F. Zhai, H. Jiang, C.-M. Feng, Z.-A. Xu, and G.-H. Cao, Phys. Rev. B **91**, 020506 (2015).

[16] Z.-T. Tang, J.-K. Bao, Z. Wang, H. Bai, H. Jiang, Y. Liu, H.-F. Zhai, C.-M. Feng, Z.-A. Xu, and G.-H. Cao, Science China Materials **58**, 16–20 (2015).

[17] R. Peierls, *Quantum theory of solids* (Oxford University Press, London, 1955).

[18] S. van Smaalen, Acta Crystallographica Section A **61**, 51–61 (2005).

[19] J Voit, Reports on Progress in Physics **58**, 977–1116 (1995).

[20] C. Autieri and C. Noce, Philosophical Magazine **97**, 3276–3295 (2017).

[21] C. Autieri, G. Cuono, F. Forte, and C. Noce, Journal of Physics: Condensed Matter **29**, 224004 (2017).

[22] O. Andersen, A. Liechtenstein, O. Jepsen, and F. Paulsen, Journal of Physics and Chemistry of Solids **56**, Proceedings of the Conference on Spectroscopies in Novel Superconductors, 1573 –1591 (1995).

[23] C. Noce and M. Cuoco, Phys. Rev. B **59**, 2659–2666 (1999).

[24] C. Autieri, G. Cuono, F. Forte, and C. Noce, Journal of Physics: Conference Series **969**, 012106 (2018).

[25] G. Cuono, C. Autieri, G. Guarnaccia, A. Avella, M. Cuoco, F. Forte, and C. Noce, Eur. Phys. J. Special Topics **228**, 631–641 (2019).

[26] Q. Niu, W. C. Yu, K. Y. Yip, Z. L. Lim, H. Kotegawa, E. Matsuoka, H. Sugawara, H. Tou, Y. Yanase, and S. K. Goh, Nat. Commun. **8**, 15358 (2017).

[27] A. Daido, T. Yoshida, and Y. Yanase, Phys. Rev. Lett. **122**, 227001 (2019).

[28] G. Cuono, F. Forte, M. Cuoco, R. Islam, J. Luo, C. Noce, and C. Autieri, Phys. Rev. Materials **3**, 095004 (2019).

[29] G. Cuono, C. Autieri, F. Forte, G. Busiello, M. T. Mercaldo, A. Romano, C. Noce, and A. Avella, AIP Advances **8**, 101312 (2018).

[30] G. Cuono, C. Autieri, F. Forte, M. T. Mercaldo, A. Romano, A. Avella, and C. Noce, New Journal of Physics **21**, 063027 (2019).

[31] L. Keller, J. S. White, M. Frontzek, P. Babkevich, M. A. Susner, Z. C. Sims, A. S. Sefat, H. M. Rønnow, and C. Rüegg, Phys. Rev. B **91**, 020409 (2015).

[32] Y. Shen, Q. Wang, Y. Hao, B. Pan, Y. Feng, Q. Huang, L. W. Harriger, J. B. Leao, Y. Zhao, R. M. Chisnell, J. W. Lynn, H. Cao, J. Hu, and J. Zhao, Phys. Rev. B **93**, 060503 (2016).

[33] M. Matsuda, F. K. Lin, R. Yu, J.-G. Cheng, W. Wu, J. P. Sun, J. H. Zhang, P. J. Sun, K. Matsubayashi, T. Miyake, T. Kato, J.-Q. Yan, M. B. Stone, Q. Si, J. L. Luo, and Y. Uwatoko, Phys. Rev. X **8**, 031017 (2018).

[34] S. Park, S. Shin, S.-I. Kim, S. Kim, C. K. Park, J. D. Thompson, and T. Park, npj Quantum Materials **4**, 49 (2019).

[35] C. M. Varma, Phys. Rev. Lett. **83**, 3538–3541 (1999).

[36] C. Noce, G. Busiello, and M. Cuoco, Europhys. Lett. **51**, 195–201 (2000).

[37] C. Noce, A. Vecchione, M. Cuoco, and A. Romano, *Ruthenate and rutheno-cuprate materials : unconventional superconductivity, magnetism and quantum phase transitions* (Springer, 2002).

[38]D. van der Marel, H. J. A. Molegraaf, J. Zaanen, Z. Nussinov, F. Carbone, A. Damascelli, H. Eisaki, M. Greven, P. H. Kes, and M. Li, npj Quantum Materials **425**, 271–274 (2003).

[39]S. Jiang, H. Xing, G. Xuan, C. Wang, Z. Ren, C. Feng, J. Dai, Z. Xu, and G. Cao, Journal of Physics: Condensed Matter **21**, 382203 (2009).

[40]T. Shibauchi, A. Carrington, and Y. Matsuda, Annual Review of Condensed Matter Physics **5**, 113–135 (2014).

[41]S. Seo, E. Park, E. D. Bauer, F. Ronning, J. N. Kim, J.-H. Shim, J. D. Thompson, and T. Park, Nat. Commun. **6**, 6433 (2015).

[42]H. Kotegawa, S. Nakahara, R. Akamatsu, H. Tou, H. Sugawara, and H. Harima, Phys. Rev. Lett. **114**, 117002 (2015).

[43]R. Khasanov, Z. Guguchia, I. Eremin, H. Luetkens, A. Amato, P. K. Biswas, C. Ruegg, M. A. Susner, Z. N. D. Sefat A. S., and E. Morenzoni, Sci. Rep. **5**, 13788 (2015).

[44]C. Y. Guo, M. Smidman, B. Shen, W. Wu, F. K. Lin, X. L. Han, Y. Chen, F. Wu, Y. F. Wang, W. B. Jiang, X. Lu, J. P. Hu, J. L. Luo, and H. Q. Yuan, Phys. Rev. B **98**, 024520 (2018).

[45]K. Kadowaki and S. B. Woods, Solide State Commun. **58**, 507–509 (1986).

[46]M. Cuoco, F. Forte, and C. Noce, Phys. Rev. B **74**, 195124 (2006).

[47]M. Cuoco, F. Forte, and C. Noce, Phys. Rev. B **73**, 094428 (2006).

[48]F. Forte, M. Cuoco, and C. Noce, Phys. Rev. B **82**, 155104 (2010).

[49]A. Nigro, P. Marra, C. Autieri, W. Wu, J. Cheng, J. Luo, and C. Noce, EPL **125**, 57002 (2019).

[50]G. Kresse and J. Hafner, Phys. Rev. B **47**, 558–561 (1993).

[51]G. Kresse and J. Hafner, Phys. Rev. B **49**, 14251–14269 (1994).

[52]G. Kresse and J. Furthmüller, Phys. Rev. B **54**, 11169–11186 (1996).

[53]G. Kresse and J. Furthmüller, Computational Materials Science **6**, 15 –50 (1996).

[54]G. Kresse and D. Joubert, Phys. Rev. B **59**, 1758–1775 (1999).

[55]J. P. Perdew and A. Zunger, Phys. Rev. B **23**, 5048–5079 (1981).

[56]D. M. Ceperley and B. J. Alder, Phys. Rev. Lett. **45**, 566–569 (1980).

[57]N. Marzari and D. Vanderbilt, Phys. Rev. B **56**, 12847–12865 (1997).

[58]I. Souza, N. Marzari, and D. Vanderbilt, Phys. Rev. B **65**, 035109 (2001).

[59]A. A. Mostofi, J. R. Yates, Y.-S. Lee, I. Souza, D. Vanderbilt, and N. Marzari, Computer Physics Communications **178**, 685 –699 (2008).

[60]W. Setyawan and S. Curtarolo, Computational Materials Science **49**, 299 –312 (2010).

[61] C. Autieri, E. Koch, and E. Pavarini, Phys. Rev. B **89**, 155109 (2014).

[62] O. Löwdin P., J. Chem. Phys. **18**, 365 (1950).

[63] J. M. Ziman, *Principles of the theory of solids* (Cambridge: Cambridge University Press, 1979).

[64] C. Noce and M. Cuoco, Phys. Rev. B **62**, 9884–9887 (2000).

[65] Z. Gercsi and K. G. Sandeman, Phys. Rev. B **81**, 224426 (2010).

[66] C. Autieri, M. Cuoco, and C. Noce, Phys. Rev. B **85**, 075126 (2012).

[67] H. Xiang, C. Lee, H.-J. Koo, X. Gong, and M.-H. Whangbo, Dalton Trans. **42**, 823–853 (2013).

[68] B Skubic, J Hellsvik, L Nordström, and O Eriksson, Journal of Physics: Condensed Matter **20**, 315203 (2008).

[69] K. Sen, Y. Yao, R. Heid, A. Omoumi, F. Hardy, K. Willa, M. Merz, A. A. Haghighirad, and M. Le Tacon, Phys. Rev. B **100**, 104301 (2019).

[70] Y. Wang, Y. Feng, C. J.-G., W. Wu, J. L. Luo, and T. F. Rosenbaum, Nat. Commun. **7**, 13037 (2016).

[71] S Toth and B Lake, Journal of Physics: Condensed Matter **27**, 166002 (2015).

[72] J. Friedel, P. Lenglart, and G. Leman, Journal of Physics and Chemistry of Solids **25**, 781 –800 (1964).

[73] M. Konig, S. Wiedmann, C. Brune, A. Roth, H. Buhmann, L. W. Molenkamp, X. L. Qi, and S. C. Zhang, Science **318**, 766 (2007).

[74] D. Hsieh, D. Qian, L. Wray, Y. Xia, Y. S. Hor, R. J. Cava, and M. Z. Hasan, Nature **452**, 970–974 (2008).

[75] M. Z. Hasan and C. L. Kane, Rev. Mod. Phys. **82**, 3045–3067 (2010).

[76] X.-L. Qi and S.-C. Zhang, Rev. Mod. Phys. **83**, 1057–1110 (2011).

[77] M. Z. Hasan and J. E. Moore, Annual Review of Condensed Matter Physics **2**, 55–78 (2011).

[78] A. P. Schnyder and P. M. R. Brydon, Journal of Physics: Condensed Matter **27**, 243201 (2015).

[79] T. Senthil, Annual Review of Condensed Matter Physics **6**, 299–324 (2015).

[80] C.-K. Chiu, H. Yao, and S. Ryu, Phys. Rev. B **88**, 075142 (2013).

[81] C.-K. Chiu and A. P. Schnyder, Phys. Rev. B **90**, 205136 (2014).

[82] C.-K. Chiu, J. C. Y. Teo, A. P. Schnyder, and S. Ryu, Rev. Mod. Phys. **88**, 035005 (2016).

[83] Y. Ando and L. Fu, Annual Review of Condensed Matter Physics **6**, 361–381 (2015).

[84] K. Shiozaki and M. Sato, Phys. Rev. B **90**, 165114 (2014).

[85] T. Morimoto and A. Furusaki, Phys. Rev. B **88**, 125129 (2013).

[86]Y.-H. Chan, C.-K. Chiu, M. Y. Chou, and A. P. Schnyder, Phys. Rev. B **93**, 205132 (2016).

[87]Y. X. Zhao, A. P. Schnyder, and Z. D. Wang, Phys. Rev. Lett. **116**, 156402 (2016).

[88]W. Brzezicki, M. M. Wysokinski, and T. Hyart, Phys. Rev. B **100**, 121107 (2019).

[89]D. J. Groenendijk, C. Autieri, T. C. van Thiel, W. Brzezicki, N. Gauquelin, P. Barone, K. H. W. van den Bos, S. van Aert, J. Verbeeck, A. Filippetti, S. Picozzi, M. Cuoco, and A. D. Caviglia, arXiv:1810.05619 (2018).

[90]J. Kruthoff, J. de Boer, J. van Wezel, C. L. Kane, and R.-J. Slager, Phys. Rev. X **7**, 041069 (2017).

[91]R.-J. Slager, A. Mesaros, V. Juricic, and J. Zaanen, Nat. Phys. **9**, 98–102 (2013).

[92]A. Bouhon, A. M. Black-Schaffer, and R.-J. Slager, arXiv:1804.09719 (2018).

[93]R. Takahashi, M. Hirayama, and S. Murakami, Phys. Rev. B **96**, 155206 (2017).

[94]T. Wehling, A. Black-Schaffer, and A. Balatsky, Advances in Physics **63**, 1–76 (2014).

[95]N. P. Armitage, E. J. Mele, and A. Vishwanath, Rev. Mod. Phys. **90**, 015001 (2018).

[96]S. M. Young, S. Zaheer, J. C. Y. Teo, C. L. Kane, E. J. Mele, and A. M. Rappe, Phys. Rev. Lett. **108**, 140405 (2012).

[97]H. Weng, C. Fang, Z. Fang, B. A. Bernevig, and X. Dai, Phys. Rev. X **5**, 011029 (2015).

[98]P. Horava, Phys. Rev. Lett. **95**, 016405 (2005).

[99]T. T. Heikkilä and G. E. Volovik, JETP Letters **93**, 59–65 (2011).

[100]A. A. Burkov, M. D. Hook, and L. Balents, Phys. Rev. B **84**, 235126 (2011).

[101]A. A. Soluyanov, D. Gresch, Z. Wang, Q. Wu, M. Troyer, X. Dai, and B. A. Bernevig, Nature **526**, 495 (2015).

[102]B. Bradlyn, J. Cano, Z. Wang, M. G. Vergniory, C. Felser, R. Cava, and B. Bernevig, Science **353**, 5037 (2016).

[103]Y. X. Zhao and A. P. Schnyder, Phys. Rev. B **94**, 195109 (2016).

[104]T. Bzdusek, Q. Wu, A. Ruegg, M. Sigrist, and A. A. Soluyanov, Nature **538**, 75–78 (2016).

[105]Z. Wang, A. Alexandradinata, R. J. Cava, and B. A. Bernevig, Nature **532**, 189 (2016).

[106]L. Lu, C. Fang, L. Fu, S. G. Johnson, J. D. Joannopoulos, and M. Soljacic, Nat. Phys. **12**, 337 (2016).

[107]S. A. Parameswaran, A. M. Turner, D. P. Arovas, and A. Vishwanath, Nat. Phys. **9**, 299 (2013).

[108]L. Michel and J. Zak, Physics Reports **341**, 377 –395 (2001).

[109] A. König and N. D. Mermin, Phys. Rev. B **56**, 13607–13610 (1997).

[110] H. Watanabe, H. C. Po, M. P. Zaletel, and A. Vishwanath, Phys. Rev. Lett. **117**, 096404 (2016).

[111] B. Singh, B. Ghosh, C. Su, H. Lin, A. Agarwal, and A. Bansil, Phys. Rev. Lett. **121**, 226401 (2018).

[112] H. Weng, X. Dai, and Z. Fang, J. Phys.: Cond. Mat. **28**, 30 (2016).

[113] B. J. Wieder and C. L. Kane, Phys. Rev. B **94**, 155108 (2016).

[114] W. Brzezicki and M. Cuoco, Phys. Rev. B **95**, 155108 (2017).

[115] T. Yoshida, A. Daido, N. Kawakami, and Y. Yanase, Phys. Rev. B **99**, 235105 (2019).

[116] J. Feng, Y. Pang, D. Wu, Z. Wang, H. Weng, J. Li, X. Dai, Z. Fang, Y. Shi, and L. Lu, Phys. Rev. B **92**, 081306 (2015).

[117] T. Liang, Q. Gibson, M. N. Ali, M. Liu, R. J. Cava, and N. P. Ong, Nat. Mater. **14**, 280–284 (2015).

[118] A. Narayanan, M. D. Watson, S. F. Blake, N. Bruyant, L. Drigo, Y. L. Chen, D. Prabhakaran, B. Yan, C. Felser, T. Kong, P. C. Canfield, and A. I. Coldea, Phys. Rev. Lett. **114**, 117201 (2015).

[119] X. Wu, F. Yang, C. Le, H. Fan, and J. Hu, Phys. Rev. B **92**, 104511 (2015).

[120] E. E. Huber and D. H. Ridgley, Phys. Rev. **135**, A1033–A1040 (1964).

[121] G. P. Felcher, Journal of Applied Physics **37**, 1056 (1966).

[122] J. B. Forsyth, S. J. Pickart, and P. J. Brown, Proceedings of the Physical Society **88**, 333–339 (1966).

[123] S. Takeuchi and K. Motizuki, Journal of the Physical Society of Japan **24**, 742–750 (1968).

[124] M. Matsuda, F. Ye, S. E. Dissanayake, J.-G. Cheng, S. Chi, J. Ma, H. D. Zhou, J.-Q. Yan, S. Kasamatsu, O. Sugino, T. Kato, K. Matsubayashi, T. Okada, and Y. Uwatoko, Phys. Rev. B **93**, 100405 (2016).

[125] H. J. Monkhorst and J. D. Pack, Phys. Rev. B **13**, 5188–5192 (1976).

[126] J. P. Perdew, K. Burke, and M. Ernzerhof, Phys. Rev. Lett. **77**, 3865–3868 (1996).

[127] S. Rundqvist, Acta Chem. Scand. **16**, 287 (1962).

[128] D. I. Khomskii, K. I. Kugel, A. O. Sboychakov, and S. V. Streltsov, Journal of Experimental and Theoretical Physics **122**, 484–498 (2016).

[129] Q. Niu, W. C. Yu, E. I. P. Aulestia, Y. J. Hu, K. T. Lai, H. Kotegawa, E. Matsuoka, H. Sugawara, H. Tou, D. Sun, F. F. Balakirev, Y. Yanase, and S. K. Goh, Phys. Rev. B **99**, 125126 (2019).

[130] P. M. R. Brydon, L. Wang, M. Weinert, and D. F. Agterberg, Phys. Rev. Lett. **116**, 177001 (2016).

[131]W. Yang, Y. Li, and C. Wu, Phys. Rev. Lett. **117**, 075301 (2016).

[132]L. Schoop, F. Pielnhofer, and B. Lotsch, English (US), Chemistry of Materials **30**, 3155–3176 (2018).

[133]L. M. Schoop, A. Topp, J. Lippmann, F. Orlandi, L. Müchler, M. G. Vergniory, Y. Sun, A. W. Rost, V. Duppel, M. Krivenkov, S. Sheoran, P. Manuel, A. Varykhalov, B. Yan, R. K. Kremer, C. R. Ast, and B. V. Lotsch, Science Advances **4** (2018).

[134]M. Manago, S. Kitagawa, K. Ishida, K. Deguchi, N. K. Sato, and T. Yamamura, Phys. Rev. B **100**, 035203 (2019).

[135]H. Usui and K. Kuroki, Phys. Rev. B **84**, 024505 (2011).

[136]F. Giusti, A. Marciniak, F. Randi, G. Sparapassi, F. Boschini, H. Eisaki, M. Greven, A. Damascelli, A. Avella, and D. Fausti, Phys. Rev. Lett. **122**, 067002 (2019).

[137]Q. Si, R. Yu, and E. Abrahams, Nat. Rev. Mater. **1**, 16017 (2016).

[138]T. Kawakami and M. Sato, Phys. Rev. B **100**, 094520 (2019).

[139]M. Malvestuto, V. Capogrosso, E. Carleschi, L. Galli, E. Gorelov, E. Pavarini, R. Fittipaldi, F. Forte, M. Cuoco, A. Vecchione, and F. Parmigiani, Phys. Rev. B **88**, 195143 (2013).

[140]D. G. Porter, V. Granata, F. Forte, S. Di Matteo, M. Cuoco, R. Fittipaldi, A. Vecchione, and A. Bombardi, Phys. Rev. B **98**, 125142 (2018).

[141]C. Autieri, M. Cuoco, and C. Noce, Phys. Rev. B **89**, 075102 (2014).

[142]M. D. Watson, Y. Feng, C. W. Nicholson, C. Monney, J. M. Riley, H. Iwasawa, K. Refson, V. Sacksteder, D. T. Adroja, J. Zhao, and M. Hoesch, PRL **118**, 097002 (2017).

[143]H. Z. Zhi, T. Imai, F. L. Ning, J.-K. Bao, and G.-H. Cao, Phys. Rev. Lett. **114**, 147004 (2015).

[144]T. Kong, S. L. Bud'ko, and P. C. Canfield, Phys. Rev. B **91**, 020507 (2015).

[145]H. Jiang, G. Cao, and C. Cao, Scientific Reports **5**, 16054 (2015).

[146]X.-X. Wu, C.-C. Le, J. Yuan, H. Fan, and J.-P. Hu, Chinese Physics Letters **32**, 057401 (2015).

[147]K. M. Taddei, Q. Zheng, A. S. Sefat, and C. de la Cruz, PRB **96**, 180506 (2017).

[148]K. M. Taddei, G. Xing, J. Sun, Y. Fu, Y. Li, Q. Zheng, A. S. Sefat, D. J. Singh, and C. de la Cruz, Phys. Rev. Lett. **121**, 187002 (2018).

[149]D. T. Adroja, A. Bhattacharyya, M. Telling, Y. Feng, M. Smidman, B. Pan, J. Zhao, A. D. Hillier, F. L. Pratt, and A. M. Strydom, Phys. Rev. B **92**, 134505 (2015).

[150]G. M. Pang, M. Smidman, W. B. Jiang, J. K. Bao, Z. F. Weng, Y. F. Wang, L. Jiao, J. L. Zhang, G. H. Cao, and H. Q. Yuan, Phys. Rev. B **91**, 220502 (2015).

[151]L.-D. Zhang, X. Wu, H. Fan, F. Yang, and J. Hu, EPL (Europhysics Letters) **113**, 37003 (2016).

[152]H. Zhong, X.-Y. Feng, H. Chen, and J. Dai, Phys. Rev. Lett. **115**, 227001 (2015).

[153]Z. Yi, C. Chao, and Z. Fu-Chun, Science Bulletin **62**, 208 (2017).

[154]V. I. Anisimov, I. V. Solovyev, M. A. Korotin, M. T. Czyzyk, and G. A. Sawatzky, Phys. Rev. B **48**, 16929–16934 (1993).

[155]L. Vaugier, H. Jiang, and S. Biermann, Phys. Rev. B **86**, 165105 (2012).

[156]M. M. Wysokinski, arXiv:1808.04109 (2018).

[157]A. Aperis, P. Maldonado, and P. M. Oppeneer, Phys. Rev. B **92**, 054516 (2015).

[158]M. Edelmann, G. Sangiovanni, M. Capone, and L. de'Medici, Phys. Rev. B **95**, 205118 (2017).

[159]W. Wu, K. Liu, Y. Li, Z. Yu, D. Wu, Y. Shao, S. Na, G. Li, R. Huang, T. Xiang, and J. Luo, National Science Review, nwz129 (2019).

[160]C. Xu, N. Wu, G.-X. Zhi, B.-H. Lei, X. Duan, F. Ning, C. Cao, and Q. Chen, arXiv:1909.04346 (2019).

[161]C.-C. Liu, C. Lu, L.-D. Zhang, X. Wu, C. Fang, and F. Yang, arXiv:1909.00943 (2019).

[162]P. W. Anderson, Phys. Rev. **124**, 41–53 (1961).

[163]C. Noce, Physics Reports **431**, 173 –230 (2006).

[164]S. Roy, C. Autieri, B. Sanyal, and T. Banerjee, Sci. Rep. **5**, 15747 (2015).

[165]A. Continenza, S. Picozzi, W. T. Geng, and A. J. Freeman, Phys. Rev. B **64**, 085204 (2001).